Mechanics of Materials 206 (2025) 105333

Contents lists available at ScienceDirect

Mechanics of Materials

journal homepage: www.elsevier.com/locate/mecmat

Research paper

Stimuli–responsive programmable mechanics of bi-level architected nonlinear mechanical metamaterials

S. Ghuku [a], S. Naskar [b], T. Mukhopadhyay [b,*]

[a] Department of Mechanical Engineering, Birla Institute of Technology, Mesra, India
[b] Faculty of Physical Sciences and Engineering, University of Southampton, Southampton, UK

ARTICLE INFO

Invited Editor Ghatu Subhash

Keywords:
Programmable metamaterials
Hard magnetic soft beam
Stimuli–responsive mechanics
Geometric and material nonlinearity
On-demand contactless stiffness
Active mechanical metamaterials

ABSTRACT

Mechanical metamaterials which are often conceptualized as a periodic network of beams have been receiving significant attention over the last decade, wherein the major focus remains confined to the design of micro-structural configurations to achieve application-specific multi-functional characteristics in a passive framework. It is often not possible to actively modulate the metamaterial properties post-manufacturing, critically limiting the applications for a range of advanced intelligent structural systems. To achieve physical properties beyond conventional saturation limits attainable only through unit cell architectures, we propose to shift the design paradigm towards more innovative bi-level modulation concepts involving the coupled design space of unit cell geometries, architected beam-like members and their stimuli–responsive deformation physics. On the premise of revolutionary advancements in additive manufacturing technologies, we introduce hard magnetic soft (HMS) material architectures in the beam networks following physics-informed insights of the stress resultants. Through this framework, it is possible to achieve real-time on-demand control and modulation of fundamental mechanical properties like elastic moduli and Poisson's ratios based on a contactless far-field stimuli source. A generic semi-analytical computational framework involving the large-deformation geometric non-linearity and material non-linearity under magneto-mechanical coupling is developed for the effective elastic properties of HMS material based bi-level architected lattices under normal or shear modes of mechanical far-field stresses, wherein we demonstrate that the constitutive behaviour can be programmed actively in an extreme-wide band based on applied magnetic field. Under certain combinations of the externally applied mechanical stress and magnetic field depending on the residual magnetic flux density, it is possible to achieve negative stiffness and negative Poisson's ratio with different degrees of auxecity, even for the non-auxetic unit cell configurations. The results further reveal that a single metamaterial could behave like extremely stiff metals to very soft polymers through contactless on-demand modulation, leading to a wide range of applicability in statics, stability, dynamics and control of advanced mechanical, aerospace, robotics and biomedical systems at different length scales.

1. Introduction

Introduction to mechanical metamaterials and a brief literature review. Mechanical metamaterials are an advanced broad class of engineered materials with architected microstructures having designed geometrical arrangements, leading to unprecedented physical and mechanical properties that are derived primarily based on their unique internal structures and geometry along with the intrinsic materials from which they are made. Metamaterials are often conceptualized as a periodic network of beam-like (or plate and shell-like) members at a relatively lower length scale to obtain effective properties at higher length scales, and find critical applications in a vast spectrum of structural and mechanical applications ranging from nano and micro to macro scale systems (Zadpoor, 2016; Sinha and Mukhopadhyay, 2023b; Mukhopadhyay and Adhikari, 2017a; Gao et al., 2023). A typical bottom-up homogenization framework ranging from an equivalent continuum (with effective properties) at macro-level to honeycomb microstructures at a lower length scale is shown in Fig. 1(a). Effective mechanical properties of such periodic beam networks not only depend on the beam-level geometry and intrinsic material characteristics but also are governed by the configuration of the network, i.e. unit cell geometry (Gibson and Ashby, 1999; Fleck et al., 2010). Compared to the conventional naturally available materials, the lattice metamaterials have low density and they provide tunable enhanced multi-functional properties based on the application-specific demands (Wadley, 2006;

* Corresponding author.
E-mail address: T.Mukhopadhyay@soton.ac.uk (T. Mukhopadhyay).

https://doi.org/10.1016/j.mechmat.2025.105333
Received 17 October 2024; Received in revised form 3 March 2025; Accepted 18 March 2025
Available online 27 March 2025

Wang et al., 2020b; Wu et al., 2021b; Bekele et al., 2023). Due to the advantages over the natural materials, the lattice materials have drawn significant attention of the material scientists and engineers for the last few decades (Surjadi et al., 2019; Wu et al., 2021a; Dalela et al., 2021). Revolutionary advancements in the manufacturing technologies especially in the field of additive manufacturing elevated such interest by providing the freedom to the designers in manufacturing complex configurations (Tibbits, 2014; Bandyopadhyay and Heer, 2018; Chen and Zheng, 2018).

The major focus of the research on mechanical metamaterials has been the development of several analytical, computational and experimental frameworks for estimation of the effective responses of periodic beam networks under static loading (Malek and Gibson, 2015; Mukhopadhyay and Adhikari, 2017b; Sinha and Mukhopadhyay, 2022), dynamic and wave propagation (Adhikari et al., 2021; Gonella and Ruzzene, 2008), buckling (Wilbert et al., 2011; Jang and Kyriakides, 2015; Jiménez and Triantafyllidis, 2013; Zschernack et al., 2016), crushing (Liu et al., 2016), low-velocity impact (Hu and Yu, 2013) etc. Another aspect of the research area has been the modulation of effective properties by designing the network configurations in terms of lattice geometric parameters, like, cell angle, thickness to span ratio of the cell walls along with the aspect ratio, etc. (Thomas and Tiwari, 2019; Scarpa et al., 2000; Sorohan et al., 2019). Auxetic configurations among the architected materials have drawn special attention due to providing negative Poisson's ratio (Yang et al., 2015; Kolken and Zadpoor, 2017; Mukhopadhyay and Kundu, 2021), and a range of associated mechanical advantages including impact and indentation resistance, shape modulation, higher stiffness and improved dynamic properties. In addition to the hexagonal honeycomb and re-entrant auxetic configurations, several other forms of lattices, like, rhombic, rectangular brick, triangular, rectangular, square, etc., have found critical engineering applications due to their special bending or stretching dominated characteristics (Wang and McDowell, 2004). Manufacturing the designed complex configurations has become feasible using additive manufacturing, followed by experimental investigations (Balawi and Abot, 2008; Mukhopadhyay et al., 2020a; Papka and Kyriakides, 1998; Damanpack et al., 2019) both for validating the computational frameworks and subsequent industry-scale production.

Due to the extensive investigations on the design of network configurations for modulation of the effective properties of lattice materials, the research area has become saturated in the past decade. Hence, the research area has been shifting towards more innovative designs of geometry and intrinsic material characteristics at the elementary beam-level. One such aspect is to exploit the non-linear characteristics of the elementary beam members undergoing large deformation. For modulation of the effective properties of lattice metamaterials as a function of the non-linearity, several geometrically non-linear frameworks have been developed in the last few years (Fu et al., 2016; Zhao et al., 2020; Nampally et al., 2020). Another innovative concept at the elementary beam-level to enhance the effective mechanical properties is providing anti-curvature to the cell walls subjected to a particular mode of applied mechanical loading (Ghuku and Mukhopadhyay, 2022a; Prajwal et al., 2022; Ghuku and Mukhopadhyay, 2022b). Significant enhancements in lattice stiffness or flexibility and elastic failure strength can be achieved due to the introduction of anti-curvature to the cell walls (Ghuku and Mukhopadhyay, 2022a; Prajwal et al., 2022; Ghuku and Mukhopadhyay, 2022b). With the revolutionary advancements in the field of additive manufacturing, recently lattices made of multiple intrinsic materials have been proposed which possess unprecedented mechanical properties, attainable based on an expanded design space (Vogiatzis et al., 2017; Mirzaali et al., 2018; Kang et al., 2019; Mukhopadhyay et al., 2020b). In such literature, the major focus remains confined to the design of micro-structural configurations to achieve application-specific multi-functional characteristics in a passive framework. It is not possible to actively modulate the metamaterial properties post-manufacturing, critically limiting the applications for a range of advanced intelligent structural systems. To achieve physical properties beyond conventional saturation limits attainable only through unit cell architectures, we propose to shift the design paradigm towards more innovative bi-level modulation concepts involving the coupled design space of unit cell geometries, architected beam-like members and their stimuli–responsive deformation physics. We would introduce hard magnetic soft (HMS) material (Lu et al., 2024) architectures in the beam networks following physics-informed insights of the stress resultants. The novel HMS lattice or beam network is very light in weight but it would be able to demonstrate a wide range of stiffness (including sign reversal) depending on applied magnetic flux. The foundation of the HMS material along with the relevant reported work in the literature on HMS beam deformations are described very briefly in the following paragraph.

Soft materials are a class of newly developed materials that have found immense technological applications in a diverse field, especially in biomedicine (Pankhurst et al., 2003; Zhao et al., 2011), soft robotic (Kim et al., 2013; Rich et al., 2018), and flexible electronic devices (Rogers et al., 2010; Li, 2016). Controllable properties of soft active materials under external stimuli, like, light (Katz and Burdick, 2010), heat (Morishima, 2007), electric (Miyajima et al., 2009), magnetic field (Kim et al., 2018) etc., open a new avenue to design application-specific devices. Recent advancements in 3D and 4D technologies make the innovative designs feasible and motivated the research community (Truby and Lewis, 2016; Chu et al., 2020; Josselin et al., 2024). One interesting class among such soft active materials which promises significant potential in critical engineering applications is the hard magnetic soft material (HMS material) (Lu et al., 2024). HMS material is manufactured by embedding hard magnetic particles into soft material matrix. This newly developed active material (HMS material) shows a magnetically hard and mechanically soft property (Lum et al., 2016). As the beam is a very fundamental element in designing any structural device, investigations on the response of beam made of HMS material under magnetic actuation have drawn the attention of the research community. The complications coming from geometric non-linearity due to large deformation and material non-linearity under magneto-mechanical coupling make the analysis of HMS beam structures challenging (Wang et al., 2020a; Chen and Wang, 2021). In the past few years, several analytical and numerical models have been proposed by the researchers to capture the non-linear response of HMS beams under external magnetic stimulation (Zhao et al., 2019; Kim et al., 2019; Chen and Wang, 2020). Besides the theoretical works, some experimental investigations on HMS beam responses are also reported in the literature (Zhao et al., 2019; Furusawa et al., 2019). To use the devices made of HMS beams in soft robotic and electronic applications, the deformed shapes of the HMS beam are of interest and need to be controlled. By properly designing the residual magnetic flux density in the HMS beam to be subjected to a particular external magnetic field, we can design the deformed shapes (Chen et al., 2020a). As most of the structures in the biological world consist of the feature of functionally graded property, to meet the complex demand of potential applications of HMS beam structures, recently functionally graded HMS materials are being designed and manufactured (Bartlett et al., 2015; Chen et al., 2020b).

Rationale behind the proposed magneto-active metamaterials. The above-presented literature review reveals that despite being a topic of interest, the theoretical investigations on HMS beam structures focus on structural characteristics under magnetic actuation only. Investigations on the multi-physical mechanics of HMS beam structures under combined mechanical load and magnetic actuation are not addressed in the literature sufficiently. Moreover, most of the reported theoretical investigations are numerical in the framework of commercial packages which lack physical insights into the problems. Some analytical models are also reported in the literature but they are limited to simple beam problems in terms of loading conditions, geometry, and

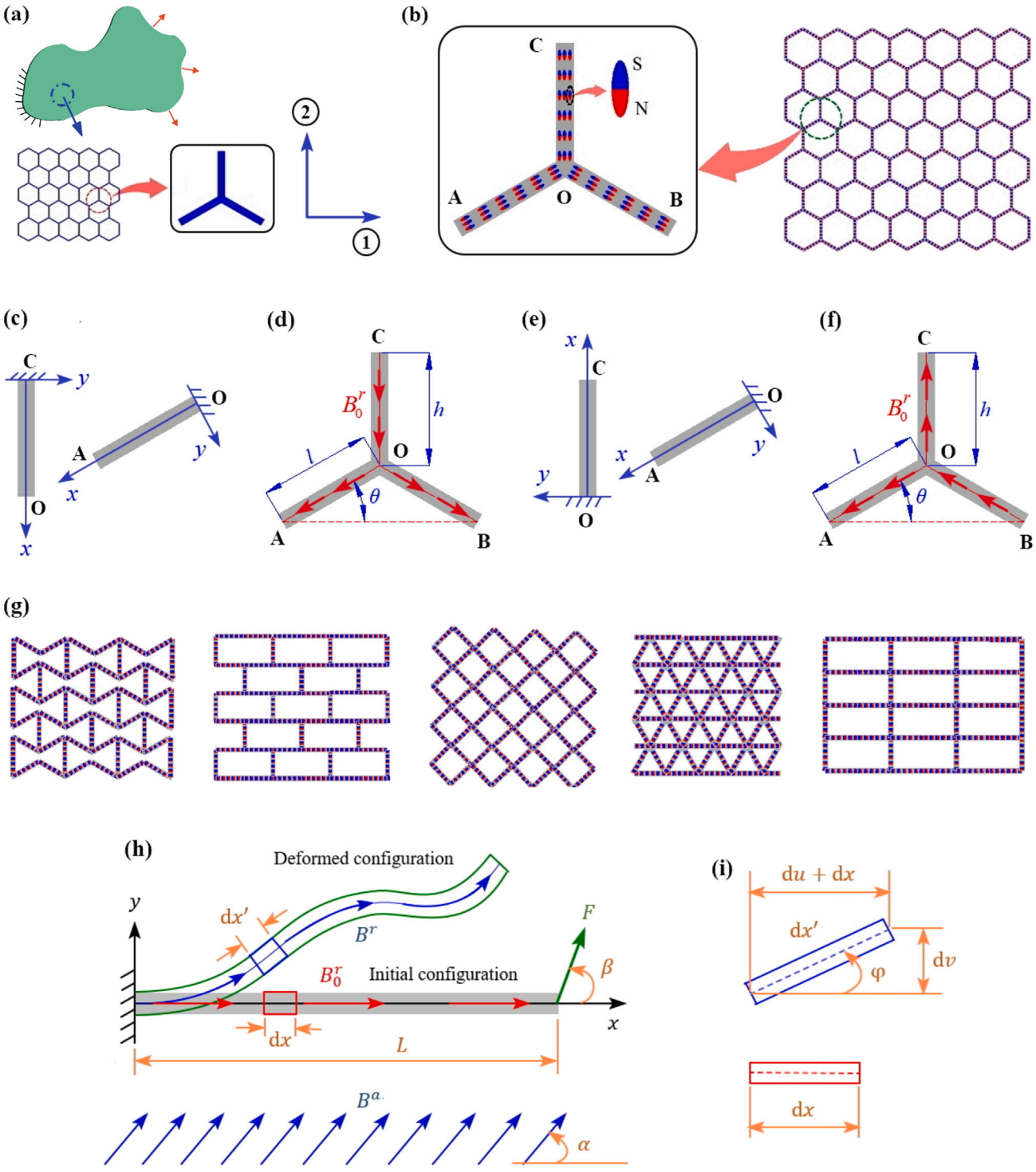

Fig. 1. Bi-level architected lattice metamaterials with periodic network of soft beams having embedded hard magnetic particles. (a) A typical homogenization framework for conventional lattice metamaterials ranging from equivalent continuum at macro-level to honeycomb microstructures at the lower length scales. **(b)** Schematic representation of hexagonal HMS beam network with the representative unit cell to analyse multi-physical mechanics under combined external mechanical and magnetic loads. **(c–f)** Definition of local Cartesian coordinate systems (x, y) and representation of residual magnetic flux density B_0^r in the unit cell of hexagonal HMS beam network to be subjected to: (c, d) magnetic field along direction-2 in combination with normal stress along direction-1 (σ_1) or direction-2 (σ_2), (e, f) magnetic field along direction-2 in combination with in-plane shear stress (τ). **(g)** Different other forms of periodic HMS beam networks ((I - III) derivatives of hexagonal lattices, (IV) triangular lattice, (V) rectangular lattice) to be analysed within the proposed multi-physical mechanics-based framework. **(h)** Large deformation multi-physical mechanics of HMS beams representing the generalized member of periodic HMS beam networks under combined mechanical and magnetic loading. **(i)** Deformation components of a generalized HMS beam element to derive large deformation kinematics.

boundary conditions. In this paper, we consider the complicated multi-physical mechanics of periodic HMS beam networks subjected to large deformation under combined mechanical and magnetic loads. One major objective is to develop a physically insightful semi-analytical framework to estimate the non-linear effective elastic moduli of the HMS beam networks under the combined fair-field mechanical stress and magnetic field. By properly designing the residual magnetic flux density in the HMS beam elements under an optimal combination of mechanical stress and magnetic field along with exploiting the geometric and material non-linearities, modulation of the effective elastic moduli through the developed semi-analytical framework would be attempted in the present work.

With the progress in manufacturing capabilities (Montgomery et al., 2020), active lattice metamaterials (Sinha and Mukhopadhyay, 2023b; Qi et al., 2022) have started receiving significant attention from the scientific community. In the context of active elastic property and stiffness modulation in lattice metamaterials with distributed actuation throughout the connecting beam spans, the pioneering works with detailed computational framework development can be traced in the area of piezoelectric lattices (Singh et al., 2021, 2022a). The major lacuna in piezoelectric lattices is the absence of contactless modulation and involvement of wire networks for supplying voltage to each constituting beams. Later, lattices with magnetostrictive layers (with distributed actuation throughout the connecting beam spans) were proposed for contactless on-demand elasticity programming (Singh et al., 2022b). All these metamaterials were developed in the regime of small deformation linear analysis framework. Some of the early research on active control of stiffness using magnetic control can be traced back to exploitation of discrete magnets attached to the connecting beam members of the lattice unit cells (Dudek et al., 2018). Unlike most of the active lattice metamaterials, Alkuino and Zhang (2024) presented discrete magneto-active lattices where magnetic particles are embedded in the joints rather than the beam-like connecting elements, wherein the active joint movement is exploited for property modulation in the proposed design. Jackson et al. (2018) proposed 4D field responsive lattice metamaterials with connecting polymer tube-like elements filled with magnetorheological fluid suspensions. In general, magneto-active metamaterials have been attracting significant attention recently covering different spectrum of physical designs including elastic, impact, vibration, wave propagation and acoustics for on-demand control (Sim and Zhao, 2024; Dudek et al., 2019; Zhang et al., 2023; Montgomery et al., 2021; Galea et al., 2022). Lately, HMS material based hexagonal lattices with distributed uniform actuation along the beam-like constituting members have been investigated for active contactless property modulation considering geometric nonlinearity (Sinha and Mukhopadhyay, 2023a). In this semi-analytical framework of the earlier work, only hexagonal lattices and their derivatives such as rhombic, rectangular brick and auxetic configurations can be analysed. In the present work we extend the computational framework to analyse other bending and stretching dominated lattices such as triangular and rectangular configurations. Further, for enhancing the efficiency of magnetic actuation, we would introduce non-uniform residual magnetic flux to exploit the concepts of anti-curvature (Ghuku and Mukhopadhyay, 2022a) in metamaterials design.

Description of the bi-level architected lattices with non-uniform magnetic flux density. A typical hexagonal network of HMS beams is shown schematically in Fig. 1(b). Within the framework of unit cell approach, an appropriate unit cell consisting of three HMS beam members OA, OB, and OC is chosen as shown in Fig. 1(b) to analyse multi-physical lattice mechanics under combined mechanical and magnetic load. In the figure, an enlarged view of embedded hard magnetic particles is shown for clear understanding. From the understanding of boundary conditions for the honeycomb lattices made of conventional elastic materials (Gibson and Ashby, 1999), definitions of local Cartesian coordinate frames $(x,\ y)$ for the inclined member OA and vertical member OC of the unit cell to be subjected to the magnetic field along direction-2 (B^a) in combination with normal mechanical stress along direction-1 (σ_1) or direction-2 (σ_2) are shown in Fig. 1(c). Similarly, definitions of local Cartesian coordinate frames $(x,\ y)$ for the inclined and vertical members of the unit cell to be subjected to the magnetic field along direction-2 (B^a) in combination with in-plane shear stress (τ) are shown in Fig. 1(e). The direction and magnitude of residual magnetic flux density B_0^r in the HMS beam member are controlled by the orientation and density of the hard magnetic particles embedded in the soft material. Mathematically, the direction and magnitude of B_0^r are defined by a coefficient S. If the residual magnetic flux density B_0^r is uniform along the beam axis and directed along the x axis of the local Cartesian frame $(x,\ y)$, the value of S is unity, i.e., $S = 1$. If the direction of uniform B_0^r is opposite to x axis, then $S = -1$. For generalized distribution of B_0^r, the coefficient $S(x)$ is a function of beam length along the x axis of the local Cartesian frame $(x,\ y)$. For the unit cells to be subjected to the magnetic field along direction-2 in combination with either normal mode or shear mode of mechanical stress, generalized representations of the residual magnetic flux density B_0^r in the HMS beam members are shown in Fig. 1(d) and (f) corresponding to the local frames $(x,\ y)$ as defined in Fig. 1(c) and (e) respectively. Note that in Fig. 1(f), the direction of residual magnetic flux density B_0^r is opposite for the inclined members OA and OB. This opposite distribution makes the inclined members behave structurally symmetric when subjected to in-plane shear stress τ in combination with external magnetic field B^a. This phenomenon will be described in more detail later through schematic diagrams in connection with the mathematical formulation of shear modulus.

As discussed in the preceding paragraphs, we propose a novel class of metamaterials as a network of beams made of soft material with embedded hard magnetic particles which enables real-time on-demand control and modulation of non-linear elastic properties based on a contactless far-field stimuli source. The metamaterial involves a dual design space at the lower length scale (referred to as micro-scale in the subject domain of metamaterials) as follows. (1) Architecturing of the hard magnetic particle distribution within the HMS beam elements tailors their multi-physical large deformation mechanics at the lower length scale (2) Architecturing of the network's periodic geometric configurations (cell angle, vertical to inclined cell wall length ratio, thickness to inclined cell wall length ratio) further tailors the unit cells' large deformation mechanics. Such bi-level architectures and designs at the lower length scale (referred to as micro-scale) govern the homogenized elastic properties of the proposed HMS metamaterials at the higher length scale (referred to as macro-scale) of the entire lattice dimension. Hence, the developed computational framework reported in the present article is basically a multi-scale framework starting from the magnetic particle architected HMS beams and periodic geometry of unit cell configurations at the micro-scale yielding to tailored homogenized non-linear elastic properties of HMS beam network at the macro-scale. Note that the computational framework for obtaining the effective nonlinear elastic properties of the lattice would essentially involve analysing appropriate unit cells with periodic boundary conditions. The foundational concept of the multi-scale modelling of conventional lattice metamaterials (involving unit cells that consist of homogeneous passive beams) is demonstrated through Fig. 1(a), and subsequently, the concept of the proposed bi-level architected novel class of HMS metamaterials (involving unit cells that consist of architected magneto-active beams) is introduced through Fig. 1(b, g).

Scope of the present study. To estimate the non-linear effective elastic moduli of the periodic HMS beam network, a generalized multi-physical mechanics problem of HMS beam subjected to combined mechanical and magnetic loads would be defined within the framework of the unit cell approach. The HMS beam problem involves complex effects coming from geometric non-linearity due to large deformation and material non-linearity due to magneto-elastic coupling. A physically insightful semi-analytical framework would be developed here through the variational principle-based energy method within the non-linear

kinematic setting of the Euler–Bernoulli beam theory using the material constitutive law according to the Yeoh hyperelastic model. Based on the beam-level deformation results, effective elastic moduli of the periodic HMS beam networks (i.e lattices) would be computed by accounting the unit cell geometry and periodic boundary conditions. The semi-analytical beam model will be validated by comparing the non-linear deformed configurations under separate mechanical load and magnetic actuation with the available literature (Chen and Wang, 2021; Chen et al., 2020a). After the validation study, a few critical beam-level numerical results will be presented first under combined mechanical and magnetic loading for HMS beams with symmetric and asymmetric residual magnetic flux density. Through the numerical results, the effect of asymmetry in residual magnetic flux density in defining a generalized HMS beam problem of the HMS beam network along with the effect of centreline extensibility in analysing large deformation characteristics of HMS beam will be investigated. A validation study of the semi-analytical framework at the periodic beam network-level will also be carried out by comparing the non-linear effective elastic moduli with the available results in the literature for honeycomb lattices under different modes of far-field mechanical loads (Fu et al., 2016; Ghuku and Mukhopadhyay, 2022a). Following the validated semi-analytical framework, the effects of magnetic field in combination with the different modes of far-field mechanical stress field on the non-linear effective elastic moduli of periodic HMS beam network with uniform residual magnetic flux density will be studied. Based on the kinematic and kinetic conditions of the beam elements of the hexagonal HMS beam network, two physics-informed designs of residual magnetic flux density will further be proposed which would significantly influence the non-linear effective elastic moduli. Through the numerical results, we will show that the proposed lightweight HMS beam networks or lattices possess broadband modulation capability of the non-linear specific stiffness ranging from very high stiffness like hard metal to very low stiffness even lower than soft polymers depending on the residual magnetic flux density and the compound effect of the externally applied mechanical load and the magnetic field. Under certain combinations of the mechanical and magnetic fields, it will be shown that the HMS lattices show negative stiffness as well. The generality of the developed multi-physical mechanics-based semi-analytical framework will be demonstrated by analysing non-linear elastic moduli of five other forms of HMS beam networks, namely, auxetic, rectangular brick, rhombic, triangular, and rectangular networks as shown in Fig. 1(g). Note that under the influence of combined far-field mechanical stresses and magnetic field, the unit cell mechanics of different considered lattice configurations becomes significantly involved that has not been investigated in the literature so far.

After presenting a brief review of literature on mechanical metamaterials and the rationale behind proposing the present novel class of lattices in this introductory section (Section 1), the mathematical framework for the estimation of non-linear effective elastic moduli of periodic HMS beam networks under different modes of far-field mechanical stress in combination with magnetic field will be presented in Section 2. Thereafter, Section 3 will present the beam-level and periodic beam network-level results along with the validation studies. Applicability of the proposed physically insightful framework of the periodic HMS beam network to different forms of lattices will be demonstrated through numerical results. The conclusions will be drawn in Sections 4 and 5 along with the prospective future scopes of the proposed novel class of HMS lattices.

2. Computational framework for stimuli–responsive lattices

A HMS beam multi-physical mechanics based (refer to Fig. 1(h, i)) semi-analytical framework is developed in this section to estimate the non-linear effective elastic moduli of periodic HMS beam networks subjected to magnetic field B^a along direction-2 either in combination with remote normal stress along direction-1 (σ_1), direction-2 (σ_2) or remote in-plane shear stress τ. The combined loading conditions of mechanical normal stress (σ_1 or σ_2) and magnetic field (B^a) for the unit cell of hexagonal HMS beam network (refer to Fig. 1(d)) are shown in Fig. 2(a) and (d) respectively. Whereas, the loading condition of mechanical in-plane shear stress (τ) in combination with the applied magnetic field (B^a) for the corresponding HMS unit cell (refer to Fig. 1(f)) is shown in Fig. 3(a). Under the combined loading condition as shown in Fig. 2(a), we obtain the longitudinal effective Young's modulus E_1 and Poisson's ratio ν_{12} of the hexagonal HMS beam network. For the combined loading condition as shown in Fig. 2(d), we obtain the transverse effective Young's modulus E_2 and Poisson's ratio ν_{21}. Whereas, under the combined loading condition of the shear mode of mechanical load and the magnetic field as shown in Fig. 3(a), we can estimate the effective shear modulus G_{12} of the hexagonal HMS beam network. Similar loading conditions are presented for other forms of lattices in Figs. 4 and 5. Here it should be noted that though the multi-physical mechanics of the HMS unit cells is presented in Figs. 2–5 for the compressive mode of normal stress and anti-clockwise mode of shear stress respectively in combination with the generalized residual magnetic flux density having coefficient $S(x)$, the developed formulation is generalized and valid for the combination of any mode of the normal (compressive or tensile) and shear (anti-clockwise or clockwise) mechanical stress with a generalized magnetic field.

Under the applied combined mechanical stress and magnetic field, developed forces and large deformation kinematics of the HMS beam elements of the unit cell are analysed first. Based on the kinetic and kinematic descriptions, a large deformation problem of the HMS beam representing a general beam-like element of the periodic network is defined, wherein the boundary and loading conditions are applied based on unit cell periodicity and applied external mechanical stress and magnetic flux, respectively. Non-linear multi-physical mechanics of the defined generalized large deformation HMS beam problem under combined mechanical and magnetic load is analysed subsequently through the variational energy principle-based semi-analytical framework (with appropriate beam-level boundary condition to ensure periodicity of the unit cells). Using the beam-level deformation results within the unit-cell framework, the effective elastic moduli (E_1, ν_{12}, E_2, ν_{21}, and G_{12}) of a periodic HMS beam network are computed. Thus, following a multi-scale framework, the homogenized nonlinear elastic properties of the proposed metamaterials at the higher length scale (referred to as macro-scale) are estimated in terms of the beam-level large deformation measures coupled with unit cell geometry under combined mechanical and magnetic loads at the lower length scale (referred to as micro-scale). In this context, it can be noted that the proposed computational framework is scale-independent in principle; the only condition is to maintain a substantial difference between the unit cell dimensions and the dimension of the overall lattice that leads to the computation of homogenized effective properties. In the forthcoming subsections, followed by establishing a generic beam-level computational framework, we will first develop a semi-analytical formulation for the effective elastic moduli of hexagonal lattices, and subsequently different other lattice geometries will be considered.

2.1. Generalized beam-level problem definition

The load–deformation characteristics of any member of the HMS beam network under any combination of the fair-field normal or shear mode of mechanical stress and magnetic field as presented through Figs. 2–5 are defined as a generalized geometrically non-linear HMS beam deformation problem. Such a generalized large deformation HMS beam problem can be defined either as a full-beam problem or as a half-beam problem under the specific boundary condition to ensure unit cell level periodicity (all the beams under consideration here need to have both the edges rotationally restrained). Both the type of geometrically non-linear HMS beam deformation problem is presented schematically in a generalized way in Fig. 1(h, i) and described in the following two subsections.

2.1.1. Full-beam problem

When the full length of the inclined or vertical members of a periodic HMS beam network (refer to Figs. 2–5) is considered for the definition of the generalized beam problem, the problem is called the full-beam problem. For example, the length L of the generalized HMS beam as shown in Fig. 1(h), is either equal to l for the inclined member or equal to h for the vertical member of a hexagonal HMS beam network. For the full-length HMS beam, one end is fixed with the other end being rationally restrained but free to translation and subjected to concentrated force F in combination with magnetic field B^a with inclination angles β and α respectively as shown in Fig. 1(h).

For the full-length HMS beam, rotation of centreline φ is zero at both the ends ($x = 0$ and $x = L$) (refer to Fig. 1(h, i)). As the HMS beam is subjected to axial load also due to the combined effect of the mechanical and magnetic field, the beam centreline has non-zero axial strain ε at both the ends ($x = 0$ and $x = L$). The kinematic boundary conditions of the HMS full-beam problem are summarized below.

$$\varphi = 0 \text{ at } x = 0 \text{ and } x = L \tag{1a}$$

$$\varepsilon \neq 0 \text{ at } x = 0 \text{ and } x = L \tag{1b}$$

With the proper definition of the load magnitudes (F and B^a) and their inclination angles (β and α) as presented later in the manuscript (for example, Eqs. (23)–(36) for the hexagonal lattices) along with the respective length (for example, $L = l$ or $L = h$ for hexagonal lattices) and boundary conditions (Eq. (1)), we can simulate deformation characteristics of each member of the HMS beam networks.

For an ordinary beam of length L_o with the prescribed boundary conditions undergoing small deformation under mechanical load only, the transverse tip-deflection δ_y under transverse load F_y and the axial tip-deflection δ_x under axial load F_x are obtained analytically (Gibson and Ashby, 1999) as $\delta_y = \dfrac{F_y L_o^3}{12 E_s I}$ and $\delta_x = \dfrac{F_x L_o}{E_s A}$. In these equations, E_s denotes Young's modulus of the elastic beam material, and I and A are the rotational inertia and area of the beam cross-section. Note that the above-presented analytical solutions are not concerned with the present large deformation HMS beam problem. These analytical solutions are only used for analogy demonstration of boundary condition modelling of the full-beam problem using cantilevered half-beam problem as presented in the following subsection.

2.1.2. Half-beam problem

The full-beam made of ordinary elastic material undergoing small deformation under mechanical load only as presented in the preceding subsection, can be modelled as two half-beams with cantilever boundary conditions exploiting the physical insight that bending moment becomes zero for the full beam at the midpoint here. The transverse and axial deflections of the tip of the cantilevered half-beam of length $L_o/2$ are analytically (Gibson and Ashby, 1999) given by $\delta_y = \dfrac{F_y L_o^3}{24 E_s I}$ and $\delta_x = \dfrac{F_x L_o}{2 E_s A}$. These analytical deflections obtained from the half-beam model of the ordinary beam are exactly half of the corresponding deflection results as presented in Section 2.1.1. Hence, doubling the deflection results coming from the half-beam model gives the same results as the full-beam model for an ordinary beam. A similar observation also becomes apparent for axial deformation.

Following the observations on boundary conditions, the considered large deformation HMS full-beam problem under combined mechanical and magnetic load is modelled here as HMS half-beam problem. For example, in the HMS half-beam problem concerning hexagonal lattices, length L of the generalized HMS beam as shown in Fig. 1(h) will be either $l/2$ for the inclined member or $h/2$ for the vertical member of the HMS beam network. Note that consideration of the half beam will lead to more computational efficiency compared to considering a full-length beam in the nonlinear multiphysical analysis. Boundary conditions of the generalized half-beam problem are summarized below.

$$\varphi = 0 \text{ at } x = 0 \text{ and } \frac{\mathrm{d}\varphi}{\mathrm{d}x} = 0 \text{ at } x = L \tag{2a}$$

$$\varepsilon \neq 0 \text{ at } x = 0 \text{ and } x = L \tag{2b}$$

Note that the modelling of HMS full-beam as HMS half-beam is only possible if the residual magnetic flux density B_0^r is symmetric about the mid-point of the full-length beam. The statement will be proved in Section 3 through numerical results from the full-beam and half-beam models with both symmetric and asymmetric residual magnetic flux density.

Large deformation analysis of the generalized HMS beam (refer to Fig. 1(h, i)) with the above-prescribed boundary conditions (Eqs. (1) and (2)) under combined mechanical and magnetic load is not readily available in the literature. A semi-analytical beam model is developed here to analyse such multi-physical mechanics problem as presented in the next subsection (Section 2.2).

2.2. Large deformation analysis of generalized HMS beam problem

Large deformation characteristics of the generalized HMS beam with residual magnetic flux density B_0^r concerning the initial configuration subjected to combined mechanical load F and magnetic field B^a as shown in Fig. 1(h, i) is analysed. Governing equation of the geometric non-linear problem is derived in a semi-analytical framework using the variational principle-based minimization of total potential energy method. In the derivation of the governing equation, we consider the centreline extension of the beam in addition to the bending mode of deformation within the geometrically non-linear kinematic setting of the Euler–Bernoulli beam theory. Derivation of the governing equation through such a generalized extensible model is presented first in the following subsection. To investigate the effect of axial rigidity of the hyperelastic HMS beam, a special form of the governing equation neglecting centreline extension is presented in the following subsection. The final algebraic form of the governing equation of the HMS beam problem derived either through the extensible model or through the inextensible model involves non-linearity due to the coupling of different deformation degrees of freedom. To solve the coupled non-linear equation, we develop an iterative computational framework as presented subsequently in this subsection.

2.2.1. Extensible model

2.2.1.1. Kinematics. To account for geometrically exact non-linearity, the beam deformation is described in terms of the rotation φ and strain ε of the beam centreline instead of the in-plane and transverse displacement fields u and v respectively. From the geometry of deformation as presented in Fig. 1(i), the displacement fields u and v are expressed in terms of the centreline rotation φ and centreline strain ε of the HMS beam as given below.

$$\frac{\mathrm{d}u}{\mathrm{d}x} = (1+\varepsilon)\cos\varphi - 1 \tag{3a}$$

$$\frac{\mathrm{d}v}{\mathrm{d}x} = (1+\varepsilon)\sin\varphi \tag{3b}$$

As the left end of the beam is considered fixed (refer to Fig. 1(h)), the displacement fields u and v are zero at $x = 0$. With the kinematic conditions, relations of the displacement fields u and v with the independent variables φ and ε are obtained by integrating Eq. (3) as given below.

$$u = \int_0^x \left\{ (1+\varepsilon)\cos\varphi - 1 \right\} \mathrm{d}x \tag{4a}$$

$$v = \int_0^x (1+\varepsilon)\sin\varphi \,\mathrm{d}x \tag{4b}$$

2.2.1.2. Material model. The material of the HMS beam under study is considered a soft material with Young's modulus E_s. The hyperelastic characteristics of the HMS beam material are modelled by the strain energy density function Φ which is defined below according to the Yeoh hyperelastic model (Chen and Wang, 2021).

$$\Phi = \sum_{i=1}^{3} C_{i0}\left\{(1+\varepsilon)^2 + \frac{2}{1+\varepsilon} - 3\right\}^i \tag{5}$$

The corresponding nominal stress, defined as $\sigma_N = \frac{\mathrm{d}\Phi}{\mathrm{d}\varepsilon}$, is obtained based on the Yeoh hyperelastic model (Chen and Wang, 2021) using Eq. (5) as given below.

$$\sigma_N = 2\left[C_{10} + 2C_{20}\left\{(1+\varepsilon)^2 + \frac{2}{1+\varepsilon} - 3\right\} + 3C_{30}\left\{(1+\varepsilon)^2 + \frac{2}{1+\varepsilon} - 3\right\}^2\right]\left\{(1+\varepsilon) - \frac{1}{(1+\varepsilon)^2}\right\} \tag{6}$$

Through Taylor expansion of Eq. (6) keeping the linear term, Young's modulus of the hyperelastic beam material is obtained as

$$E_s = 6C_{10} \tag{7}$$

2.2.1.3. Governing equation. Governing equation for the large deformation characteristics of the HMS beam under combined mechanical and magnetic load is derived through variational principle based minimization of total potential energy, as defined mathematically by

$$\delta\left(U_E + U_M + V\right) = 0 \tag{8}$$

In the above equation, U_E, U_M, and V are the elastic strain energy of the HMS beam, magnetic potential energy of the HMS beam, and potential energy of the external mechanical load. The elastic strain energy of the HMS beam U_E consists of membrane and bending strain energies which in total is given by

$$U_E = A\int_0^L \Phi\,\mathrm{d}x + \frac{E_s I}{2}\int_0^L \left(\frac{\mathrm{d}\varphi}{\mathrm{d}x}\right)^2 \mathrm{d}x \tag{9}$$

Magnetic potential energy U_M of the HMS beam due to the interaction of the externally applied magnetic field B^a with the residual magnetic flux density B_0^r (refer to Fig. 1(h)) is given by (Chen et al., 2020a)

$$U_M = -\frac{A}{\mu_0}\int_0^L S\left|B_0^r\right||B^a|(1+\varepsilon)\cos(\varphi-\alpha)\,\mathrm{d}x \tag{10}$$

In the above equation, μ_0 denotes permeability of vacuum. On the other hand, potential energy of the externally applied mechanical load F is defined as $V = -F_x u|_{x=L} - F_y v|_{x=L}$, where F_x and F_y are the components of force F in the x and y directions, given by $F_x = F\cos\beta$ and $F_y = F\sin\beta$ respectively (refer to Fig. 1(h)). Using Eq. (4), the potential energy V is expressed in terms of the independent variables φ and ε as given below.

$$V = -F_x\int_0^L\left\{(1+\varepsilon)\cos\varphi - 1\right\}\mathrm{d}x - F_y\int_0^L(1+\varepsilon)\sin\varphi\,\mathrm{d}x \tag{11}$$

Before going to further derivation of the governing equation through the energy principle, the physical coordinate system (x, y) is transformed into the computational frame (ξ, η) and some other non-dimensional geometric and material parameters are introduced as defined below.

$$\xi = \frac{x}{L},\ \eta = \frac{y}{L},\ \Pi_0 = \frac{AL^2}{I},\ \bar{\sigma}_N = \frac{\sigma_N}{E_s},\ B = \frac{\left|B_0^r\right||B^a|\,\Pi_0}{E_s\mu_0},$$
$$C = \frac{FL^2}{E_s I},\ \bar{F}_x = C\cos\beta,\ \bar{F}_y = C\sin\beta \tag{12}$$

Putting the energy expressions presented in Eqs. (9)–(11) with respect to the normalized coordinate frame (ξ, η) in terms of the normalized parameters (Eq. (12)) into the energy principle (Eq. (8)), the governing equation is obtained in variational form as presented below.

$$\delta\left[\Pi_0\int_0^1 \Phi\,\mathrm{d}\xi + \frac{1}{2}\int_0^1\left(\frac{\mathrm{d}\varphi}{\mathrm{d}\xi}\right)^2\mathrm{d}\xi - B\int_0^1 S(1+\varepsilon)\cos(\varphi-\alpha)\,\mathrm{d}\xi - C\cos\beta\int_0^1\left\{(1+\varepsilon)\cos\varphi - 1\right\}\mathrm{d}\xi - C\sin\beta\int_0^1(1+\varepsilon)\sin\varphi\,\mathrm{d}\xi\right] = 0 \tag{13}$$

In the normalized frame (ξ, η), the unknown deformation fields φ and ε are approximated as

$$\varphi = \sum_{i=1}^{nb} c_{1_i}\omega_i \tag{14a}$$

$$\varepsilon = \sum_{i=1}^{ns} c_{2_i}\psi_i \tag{14b}$$

where, c_{1_i} and c_{2_i} are the unknown coefficients to be computed, and ω_i and ψ_i are the sets of nb and ns number of coordinate functions chosen satisfying the kinematic boundary conditions. For the full-beam problem, the function sets are chosen by satisfying the boundary condition of Eq. (1) as

$$\omega_i = \sin(i\pi\xi) \tag{15a}$$

$$\psi_i = \cos\{(i-1)\pi\xi\} \tag{15b}$$

Whereas, for the HMS half-beam problem, the function sets as chosen through Eq. (2) are

$$\omega_i = \sin\left(\frac{2i-1}{2}\pi\xi\right) \tag{16a}$$

$$\psi_i = \cos\{(i-1)\pi\xi\} \tag{16b}$$

Now substituting the approximated deformation fields as presented in Eq. (14) into the governing equation (Eq. (13)) and carrying out the variational operation, we derive the final algebraic form of the governing equation as presented below.

$$[K]\{c\} = \{f\} \tag{17}$$

In the above equation, $[K]$, $\{c\}$, and $\{f\}$ denote stiffness matrix, set of unknown coefficients $\{c_{1_i}\ c_{2_i}\}^T$, and load vector for the large deformation of HMS beam problem respectively. The detailed expressions of the stiffness matrix $[K]$ and load vector $\{f\}$ are given below.

$$[K_{11}] = \sum_{j=1}^{nb}\sum_{i=1}^{nb}\int_0^1 \omega_i'\omega_j'\,\mathrm{d}\xi$$

$$[K_{12}] = \sum_{j=1}^{nb}\sum_{i=1}^{ns}\int_0^1\left[BS\sin\left(\sum_{k=1}^{nb}c_{1_k}\omega_k - \alpha\right) + C\cos\beta\sin\left(\sum_{k=1}^{nb}c_{1_k}\omega_k\right) - C\sin\beta\cos\left(\sum_{k=1}^{nb}c_{1_k}\omega_k\right)\right]\psi_i\omega_j\,\mathrm{d}\xi$$

$$[K_{21}] = [0]$$

$$[K_{22}] = \Pi_0\sum_{j=1}^{ns}\sum_{i=1}^{ns}\int_0^1 \bar{\sigma}_{N_c}\psi_i\psi_j\,\mathrm{d}\xi$$

$$\{f_1\} = \sum_{j=1}^{nb}\int_0^1\left[-BS\sin\left(\sum_{k=1}^{nb}c_{1_k}\omega_k - \alpha\right) - C\cos\beta\sin\left(\sum_{k=1}^{nb}c_{1_k}\omega_k\right) + C\sin\beta\cos\left(\sum_{k=1}^{nb}c_{1_k}\omega_k\right)\right]\omega_j\,\mathrm{d}\xi$$

$$\{f_2\} = \sum_{j=1}^{ns} \int_0^1 \left[BS\cos\left(\sum_{k=1}^{nb} c_{1_k}\omega_k - \alpha\right) + C\cos\beta\cos\left(\sum_{k=1}^{nb} c_{1_k}\omega_k\right) + C\sin\beta\sin\left(\sum_{k=1}^{nb} c_{1_k}\omega_k\right) - \Pi_0\bar{\sigma}_{N_c}\left\{1 - \frac{1}{\left(1+\sum_{k=1}^{ns} c_{2_k}\psi_k\right)^2}\right\}\right] \psi_j \, d\xi$$

where,

$$\bar{\sigma}_{N_c} = \frac{2}{E_s}\left[C_{10} + 2C_{20}\left\{\left(1+\sum_{k=1}^{ns} c_{2_k}\psi_k\right)^2 + \frac{2}{1+\sum_{k=1}^{ns} c_{2_k}\psi_k} - 3\right\} + 3C_{30}\left\{\left(1+\sum_{k=1}^{ns} c_{2_k}\psi_k\right)^2 + \frac{2}{1+\sum_{k=1}^{ns} c_{2_k}\psi_k} - 3\right\}^2\right]$$

2.2.2. Inextensible model

The governing equation (Eq. (17)) presented in the previous subsection is derived considering both the centreline rotation φ and centreline extension ε of the HMS beam. If we neglect the terms corresponding to the centreline strain ε from the elements of Eq. (17), we readily get the governing equation of the HMS beam deformation problem within the framework of the inextensible model. The elements of the stiffness matrix $[K]$ and the load vector $\{f\}$ for the inextensible model are presented below.

$$[K] = \sum_{j=1}^{nb}\sum_{i=1}^{nb} \int_0^1 \omega_i'\omega_j' \, d\xi$$

$$\{f\} = \sum_{j=1}^{nb} \int_0^1 \left[-BS\sin\left(\sum_{k=1}^{nb} c_{1_k}\omega_k - \alpha\right) - C\cos\beta\sin\left(\sum_{k=1}^{nb} c_{1_k}\omega_k\right) + C\sin\beta\cos\left(\sum_{k=1}^{nb} c_{1_k}\omega_k\right)\right] \omega_j \, d\xi$$

Note that the Inextensible model is computationally less intensive, but it also becomes less accurate for large deformation problems.

2.2.3. Iterative solution scheme

The elements of stiffness matrix $[K]$ and load vector $\{f\}$ of the governing equation (Eq. (17)), either derived through the extensible model or through the inextensible model, involve unknown coefficients $\{c\}$. However, the degree of such non-linearity is different for the extensible and inextensible models. Due to the involved non-linearity, the governing equation cannot be solved directly. Hence, an iterative computational scheme (Ghuku and Saha, 2019; Halpern et al., 2002) is developed to tackle the non-linearity involved in the governing equation.

Under an incremental step of non-dimensional mechanical load C with the inclination angle β, the non-dimensional magnetic load B is applied incrementally by a ratio r which is termed as magnetic load ratio and defined by

$$r = \frac{B}{C} \tag{18}$$

Hence, the inputs of the beam model are the magnitude of the non-dimensional mechanical load C with its inclination angle β and the magnetic load ratio r along with the coefficient of the residual magnetic flux density $S(\xi)$ and the inclination angle of the external magnetic field α.

At the incremental step of the non-dimensional mechanical load C and magnetic load $B = rC$, the iterative solution process to find the set of unknown coefficients $\{c\}$ starts with assumed set of the coefficients denoted as $\{c\}^{i-1}$, where the superscript i denotes the iteration number. With the assumed set of the unknown coefficients $\{c\}^{i-1}$, elements of the stiffness matrix $[K]^i$ and load vector $\{f\}^i$ at the current iteration step i are computed. With the known $[K]^i$ and $\{f\}^i$, the set of unknown coefficients $\{c\}^i$ are computed through the matrix inversion of the governing equation (Eq. (17)) as

$$\{c\}^i = \left[[K]^{-1}\right]^i \{f\}^i \tag{19}$$

The set of coefficients $\{c\}^i$ computed through the above equation, is compared with its old values $\{c\}^{i-1}$ as $\mu = \{c\}^i - \{c\}^{i-1}$. Until the error μ becomes less than its predefined limit, the set of unknown coefficient $\{c\}^{i+1}$ is updated through the successive relaxation scheme presented below and the next iteration $(i+1)$ begins.

$$\{c\}^{i+1} = \lambda\{c\}^i + (1-\lambda)\{c\}^{i-1} \tag{20}$$

In the above equation, λ denotes the relaxation parameter for the successive relaxation scheme which lies between 0 to 1. The iterative scheme to compute the large deformation characteristics of the HMS beam under combined mechanical load and magnetic field is presented in Algorithm 1.

Algorithm 1: Beam-level computational algorithm to obtain large deformation characteristics of HMS beam under combined mechanical load and magnetic field.

Define geometry: Define non-dimensional geometric specification of the HMS beam Π_0.

Define material property: Define the material constitutive parameters C_{10}, C_{20}, and C_{30} in the framework of Yeoh hyperelastic model.

Define numerical parameters: Define the numerical values of the computational parameters λ, μ, nb, and ns.

Generate: Generate the set of coordinate functions ω_i and ψ_i through satisfaction of the boundary conditions of the HMS beam problem under consideration.

Input load: Input the magnitude of the non-dimensional mechanical load C and magnetic load B in terms of the magnetic load ratio r as $B = rC$, along with their orientation angles β and α.

Iterate: The iterative computational scheme to obtain the set of unknown coefficients $\{c\}$ from the non-linear governing equation $[K]\{c\} = \{f\}$ involves the following steps:

- Initialize the set of unknown coefficients denoted as $\{c\}^{i-1}$.
- Compute the stiffness matrix $[K]^i$ involving the set of unknown coefficients $\{c\}^{i-1}$.
- Compute the load vector $\{f\}^i$ involving the set of unknown coefficients $\{c\}^{i-1}$ under the current step of combined mechanical and magnetic loads.
- Compute the set of unknown coefficients as $\{c\}^i = \left[[K]^{-1}\right]^i \{f\}^i$.
- Compare the computed set $\{c\}^i$ with its old values $\{c\}^{i-1}$ defined as $\mu = \{c\}^i - \{c\}^{i-1}$.
- Until the error μ becomes less than its predefined limit, the set of coefficients is updated by $\{c\}^{i+1} = \lambda\{c\}^i + (1-\lambda)\{c\}^{i-1}$ and go for the next iteration $i+1$.

Note output: Once the set of unknown coefficients $\{c\}$ is obtained through the iterative computational scheme, the centreline rotation φ and the centreline strain ε become known which in turn give the non-dimensional deflection profile (ξ, η) and the tip-deflections $\bar{\delta}_x$ and $\bar{\delta}_y$.

Once the set of unknown coefficients $\{c\}$ for the current combined load step C and B is obtained through the iterative computational scheme, the centreline rotation φ and the centreline strain ε become

known from Eq. (14) for the extensible model. Whereas, for the inextensible model, only the centreline rotation φ is obtained. With the known deformation components (φ and ε), the deflection profile (x, y) of the HMS beam is obtained which in turn provides axial deflection δ_x and transverse deflection δ_y of the tip of the beam. The expressions of the axial and transverse tip-deflections (δ_x and δ_y) in the normalized form as obtained from Eq. (4) are given below for the extensible model.

$$\bar{\delta}_x = \frac{\delta_x}{L} = \int_0^1 \left\{ (1+\varepsilon)\cos\varphi - 1 \right\} \mathrm{d}\xi \tag{21a}$$

$$\bar{\delta}_y = \frac{\delta_y}{L} = \int_0^1 (1+\varepsilon)\sin\varphi \, \mathrm{d}\xi \tag{21b}$$

For the inextensible model, the normalized tip-deflections ($\bar{\delta}_x$ and $\bar{\delta}_y$) are obtained from the above equation by neglecting the ε terms as

$$\bar{\delta}_x = \frac{\delta_x}{L} = \int_0^1 (\cos\varphi - 1) \, \mathrm{d}\xi \tag{22a}$$

$$\bar{\delta}_y = \frac{\delta_y}{L} = \int_0^1 \sin\varphi \, \mathrm{d}\xi \tag{22b}$$

Using the beam-level tip-deflections, we compute unit cell level strains under a given far-field mechanical stress and magnetic field, as discussed in the following subsections considering different lattice geometries.

2.3. Effective elastic moduli of hexagonal HMS beam networks

2.3.1. Beam-level forces and deformation kinematics

As described in Fig. 1, the chosen unit cell in hexagonal lattices consists of three HMS beams having residual magnetic flux density B_0^r concerning the initial configuration. The beam-level forces developed under the two different combinations of normal stress and magnetic fields as shown in Fig. 2(a) and (d), and under the combination of shear stress with the magnetic field as shown in Fig. 3(a), along with the large deformation kinematics of the HMS beam elements are described in the following three subsections.

2.3.1.1. Mechanical normal stress along direction-1 and magnetic field along direction-2. Under the combined mechanical stress σ_1 and magnetic field B^a as shown in Fig. 2(a), the inclined HMS beams (OA and OB) undergo combined transverse and axial deformations with fixed end O and the other end A and B being rotationally restrained but free to translation. Whereas the vertical member OC undergoes axial deformation only with fixed end C. Due to symmetry, we concentrate on one inclined member (OA) only along with the vertical member OC. The large deformation kinematics of the inclined member OA and the vertical member OC are shown concerning the local Cartesian frames (x, y) in Fig. 2(b) and (c) respectively. The kinematic boundary conditions of the beam members are conceptualized from the classical deformation analysis of conventional honeycomb lattices under mechanical stress only (Gibson and Ashby, 1999). Note that due to deformations of the HMS members as shown in Fig. 2(b) and (c), the residual magnetic flux density changes from B_0^r to B^r.

As shown in Fig. 2(b), the inclined HMS beam OA is subjected to tip concentrated force F_i developed due to the applied stress field σ_1. Expression of F_i in terms of σ_1 is given by

$$F_i = \sigma_1 b(h + l\sin\theta) \tag{23}$$

The above-presented force F_i is inclined by the angle β_i concerning the local Cartesian frame (x, y) as shown in Fig. 2(b). Whereas, the inclination angle of the magnetic field B_a concerning the local frame (x, y) is denoted by α_i. The inclination angles are expressed in terms of the inclination angle θ of the inclined member of the beam network as

$$\beta_i = \pi - \theta \tag{24a}$$

$$\alpha_i = \frac{3\pi}{2} - \theta \tag{24b}$$

As shown in Fig. 2(c), the vertical HMS beam OC is not subjected to any mechanical load but subjected to magnetic field B^a only with inclination angle α_v. For the vertical HMS beam OC, the kinetic equations similar to Eqs. (23) and (24) are presented below respectively.

$$F_v = 0 \tag{25}$$

$$\alpha_v = \pi \tag{26}$$

2.3.1.2. Mechanical normal stress along direction-2 and magnetic field along direction-2. When the unit cell is subjected to far-field mechanical stress along direction-2 (i.e. σ_2) along with the magnetic field B^a as shown in Fig. 2(d), the kinematic boundary conditions of the HMS members remain the same as in the case of combined loading σ_1 and B^a considered in the previous subsection. The large deformation patterns of the inclined member OA and the vertical member OC concerning the local Cartesian frames (x, y) are shown in Fig. 2(e) and (f) respectively. The tip concentrated force F_i developed in the inclined member due to the mechanical stress field σ_2 is expressed in terms of σ_2 as

$$F_i = \sigma_2 bl\cos\theta \tag{27}$$

The inclination angles of the mechanical load F_i and the magnetic field B_a concerning the local frame (x, y) are expressed in terms of the inclination angle θ as (refer to Fig. 2(e))

$$\beta_i = \alpha_i = \frac{3\pi}{2} - \theta \tag{28}$$

The vertical HMS beam OC is subjected to mechanical concentrated force F_v in addition to the uniform magnetic field B^a as shown in Fig. 2(f). Expression of the force F_v in terms of the remote stress σ_2 is given by

$$F_v = 2\sigma_2 bl\cos\theta \tag{29}$$

The inclination angles of the mechanical force F_v and the magnetic field B^a concerning the local frame (x, y) are given by

$$\beta_v = \alpha_v = \pi \tag{30}$$

2.3.1.3. Mechanical shear stress in 1–2 plane and magnetic field along direction-2. Under the combined shear stress τ and the magnetic field B^a as shown in Fig. 3(a), the developed forces and end moments at the HMS beam members are shown through free body diagrams in Fig. 3(b). The forces F_1 and F_2 developed due to the far-field mechanical shear stress τ are expressed as

$$F_1 = 2\tau bl\cos\theta \tag{31a}$$

$$F_2 = \tau b(h + l\sin\theta) \tag{31b}$$

From the moment balance condition concerning point O (refer to Fig. 3(b)), the induced moment M in the inclined members are found to be $M = F_1 h/4$. Using Eq. (31a), the end moment M is expressed in terms of the remote stress τ as given below.

$$M = \frac{1}{2}\tau blh\cos\theta \tag{32}$$

Under the mechanical forces and end moments in combination with the magnetic field, all the HMS beam members (OA, OB, and OC) undergo combined axial and transverse deformations with fixed end O and the other ends (A, B, and C) being rotationally restrained but free to translation. The large deformation patterns of the inclined (OA and OB) and vertical (OC) members of the HMS unit cell concerning the corresponding local Cartesian frames (x, y) are shown in Fig. 3(c), (d), and (e) respectively. Though the deformed geometries of the inclined members OA and OB look asymmetric, they behave structurally (i.e. visually asymmetric, but structurally symmetric) the same under the combined mechanical and magnetic field due to the opposite direction of the residual magnetic flux density B_0^r in them. Hence, we consider the mechanics of one inclined member (OA) along with the

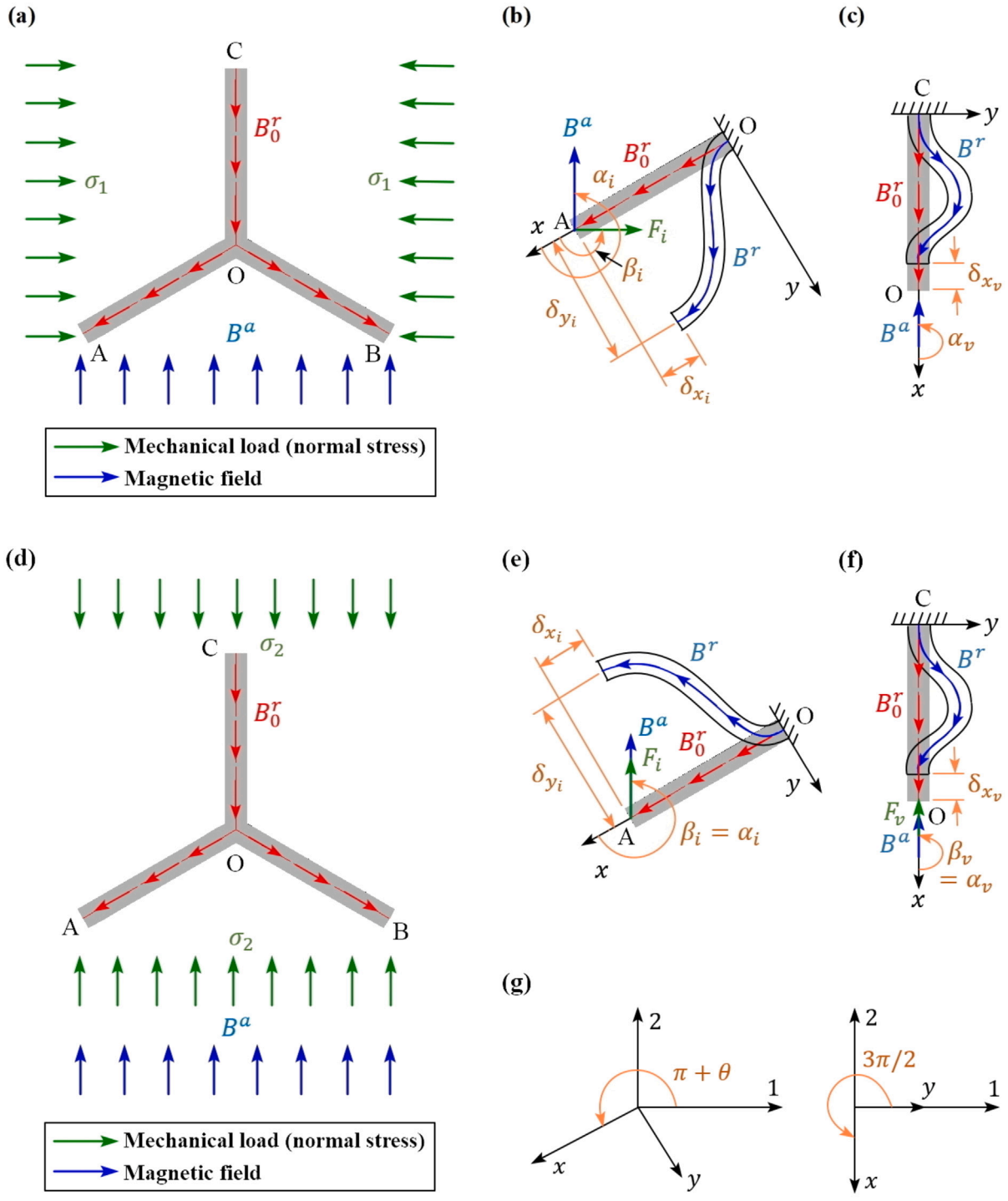

Fig. 2. Multi-physical mechanics of periodic hexagonal HMS beam networks under combined mechanical normal stress and magnetic field. (a) Combined loading mode of the unit cell of hexagonal HMS beam network subjected to normal stress along direction-1 (σ_1) and magnetic field along direction-2 (B^a). **(b, c)** Beam-level forces and large deformation kinematics of the inclined and vertical members of the unit cell under the combined normal stress σ_1 and magnetic field B^a. Note that under the combined loading condition (a–c), we focus on the longitudinal effective Young's modulus E_1 and Poisson's ratio ν_{12} of the HMS beam network. **(d)** Combined loading mode of the unit cell of hexagonal HMS beam network subjected to mechanical normal stress along direction-2 (σ_2) and magnetic field along direction-2 (B^a). **(e, f)** Beam-level forces and large deformation kinematics of the inclined and vertical members of the unit cell under the combined normal stress σ_2 and magnetic field B^a. Note that under the combined loading condition (d–f), we focus on the transverse Young's modulus E_2 and Poisson's ratio ν_{21} of the HMS beam network. **(g)** Local coordinate systems (x, y) for the inclined and vertical members and their orientations with the global frame (1, 2).

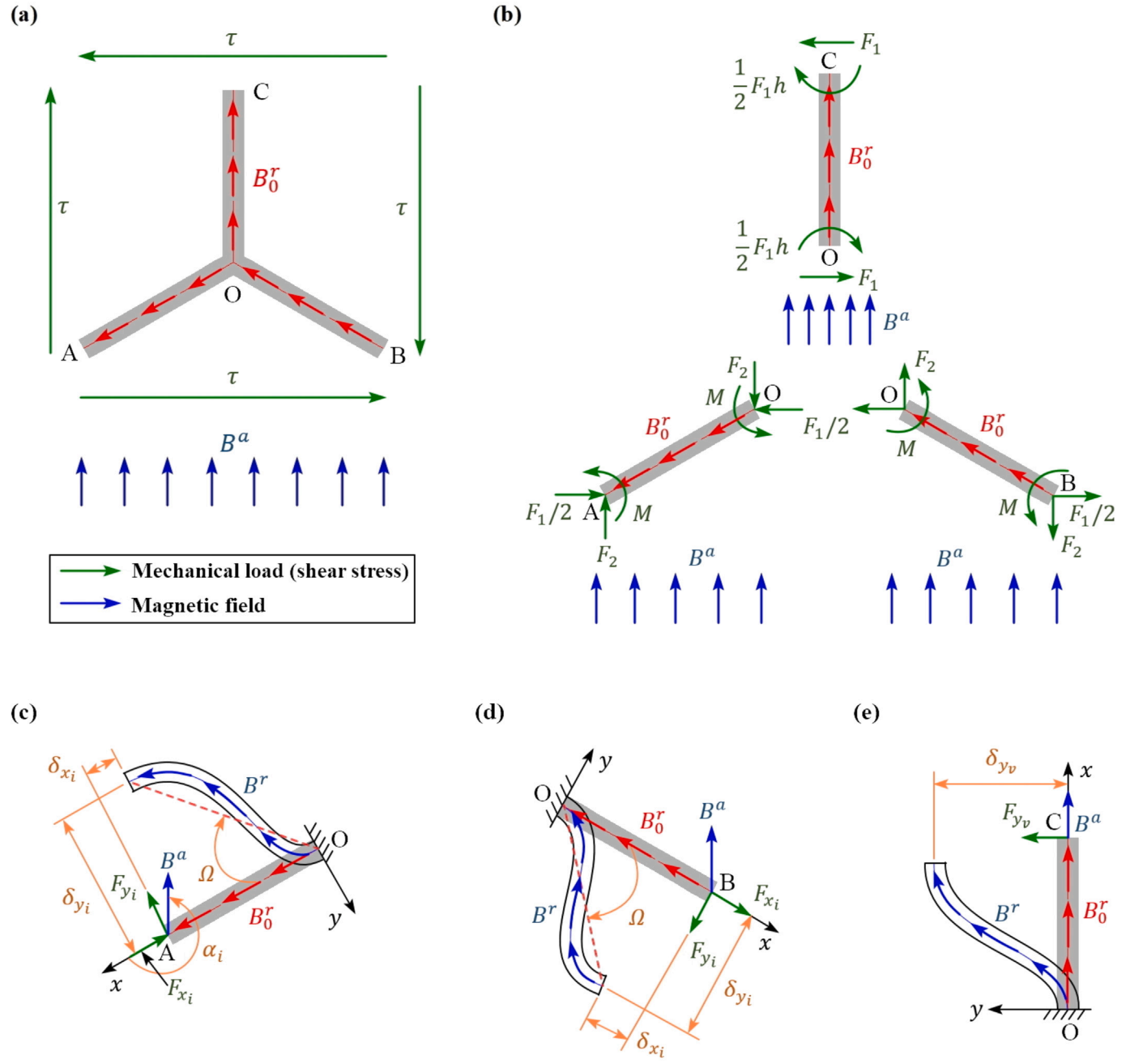

Fig. 3. Multi-physical mechanics of periodic hexagonal HMS beam networks under combined mechanical shear stress and magnetic field. (a) Combined loading mode of the unit cell of hexagonal HMS beam network subjected to shear stress in 1–2 plane (τ) and magnetic field along direction-2 (B^a). **(b)** Free body diagrams of the inclined and vertical members of the unit cell under the combined in-plane shear stress τ and magnetic field B^a. **(c–e)** Beam-level forces and large deformation kinematics of the inclined and vertical members of the unit cell. Note that under this combined loading condition, we focus on the in-plane shear modulus G_{12} of the HMS beam network.

vertical member OC. In this context, it may be further emphasized that the direction of residual flux densities B_0^r is architected differently under normal and shear far-field stresses (refer to Figs. 2(a, d) and 3(a)) to maintain structural symmetry in the deformation behaviour. Here if we keep the distribution of residual flux densities B_0^r same for both the far-field normal and shear stresses, the analysis will involve structural asymmetry in any one of cases of far-field stress, leading to more involved unit cell level derivation to distribute unbalanced stress resultants at joint O. In the current paper, we have focused on demonstrating the concepts of active elasticity modulation rather than increasing unit cell level structural complexity.

The beam-level transverse force F_{y_i} for the inclined member OA as shown in Fig. 3(c), is the equivalent force of the end moment M derived following the typical rotationally restrained boundary condition of the member OA as given by $F_{y_i} = -2M/l$. Whereas, the axial force F_{x_i} is obtained from the components of F_1 and F_2 along OA as given by $F_{x_i} = -(F_1/2)\cos\theta - F_2\sin\theta$. Using Eqs. (31) and (32), the beam-level forces are expressed in terms of the applied remote shear stress τ as

$$F_{x_i} = -\tau bl\left\{\cos^2\theta + \left(\frac{h}{l} + \sin\theta\right)\sin\theta\right\} \tag{33a}$$

$$F_{y_i} = -\tau bh\cos\theta \tag{33b}$$

The inclination angle α_i of the externally applied magnetic field B^a (refer to Fig. 3(c)) is given in terms of the inclination angle θ as

$$\alpha_i = \frac{3\pi}{2} - \theta \tag{34}$$

As shown in Fig. 3(e), the vertical HMS beam member OC is subjected to transverse force F_{y_v} which is given by $F_{y_v} = F_1$. Hence, the expression of the transverse force F_{y_v} in terms of the remote stress τ is obvious from Eq. (31a) as

$$F_{y_v} = 2\tau bl\cos\theta \tag{35}$$

In addition to the above presented mechanical force, the vertical HMS beam member OC is subjected to the vertical magnetic field B^a, inclination angle of which concerning the local Cartesian frame (x, y) is obvious from Fig. 3(e) as given below.

$$\alpha_v = 0 \tag{36}$$

2.3.2. Effective elastic moduli

The beam model presented in the previous subsection gives non-dimensional deformation characteristics ($\bar{\delta}_x$ and $\bar{\delta}_y$) of HMS beam with non-dimensional geometric specification Π_0 for the inputs of normalized mechanical load C and magnetic load B in terms of magnetic load ratio r as $B = rC$ along with their orientation angles β and α respectively. To use the beam model for the estimation of elastic moduli of hexagonal HMS beam networks following a unit cell approach (refer to Figs. 2 and 3), the geometric specifications and loading terms of the HMS beam network need to be defined in non-dimensional forms. The non-dimensional geometric specifications of the inclined (Π_{0_i}) and vertical (Π_{0_v}) members of the HMS beam network are defined following Eq. (12) as

$$\Pi_{0_i} = \frac{12}{\left(\frac{t}{l}\right)^2} \tag{37a}$$

$$\Pi_{0_v} = \frac{12\left(\frac{h}{l}\right)^2}{\left(\frac{t}{l}\right)^2} \tag{37b}$$

Under any mode of the applied far-field mechanical stress (σ_1 or σ_2 or τ), non-dimensional mechanical force for the inclined (C_i) and vertical (C_v) members of the HMS beam network can be obtained following Eq. (12) from the beam-level forces (F_i and F_v) presented in Section 2.3.1. Such expressions of the non-dimensional mechanical loads C_i and C_v in terms of the applied stress (σ_1 or σ_2 or τ) are presented in the subsequent subsections for the three different combinations of mechanical and magnetic loads. Under the defined non-dimensional mechanical load C_i for a particular combination of mechanical and magnetic loads, the non-dimensional magnetic load B_i of the inclined member is defined in terms of the magnetic load ratio r_i as

$$r_i = \frac{B_i}{C_i} \tag{38}$$

With the known non-dimensional magnetic load B_i from the above equation, the non-dimensional magnetic load B_v of the vertical member becomes known once we know the relationship between B_i and B_v. To derive such a relationship between B_i and B_v, let us observe their definitions from Eq. (12) as given below.

$$B_i = \frac{\left|B_0^r\right| |B^a| \Pi_{0_i}}{E_s \mu_0} \tag{39a}$$

$$B_v = \frac{\left|B_0^r\right| |B^a| \Pi_{0_v}}{E_s \mu_0} \tag{39b}$$

Using Eq. (37), the relationship between B_i and B_v is obtained from the above equation which gives the non-dimensional magnetic load B_v in terms of B_i as presented below.

$$B_v = \left(\frac{h}{l}\right)^2 B_i \tag{40}$$

Now, with the defined non-dimensional geometric and load parameters, the non-dimensional tip-deflections $\bar{\delta}_x$ and $\bar{\delta}_y$ of the members of the hexagonal HMS beam network are obtained from the generalized beam model which in turn give the non-linear effective elastic moduli following the framework of the unit cell approach. Derivations of the effective elastic moduli for the three different combinations of mechanical and magnetic loads are presented in the following three subsections. In addition, non-dimensional forms of the effective elastic moduli are defined subsequently.

2.3.2.1. Computation of E_1 and ν_{12} under combined load σ_1 and B^a.

Under the combined loading of mechanical far-field normal stress σ_1 and magnetic field B^a as shown in Fig. 2(a–c), the non-dimensional mechanical loads C_i and C_v are derived using Eqs. (23), (25) and (12) as given by

$$C_i = \frac{12\left(\frac{h}{l} + \sin\theta\right)}{E_s\left(\frac{t}{l}\right)^3}\sigma_1 \tag{41a}$$

$$C_v = 0 \tag{41b}$$

With the above-presented non-dimensional mechanical loads C_i and C_v under normal stress σ_1, the non-dimensional magnetic loads B_i and B_v are defined in terms of the magnetic load ratio r_i using Eqs. (38) and (40). With the defined mechanical and magnetic loads along with their orientation angles (Eqs. (24) and (26)), the non-dimensional tip-deflections of the inclined member ($\bar{\delta}_{x_i}$ and $\bar{\delta}_{y_i}$) and the vertical member ($\bar{\delta}_{x_v}$) of the unit cell of hexagonal HMS beam network (refer to Fig. 2(b) and (c)) are obtained with respect to the local Cartesian frames (x, y) based on the generalized beam model presented in Section 2.2. Through the coordinate transformation between the local frames (x, y) and the global frame (1, 2) as shown in Fig. 2(g), the resultant deflection along direction-1 (δ_1) and direction-2 (δ_2) are obtained as

$$\delta_1 = l\left(-\bar{\delta}_{x_i}\cos\theta + \bar{\delta}_{y_i}\sin\theta\right) \tag{42}$$

$$\delta_2 = -l\left(\bar{\delta}_{x_i}\sin\theta + \bar{\delta}_{y_i}\cos\theta\right) - h\bar{\delta}_{x_v} \tag{43}$$

The normal strain developed along direction-1 under the combined loading σ_1 and B^a is obtained by $\epsilon_1 = \delta_1/l\cos\theta$, using Eq. (42) which becomes

$$\epsilon_1 = \frac{-\bar{\delta}_{x_i}\cos\theta + \bar{\delta}_{y_i}\sin\theta}{\cos\theta} \tag{44}$$

Similarly, the normal strain along direction-2 is obtained by $\epsilon_2 = \delta_2/(h + l\sin\theta)$, using Eq. (43) which becomes

$$\epsilon_2 = \frac{-\bar{\delta}_{x_i}\sin\theta - \bar{\delta}_{y_i}\cos\theta - \frac{h}{l}\bar{\delta}_{x_v}}{\frac{h}{l} + \sin\theta} \tag{45}$$

The longitudinal effective Young's modulus of the hexagonal HMS beam network is obtained from its fundamental definition $E_1 = \sigma_1/\epsilon_1$ using Eq. (44) as

$$E_1 = \frac{\sigma_1\cos\theta}{-\bar{\delta}_{x_i}\cos\theta + \bar{\delta}_{y_i}\sin\theta} \tag{46}$$

The effective Poisson's ratio ν_{12} of the HMS beam network under the combined loading σ_1 and B^a is obtained by the definition $\nu_{12} = -\epsilon_2/\epsilon_1$, using Eqs. (44) and (45) which becomes

$$\nu_{12} = \frac{\left(\bar{\delta}_{x_i}\sin\theta + \bar{\delta}_{y_i}\cos\theta + \frac{h}{l}\bar{\delta}_{x_v}\right)\cos\theta}{\left(\frac{h}{l} + \sin\theta\right)\left(-\bar{\delta}_{x_i}\cos\theta + \bar{\delta}_{y_i}\sin\theta\right)} \tag{47}$$

The solution steps involved in the computation of the non-linear effective elastic moduli E_1 and ν_{12} of the hexagonal HMS beam network using the beam model are presented in Algorithm 2. Note that the solution algorithm is generic and is applicable to the computations of effective elastic moduli under all the three combined loading conditions of the magnetic field and different far-field mechanical stresses.

Algorithm 2: Beam network-level computational algorithm to obtain non-linear effective elastic moduli of periodic HMS beam networks under combined mechanical stress and magnetic field.

Define geometry: Define non-dimensional geometric parameters of the HMS beam network (such as t/l, h/l, and θ for hexagonal lattices). With the defined lattice parameters, compute the geometric specifications of the constituting inclined and vertical HMS beams Π_{0_i} and Π_{0_v}.

Define mechanical load: Under a particular mode of applied mechanical stress (σ_1 or σ_2 or τ), define the non-dimensional mechanical force for the inclined and vertical HMS beams C_i and C_v along with their inclination angles β_i and β_v.

Define magnetic load: Define the magnetic load ratio r_i for the inclined HMS beam. Compute the non-dimensional magnetic load of the inclined member in terms of r_i and C_i as $B_i = r_i C_i$. Compute magnetic load of the vertical member as $B_v = (h/l)^2 B_i$ along with the inclination angles α_i and α_v.

Compute beam deflections: Under the combined mechanical and magnetic loads, compute non-dimensional tip-deflections of the inclined and vertical HMS beams $\bar{\delta}_{x_i}$, $\bar{\delta}_{y_i}$, $\bar{\delta}_{x_v}$, and $\bar{\delta}_{y_v}$ through solution Algorithm 1.

Compute effective elastic moduli: In terms of the tip-deflections $\bar{\delta}_{x_i}$, $\bar{\delta}_{y_i}$, $\bar{\delta}_{x_v}$ and $\bar{\delta}_{y_v}$, compute the effective elastic moduli (E_1, ν_{12}, E_2, ν_{21}, and G_{12}) of the periodic HMS beam network under the corresponding mode of mechanical stress in combination with the magnetic field.

2.3.2.2. Computation of E_2 and ν_{21} under combined load σ_2 and B^a. Under the applied normal far-field stress along direction-2 (σ_2) in combination with the magnetic field B^a as shown in Fig. 2(d)–(f), the non-dimensional mechanical force for the inclined (C_i) and vertical (C_v) members of the HMS unit cell are obtained in terms of σ_2 using Eqs. (27) and (29) through the normalization scheme of Eq. (12) as

$$C_i = \frac{12\cos\theta}{E_s\left(\frac{t}{l}\right)^3}\sigma_2 \tag{48a}$$

$$C_v = \frac{24\left(\frac{h}{l}\right)^2\cos\theta}{E_s\left(\frac{t}{l}\right)^3}\sigma_2 \tag{48b}$$

The non-dimensional magnetic loads B_i and B_v are defined in terms of the magnetic load ratio r_i and the mechanical load C_i using Eqs. (38) and (40). The inclination angles of the mechanical and magnetic loads (β_i, α_i, β_v, and α_v) are given in Eqs. (28) and (30). With the defined input parameters, the tip-deflections of the HMS beam members $\bar{\delta}_{x_i}$, $\bar{\delta}_{y_i}$, and $\bar{\delta}_{x_v}$ are computed through the generalized beam model. As the coordinate systems for the current load combination of σ_2 and B^a is the same with the load combination of σ_1 and B^a (refer to Fig. 2), the expressions of the deflections δ_1 and δ_2, and the normal strains ϵ_1 and ϵ_2 are the same as presented in Eqs. (42)–(45). Hence, the equations are not repeated here to maintain brevity of the paper.

The transverse effective Young's modulus E_2 of the hexagonal HMS beam network is defined as $E_2 = \sigma_2/\epsilon_2$. Using Eq. (45), the final expression of the Young's modulus E_2 is obtained in terms of the beam-level deflections as

$$E_2 = \frac{\sigma_2\left(\frac{h}{l}+\sin\theta\right)}{-\bar{\delta}_{x_i}\sin\theta - \bar{\delta}_{y_i}\cos\theta - \frac{h}{l}\bar{\delta}_{x_v}} \tag{49}$$

Using the strain expressions presented in Eqs. (44) and (45), the effective Poisson's ratio of the hexagonal HMS beam network is obtained through its fundamental definition $\nu_{21} = -\epsilon_1/\epsilon_2$ as

$$\nu_{21} = \frac{\left(\frac{h}{l}+\sin\theta\right)\left(-\bar{\delta}_{x_i}\cos\theta + \bar{\delta}_{y_i}\sin\theta\right)}{\left(\bar{\delta}_{x_i}\sin\theta + \bar{\delta}_{y_i}\cos\theta + \frac{h}{l}\bar{\delta}_{x_v}\right)\cos\theta} \tag{50}$$

2.3.2.3. Computation of G_{12} under combined load τ and B^a. Under the combined loading condition of the shear mode of mechanical stress (τ) and magnetic field B^a along direction-2 as shown in Fig. 3, components of the non-dimensional mechanical force C_i for the inclined member of the HMS unit cell are obtained using Eqs. (33) and (12) as given below.

$$\bar{F}_{x_i} = C_i\cos\beta_i = -\frac{12\left\{\cos^2\theta + \left(\frac{h}{l}+\sin\theta\right)\sin\theta\right\}}{E_s\left(\frac{t}{l}\right)^3}\tau \tag{51a}$$

$$\bar{F}_{y_i} = C_i\sin\beta_i = -\frac{12\left(\frac{h}{l}\right)\cos\theta}{E_s\left(\frac{t}{l}\right)^3}\tau \tag{51b}$$

From the above set of equations, the non-dimensional mechanical force C_i along with its orientation angle β_i can be obtained. In terms of the mechanical load C_i and the required magnetic load ratio r_i, the non-dimensional magnetic loads B_i and B_v are defined using Eqs. (38) and (40) having the orientation angles α_i and α_v as defined in Eqs. (34) and (36). On the other hand, non-dimensional form of the transverse mechanical force F_{y_v} having orientation angle $\beta_v = \pi/2$ (refer to Fig. 3) is derived from Eqs. (35) and (12) as

$$\bar{F}_{y_v} = C_v = \frac{24\left(\frac{h}{l}\right)^2\cos\theta}{E_s\left(\frac{t}{l}\right)^3}\tau \tag{52}$$

Under the prescribed combined mechanical and magnetic loading, rotation Ω of the inclined member of the HMS unit cell (refer to Fig. 3(c)) is obtained from the generalized beam model as

$$\Omega = -\bar{\delta}_{y_i} \tag{53}$$

Total horizontal shear deflection at point C (δ_{1_C}) comprises of the deflection of the vertical member OC (δ_{y_v}) and the deflection component due to the rotation Ω (refer to Fig. 3(c) and (e)) defined as $\delta_{1_C} = h\Omega + h\bar{\delta}_{y_v}$. Using Eq. (53), the shear deflection δ_{1_C} is obtained as

$$\delta_{1_C} = h\left(-\bar{\delta}_{y_i} + \bar{\delta}_{y_v}\right) \tag{54}$$

The horizontal and vertical components of the axial deflection δ_{x_i} at point A of the inclined member (refer to Fig. 3(c)) are obtained through a coordinate transformation as given by

$$\delta_{1_A} = -l\bar{\delta}_{x_i}\cos\theta \tag{55a}$$

$$\delta_{2_A} = -l\bar{\delta}_{x_i}\sin\theta \tag{55b}$$

Due to the deflections as presented in Eqs. (54) and (55), the total shear strain developed in the HMS unit cell under the combined loading of τ and B^a is given by

$$\gamma_{12} = \frac{\delta_{1_C}+\delta_{1_A}}{h + l\sin\theta} + \frac{\delta_{2_A}}{l\cos\theta} = \frac{\frac{h}{l}\left(-\bar{\delta}_{y_i}+\bar{\delta}_{y_v}\right) - \bar{\delta}_{x_i}\cos\theta}{\frac{h}{l}+\sin\theta} - \frac{\bar{\delta}_{x_i}\sin\theta}{\cos\theta} \tag{56}$$

The effective shear modulus G_{12} of the hexagonal HMS beam network under the combined loading τ and B^a is defined in terms of the developed shear strain as $G_{12} = \tau/\gamma_{12}$. Using the expression of the shear strain as presented in Eq. (56), we get the final form of G_{12} as shown below.

$$G_{12} = \frac{\tau\left(\frac{h}{l}+\sin\theta\right)\cos\theta}{\frac{h}{l}\left(-\bar{\delta}_{y_i}+\bar{\delta}_{y_v}\right)\cos\theta - \bar{\delta}_{x_i}\cos^2\theta - \bar{\delta}_{x_i}\left(\frac{h}{l}+\sin\theta\right)\sin\theta} \tag{57}$$

From the expressions of effective elastic moduli presented in Eqs. (46), (47), (49), (50) and (57) (and subsequently considering the dependencies of the tip deflections), we notice nonlinear dependency of the moduli on applied magnetic field and far-field stress, along with unit cell geometry, intrinsic material properties and residual magnetic

flux architecture. Such complex interplay of the influencing parameters in an expanded design space provides a unique scope of designing novel metamaterial functionalities with unprecedented mechanical behaviour.

2.3.2.4. Non-dimensional elastic moduli. To observe the effect of non-linearity along with the incremental effect of the magnetic field with the applied mechanical load on the hexagonal HMS beam network explicitly, we present the effective elastic moduli in specific forms. Among the five elastic moduli, the Poisson's ratios ν_{12} and ν_{21} are already in non-dimensional forms. Hence, they are presented in their original forms. Whereas, the other three effective elastic moduli of the HMS beam network (E_1, E_2, and G_{12}) are expressed in non-dimensional forms as given below.

$$\bar{E}_1 = \frac{E_1}{E_s\rho^3},\ \bar{E}_2 = \frac{E_2}{E_s\rho^3},\ \bar{G}_{12} = \frac{G_{12}}{E_s\rho^3} \tag{58}$$

where, ρ is the relative density of the hexagonal HMS beam network defined as the ratio of the volume of the total intrinsic HMS material and the volume of the equivalent plate-like object that the hexagonal HMS beam network acquires (Gibson and Ashby, 1999). Expression of the relative density ρ is given by

$$\rho = \frac{\left(\frac{h}{l}+2\right)\frac{t}{l}}{2\left(\frac{h}{l}+\sin\theta\right)\cos\theta} \tag{59}$$

2.3.2.5. Note on different lattice architectures. For the hexagonal network of HMS beams, a detailed derivation of the non-linear effective elastic moduli within the multi-physical mechanics-based semi-analytical framework is presented in this subsection. To demonstrate the generality of the physically insightful framework, non-linear effective elastic properties of five other HMS beam networks, namely, auxetic, rectangular brick, rhombic, triangular, and rectangular configurations are also analysed within the broad framework (refer to Fig. 1(g)). Among the considered five other forms of HMS beam networks, the effective elastic moduli of the auxetic, rectangular brick, and rhombic configurations are readily obtained from the framework for hexagonal HMS beam network by properly selecting the geometric parameters h/l and θ (note: for auxetic configuration θ is negative, for rectangular brick configuration θ is zero, for rhombic configuration h/l is zero). However, for the triangular and rectangular HMS beam networks, the appropriate unit cells need to be chosen and analysed separately. The detailed derivations of the non-linear elastic moduli for the triangular and rectangular HMS beam networks are presented in the following subsections. Note that under the influence of combined far-field mechanical stresses and magnetic field, the unit cell mechanics of different lattice configurations becomes significantly involved (due to combined bending and stretching dominance in a multi-physical environment) that has not been investigated in the literature.

2.4. Effective elastic moduli of triangular HMS beam networks

The non-linear effective elastic moduli E_1, ν_{12}, E_2, ν_{21}, and G_{12} of a triangular network of HMS beams, as shown in Fig. 1(g)IV, under different modes of far-field mechanical stress (σ_1, σ_2, and τ) in combination with the magnetic field B^a are derived in this subsection. The unit cell of the triangular HMS beam network is an equilateral triangle with side l having residual magnetic flux density B_0^r. The combined loading conditions for the triangular HMS unit cell under the longitudinal and transverse normal stresses σ_1 and σ_2 in combination with the magnetic field B^a along direction-2 are shown in Fig. 4(a) and (b) respectively. Whereas, the combined loading condition under the in-plane shear stress τ and the magnetic field B^a for the triangular HMS unit cell is shown in Fig. 4(d). Note in Fig. 4(d) that the direction of residual magnetic flux density B_0^r for the inclined members OB and AB is opposite (unlike the unit cells considered under far-field normal stresses). This opposite distribution of B_0^r makes the members OB and AB structurally symmetric under the in-plane shear stress τ in combination with external magnetic field B^a. This phenomenon is already described in detail for the hexagonal HMS beam network and is not repeated here to maintain brevity.

Under only far-field mechanical stress (σ_1, σ_2, and τ) in absence of magnetic field B^a, the cell members undergo stretch-dominated deformations (Gibson and Ashby, 1999). Hence, the effective elastic moduli of the triangular lattice configurations under mechanical load only are governed by the axial deformations of the members (Wang and McDowell, 2004). The analytical formulae for the effective elastic moduli of triangular lattices (with cell wall thickness t) under mechanical load only within small deformation regime are given by (Gibson and Ashby, 1999; Wang and McDowell, 2004)

$$\frac{E_1}{E_s} = \frac{E_2}{E_s} = \frac{2}{\sqrt{3}}\frac{t}{l} \tag{60a}$$

$$\nu_{12} = \nu_{21} = \frac{1}{3} \tag{60b}$$

$$\frac{G_{12}}{E_s} = \frac{\sqrt{3}}{4}\frac{t}{l} \tag{60c}$$

In this subsection, the conventional unit cell-based approach for triangular lattices (Gibson and Ashby, 1999; Wang and McDowell, 2004) is extended to a magneto-active multi-physical mechanics-based semi-analytical framework following the formulation for hexagonal HMS beam network presented in the preceding subsection, leading to the evaluation of non-linear effective elastic moduli of the triangular HMS beam network under combined mechanical and magnetic loads. Large deformation kinematics of the triangular HMS unit cell and the beam-level forces developed under different combinations of mechanical stress and magnetic field are described first in the following subsection. With the identified kinematic and kinetic conditions, the beam-level non-linear multi-physical mechanics problems are solved through the semi-analytical HMS beam model as presented in Sections 2.1 and 2.2. Using the beam-level deformation results, computations of the non-linear effective elastic moduli of the triangular HMS beam network under the combined mechanical stress and magnetic field are presented subsequently.

2.4.1. Beam-level forces and deformation kinematics

Under the combined mechanical and magnetic loads as presented in Fig. 4(a), (b), and (d), the HMS beam members undergo bending in combination with axial deformation. Kinematics and kinetics of the beam members under the magnetic field B^a in combination with the three different modes of the mechanical stress σ_1, σ_2, and τ are presented in the following three subsections.

2.4.1.1. Mechanical normal stress along direction-1 and magnetic field along direction-2. Under the combined loading of far-field normal stress σ_1 and magnetic field B^a as shown in Fig. 4(a), all the three members (OA, OB, and AB) of the triangular HMS unit cell undergo combined bending–stretching deformation with one end fixed, while the other ends being restrained to rotation and transverse displacement but free to axial translation. The deformed configuration of the triangular HMS unit cell under the combined loading of σ_1 and B^a is shown in Fig. 4(c). The generalized figure also represents the deformed configuration under the combined loading of σ_2 and B^a. Note in the figure that the changes in the span of the HMS beam members are shown in a generalized manner without taking into consideration of the proper algebraic signs. Those senses of the axial deformations will be implicitly taken care of by the generic beam model under the proper description of the sense of the beam-level forces under a particular combined loading condition.

Due to the symmetry of the deformation under the combined loading of σ_1 and B^a, we concentrate on one inclined member OB in addition to the horizontal member OA. To use the developed framework of hexagonal HMS beam network as presented in the preceding

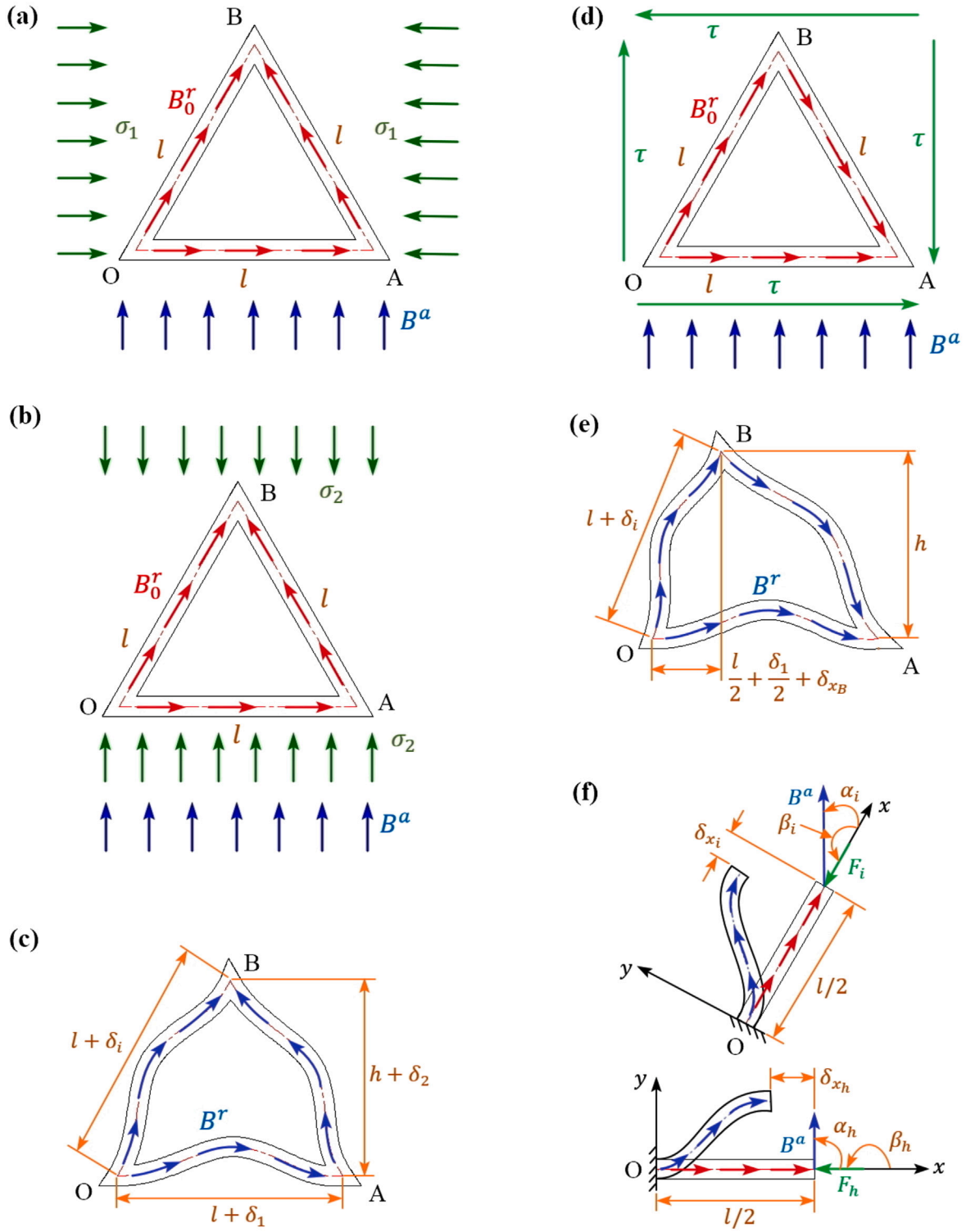

Fig. 4. Multi-physical mechanics of periodic triangular HMS beam network under combined mechanical stress and magnetic field. **(a)** Combined loading mode of the triangular HMS unit cell under normal stress along direction-1 (σ_1) and magnetic field along direction-2 (B^a). **(b)** Combined loading mode of the triangular HMS unit cell under normal stress along direction-2 (σ_2) and magnetic field along direction-2 (B^a). **(c)** Deformed configuration of the triangular HMS unit cell under combined normal stress σ_1 or σ_2 and magnetic field B^a. **(d)** Combined loading mode of the triangular HMS unit cell under shear stress in plane 1–2 (τ) and magnetic field along direction-2 (B^a). **(e)** Deformed configuration of the triangular HMS unit cell under combined shear stress τ and magnetic field B^a. **(f)** Generalized forces and large deformation kinematics of inclined and horizontal members under any of the three combined loading conditions.

subsection readily for the present multi-physical mechanics of triangular HMS beam network, we consider half of the members OA and OB of length $l/2$ which have similar boundary conditions as those of the members of the hexagonal network, i.e., one end fixed with the other end being rotationally restrained but free to translation (refer to Section 2.1.1). Point O is considered the fixed point and origin of local

Cartesian frames (x, y) for half of the inclined and horizontal members. Large deformation kinematics along with the developed forces in half of the inclined and horizontal HMS members under the combined loading of σ_1 and B^a are shown in Fig. 4(f). Note that the kinematic and kinetic descriptions of the HMS half beams in Fig. 4(f) are a generalized representation under any of the three combined loading conditions presented in Fig. 4(a), (b), and (d).

Under the remote mechanical stress σ_1, the tip-concentrated force F_h developed in the horizontal member as shown in Fig. 4(f) is given by

$$F_h = \frac{\sqrt{3}}{2}\sigma_1 bl \tag{61}$$

Inclination angles β_h and α_h of the above-presented mechanical force F_h and the vertical magnetic field B^a for the horizontal HMS member (refer to Fig. 4(f)) are given by

$$\beta_h = \pi \tag{62a}$$

$$\alpha_h = \frac{\pi}{2} \tag{62b}$$

For the inclined HMS member as shown in Fig. 4(f), the developed force F_i and the inclination angle α_i of the magnetic field B^a are given by

$$F_i = 0 \tag{63}$$

$$\alpha_i = \frac{\pi}{6} \tag{64}$$

2.4.1.2. Normal stress along direction-2 and magnetic field along direction-2. Under the remote normal stress σ_2 in combination with the external magnetic field B^a as shown in Fig. 4(b), the large deformation kinematics of the triangular HMS unit cell and the kinetics of the HMS beam members are already described through Fig. 4(c) and (f). The concentrated force F_h developed in the horizontal HMS beam due to the remote stress σ_2 is given by

$$F_h = \frac{1}{2\sqrt{3}}\sigma_2 bl \tag{65}$$

As observed in Fig. 4(f), the inclination angles β_h and α_h are given by

$$\beta_h = 0 \tag{66a}$$

$$\alpha_h = \frac{\pi}{2} \tag{66b}$$

The concentrated force F_i developed in the inclined member is expressed in terms of the remote normal stress σ_2 (refer to Fig. 4(f)) as

$$F_i = \frac{1}{\sqrt{3}}\sigma_2 bl \tag{67}$$

The inclination angles β_i and α_i of the mechanical and magnetic loads for the inclined member as shown in Fig. 4(f) are presented below.

$$\beta_i = \pi \tag{68a}$$

$$\alpha_i = \frac{\pi}{6} \tag{68b}$$

2.4.1.3. Far-field shear stress in 1–2 plane and magnetic field along direction-2. When the triangular HMS beam network is subjected to in-plane shear stress τ combined with the external magnetic field B^a as shown in Fig. 4(d), all the three members (OA, OB, and AB) of the triangular HMS unit cell are subjected to the same boundary conditions as those under the combined normal stress (σ_1 or σ_2) and the magnetic field (B^a) (refer to Fig. 4(c)). However, under the combined load of τ and B^a, the two inclined members OB and AB undergo the opposite modes of axial deformation (compression and tension), and hence the triangular HMS unit cell becomes asymmetric as shown in Fig. 4(e). The opposite distribution of the residual magnetic flux density B_0^r in the inclined members OB and AB makes the structural behaviour under the mechanical and magnetic field in phase with each other (i.e. structurally symmetric, as discussed in the derivation of hexagonal lattices). Within the unit cell-based approach to compute the effective shear modulus, we concentrate only on one inclined member OB in addition to the horizontal member OA. The large deformation kinematics and force kinetics of half of the inclined and horizontal HMS beams are presented through the generalized schematic in Fig. 4(f).

Under the remote shear stress τ, the concentrated axial force F_h developed in the horizontal member along with the inclination angle α_h of the magnetic field (refer to Fig. 4(f)) are expressed as

$$F_h = 0 \tag{69}$$

$$\alpha_h = \frac{\pi}{2} \tag{70}$$

The concentrated force F_i developed in the inclined HMS member as shown in Fig. 4(f) is expressed in terms of the remote shear stress τ as

$$F_i = \tau bl \tag{71}$$

The inclination angles β_i and α_i of the mechanical force F_i and the magnetic field B^a for the inclined HMS beam (refer to Fig. 4(f)) are given below.

$$\beta_i = \pi \tag{72a}$$

$$\alpha_i = \frac{\pi}{6} \tag{72b}$$

2.4.2. Effective elastic moduli

To estimate the non-linear effective elastic moduli of the triangular HMS beam network, geometrically non-linear axial tip-deflections δ_{x_h} and δ_{x_i} of the horizontal and inclined HMS beams under the concentrated force F_h and F_i combined with the magnetic field B^a as described through Fig. 4(f) in the previous subsection are computed based on the generalized HMS beam model. In the framework of the generalized HMS beam model, the geometries of the horizontal and inclined HMS half beams shown in Fig. 4(f) are normalized as

$$\Pi_{0_h} = \Pi_{0_i} = \frac{3}{\left(\frac{t}{l}\right)^2} \tag{73}$$

The non-dimensional forms of the beam-level forces in the framework of the generalized HMS beam model are presented in the respective subsection estimating the elastic moduli of the triangular HMS beam network under a particular combined loading case. Expression of the relative density and non-dimensional forms of the effective elastic moduli are presented subsequently.

2.4.2.1. Computation of E_1 and ν_{12} under combined load σ_1 and B^a. Under the combined loading of normal stress σ_1 and magnetic field B^a (refer to Fig. 4(a) and (f)), the non-dimensional mechanical forces C_h and C_i for the horizontal and inclined members are derived from Eqs. (61) and (63) following the normalization scheme discussed earlier as

$$C_h = \frac{3\sqrt{3}}{2E_s\left(\frac{t}{l}\right)^3}\sigma_1 \tag{74a}$$

$$C_i = 0 \tag{74b}$$

With the non-dimensional mechanical forces C_h and C_i, the non-dimensional magnetic loads B_h and B_i for the horizontal and inclined HMS beams are defined in terms of the magnetic load ratio r_h as

$$B_h = B_i = r_h C_h \tag{75}$$

Under the non-dimensional mechanical and magnetic loads with the inclination angles presented in Eqs. (62) and (64), the non-linear non-dimensional tip-deflections $\bar{\delta}_{x_h}$ and $\bar{\delta}_{x_i}$ of the horizontal and inclined HMS beams are computed. The normal strain in direction-1 (ϵ_1) is

obtained in terms of the beam-level defection $\bar{\delta}_{x_h}$ through a suitable coordinate transformation as given by

$$\epsilon_1 = \bar{\delta}_{x_h} \tag{76}$$

The normal strain in direction-2 (ϵ_2) is derived from the deformed geometry of the triangular HMS unit cell as presented in Fig. 4(c). By using the Pythagorean theorem on the triangle, we get

$$(h+\delta_2)^2 + \left(\frac{l+\delta_1}{2}\right)^2 = (l+\delta_i)^2 \tag{77}$$

Noting the geometric relation of the undeformed triangular unit cell as $h^2 + (l/2)^2 = l^2$ (refer to Fig. 4(a)) and neglecting the higher order terms, the above equation gives

$$\sqrt{3}\,\delta_2 = -\frac{1}{2}\,\delta_1 + 2\,\delta_i \tag{78}$$

From the above relation, the strain ϵ_2 is obtained in terms of the beam-level displacements as

$$\epsilon_2 = -\frac{1}{3}\,\bar{\delta}_{x_h} + \frac{4}{3}\,\bar{\delta}_{x_i} \tag{79}$$

With the known normal strains ϵ_1 and ϵ_2 as presented in Eqs. (76) and (79), the non-linear effective elastic moduli E_1 and ν_{12} are obtained as

$$E_1 = \frac{\sigma_1}{\bar{\delta}_{x_h}} \tag{80}$$

$$\nu_{12} = \frac{1}{3} - \frac{4}{3}\,\frac{\bar{\delta}_{x_i}}{\bar{\delta}_{x_h}} \tag{81}$$

2.4.2.2. Computation of E_2 and ν_{21} under combined load σ_2 and B^a. Under the normal stress σ_2 combined with B^a as shown in Fig. 4(b) and (f), the non-dimensional forces C_h and C_i for the horizontal and inclined beams are obtained from Eqs. (65) and (67) as

$$C_h = \frac{\sqrt{3}}{2E_s\left(\frac{t}{l}\right)^3}\,\sigma_2 \tag{82a}$$

$$C_i = \frac{\sqrt{3}}{E_s\left(\frac{t}{l}\right)^3}\,\sigma_2 \tag{82b}$$

In combination with the above-presented non-dimensional mechanical forces C_h and C_i, the HMS beams are subjected to the non-dimensional magnetic loads B_h and B_i which are defined in terms of the magnetic load ratio r_i by

$$B_h = B_i = r_i C_i \tag{83}$$

The inclination angles of the mechanical and magnetic loads are already presented in Eqs. (66) and (68). Following the same procedure as in the previous combined loading case in the preceding subsection, the non-linear non-dimensional tip-deflections $\bar{\delta}_{x_h}$ and $\bar{\delta}_{x_i}$ are obtained which give the normal strains ϵ_1 and ϵ_2 having the same mathematical expressions as presented in Eqs. (76) and (79). Using the strain expressions, the non-linear effective Young's modulus E_2 and the Poisson's ratio ν_{21} of the triangular HMS beam network are derived as

$$E_2 = \frac{3\,\sigma_2}{-\bar{\delta}_{x_h} + 4\,\bar{\delta}_{x_i}} \tag{84}$$

$$\nu_{21} = \frac{3\,\bar{\delta}_{x_h}}{\bar{\delta}_{x_h} - 4\,\bar{\delta}_{x_i}} \tag{85}$$

2.4.2.3. Computation of G_{12} under combined load τ and B^a. Under the combined in-plane shear stress τ and magnetic field B^a as presented in Fig. 4(d) and (f), the non-dimensional mechanical forces C_h and C_i for the horizontal and inclined HMS beam members as derived from Eqs. (69) and (71) are given by

$$C_h = 0 \tag{86a}$$

$$C_i = \frac{3}{E_s\left(\frac{t}{l}\right)^3}\,\tau \tag{86b}$$

The non-dimensional magnetic loads B_h and B_i of the horizontal and inclined HMS beam members are defined similarly as those for the other two combined loading cases as

$$B_h = B_i = r_i C_i \tag{87}$$

Under the non-dimensional mechanical and magnetic forces with the inclination angles of Eqs. (70) and (72), the non-linear non-dimensional defections $\bar{\delta}_{x_h}$ and $\bar{\delta}_{x_i}$ are computed through the generalized HMS beam model. To derive the in-plane shear strain γ_{12} under the combined loading of τ and B^a, we concentrate on the deformed triangular HMS unit cell as presented in Fig. 4(e). By using the Pythagorean theorem on the deformed triangle, we get the following geometric relation

$$h^2 + \left(\frac{l}{2} + \frac{\delta_1}{2} + \delta_{x_B}\right)^2 = (l+\delta_i)^2 \tag{88}$$

Noting the geometric relation of the undeformed triangular unit cell as $h^2 + (l/2)^2 = l^2$ (refer to Fig. 4(d)) and carrying out some mathematical manipulations by neglecting the higher order terms, the horizontal displacement δ_{x_B} of point B is obtained as

$$\delta_{x_B} = 2\,\delta_i - \frac{\delta_1}{2} \tag{89}$$

Due to the horizontal displacement δ_{x_B}, the shear strain γ_{12} developed in the triangular unit cell is given by $\gamma_{12} = \delta_{x_B}/h$. Using the geometric relation from Eq. (89), the shear strain γ_{12} is expressed in terms of the beam-level displacements $\bar{\delta}_{x_h}$ and $\bar{\delta}_{x_i}$ as

$$\gamma_{12} = \frac{4}{\sqrt{3}}\,\bar{\delta}_{x_i} - \frac{1}{\sqrt{3}}\,\bar{\delta}_{x_h} \tag{90}$$

Once the shear strain γ_{12} is known as presented above, the non-linear effective shear modulus G_{12} of the triangular HMS beam network is obtained through its fundamental definition $G_{12} = \tau/\gamma_{12}$ as

$$G_{12} = \frac{\sqrt{3}\,\tau}{4\,\bar{\delta}_{x_i} - \bar{\delta}_{x_h}} \tag{91}$$

2.4.2.4. Non-dimensional elastic moduli. As Poisson's ratios ν_{12} and ν_{21} are already non-dimensional, they are presented in their original forms. The other three effective elastic moduli E_1, E_2, and G_{12} of the triangular HMS beam network are presented in non-dimensional forms following the normalization scheme as

$$\bar{E}_1 = \frac{E_1}{E_s\rho^3},\ \bar{E}_2 = \frac{E_2}{E_s\rho^3},\ \bar{G}_{12} = \frac{G_{12}}{E_s\rho^3} \tag{92}$$

Here the relative density ρ of the triangular HMS beam network obtained following the same definition as the hexagonal beam network is given by

$$\rho = 2\sqrt{3}\,\frac{t}{l} \tag{93}$$

2.5. Effective elastic moduli of rectangular HMS beam networks

To estimate the non-linear effective elastic moduli E_1, ν_{12}, E_2, ν_{21}, and G_{12} of periodic rectangular network of HMS beams, as shown in Fig. 1(g)V, the unit cell consisting of horizontal HMS beam of length l and vertical HMS beam of length h with residual magnetic flux density B_0^r is chosen. The three different combined mechanical and magnetic loading conditions for the rectangular HMS unit cell are shown in Fig. 5(a), (b), and (d) respectively.

Under the normal modes of mechanical stress σ_1 or σ_2 in absence of magnetic field B^a, the cell members of the rectangular lattice undergo stretch-dominated deformations (Gibson and Ashby, 1999). Whereas, under the shear mode of mechanical stress τ in absence of magnetic field B^a, the cell members are subjected to bending-dominated deformations (Wang and McDowell, 2004). The analytical formulae for the

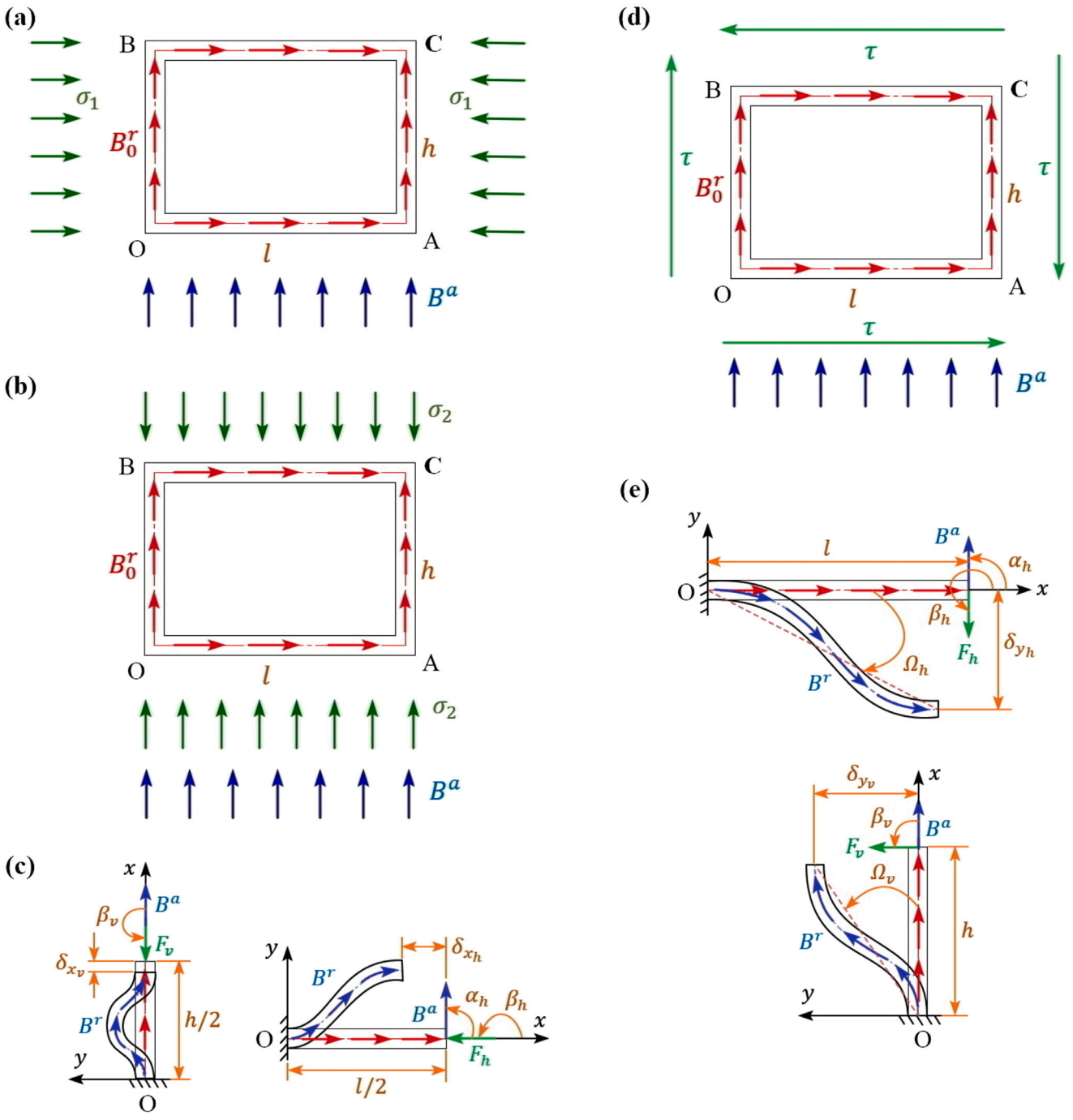

Fig. 5. Multi-physical mechanics of periodic rectangular HMS beam network under combined mechanical stress and magnetic field. (a) Combined loading mode of the rectangular HMS unit cell under normal stress along direction-1 (σ_1) and magnetic field along direction-2 (B^a). **(b)** Combined loading mode of the rectangular HMS unit cell under normal stress along direction-2 (σ_2) and magnetic field along direction-2 (B^a). **(c)** Generalized forces and large deformation kinematics of the vertical and horizontal members under combined normal stress σ_1 or σ_2 and magnetic field B^a. **(d)** Combined loading mode of the rectangular HMS unit cell under shear stress in plane 1–2 (τ) and magnetic field along direction-2 (B^a). **(e)** Forces and large deformation kinematics of the horizontal and vertical members under combined shear stress τ and magnetic field B^a.

effective elastic moduli of rectangular lattice under mechanical load only within small deformation regime are given by (Gibson and Ashby, 1999; Wang and McDowell, 2004)

$$\frac{E_1}{E_s} = \frac{\left(\frac{t}{l}\right)}{\left(\frac{h}{l}\right)} \tag{94a}$$

$$\frac{E_2}{E_s} = \frac{t}{l} \tag{94b}$$

$$\nu_{12} = \nu_{21} = 0 \tag{94c}$$

$$\frac{G_{12}}{E_s} = \frac{\left(\frac{t}{l}\right)^3}{\frac{h}{l}\left(1+\frac{h}{l}\right)} \tag{94d}$$

In this subsection, the conventional unit cell-based approach for rectangular lattices (Gibson and Ashby, 1999; Wang and McDowell, 2004) is extended to a magneto-active multi-physical mechanics-based semi-analytical framework following the formulation for hexagonal

HMS beam network presented in the preceding subsection, leading to the evaluation of non-linear effective elastic moduli of the rectangular HMS beam network under combined mechanical and magnetic loads. Large deformation kinematics of the rectangular HMS unit cell and the beam-level forces developed under different combinations of mechanical stress and magnetic field are described first in the following subsection. With the identified kinematic and kinetic conditions, the beam-level non-linear multi-physical mechanics problems are solved through the semi-analytical HMS beam model as presented in Sections 2.1 and 2.2. Using the beam-level deformation results, computations of the non-linear effective elastic moduli of the rectangular HMS beam network under the combined mechanical stress and magnetic field are presented subsequently.

2.5.1. Beam-level forces and deformation kinematics

Under the three combined mechanical and magnetic loading conditions as presented in Fig. 5(a), (b), and (d), the HMS beam members undergo large deformation, the kinematics and kinetics of which are described in the following three subsections.

2.5.1.1. Far-field normal stress along direction-1 and magnetic field along direction-2. Under the combined loading case of normal stress σ_1 and magnetic field B^a as shown in Fig. 5(a), the horizontal and vertical HMS beam members OA and OB of the rectangular HMS unit cell undergo combined bending–stretching deformation with fixed end O and the other ends A and B being restrained to rotation and transverse displacement but free to axial translation. The other pairs of horizontal and vertical HMS beams BC and CA are not considered in the analysis due to the structural symmetry of the unit cell. Following the same procedure as in the case of the triangular HMS beam network (refer to the preceding subsection), half of the members OA and OB of length $l/2$ and $h/2$ respectively are considered for the present multi-physical mechanics. The half beams are subjected to the boundary conditions of one fixed end with the other end being rotationally restrained but free to translation.

Large deformation kinematics and the force kinetics of the vertical and horizontal HMS half beams under the combined loading of σ_1 and B^a are presented in Fig. 5(c) concerning the local Cartesian frames (x, y) fitted at the fixed point O. Note that the kinematic and kinetic descriptions of the HMS half beams in Fig. 5(c) are a generalized representation under the normal modes of mechanical stress σ_1 or σ_2 combined with the magnetic field B^a as presented in Fig. 5(a) and (b).

The concentrated mechanical force F_h developed in the horizontal HMS beam under the remote normal stress σ_1 as shown in Fig. 5(c) is given by

$$F_h = \sigma_1 bh \tag{95}$$

Inclination angles β_h and α_h of the mechanical force F_h and the magnetic field B^a respectively for the horizontal HMS member as shown in Fig. 5(c) are given by

$$\beta_h = \pi \tag{96a}$$

$$\alpha_h = \frac{\pi}{2} \tag{96b}$$

The vertical HMS beam (refer to Fig. 5(c)) is only subjected to the magnetic field B^a without any mechanical force F_v under the present combined loading case. Hence, the kinetics of the vertical HMS beam is represented as

$$F_v = 0 \tag{97}$$

$$\alpha_v = 0 \tag{98}$$

2.5.1.2. Far-field normal stress along direction-2 and magnetic field along direction-2. The large deformation kinematics and kinetics of the members of the rectangular HMS unit cell under the combined loading of σ_2 and B^a are already described through the generalized schematic diagrams in Fig. 5(c). Under the present combined loading case, the horizontal HMS beams are not subjected to any mechanical force F_h. However, the horizontal members are subjected to B^a with the inclination angle α_h. The kinetic relations for the horizontal HMS beam member are summarized as

$$F_h = 0 \tag{99}$$

$$\alpha_h = \frac{\pi}{2} \tag{100}$$

The concentrated force F_v developed in the vertical member (refer to Fig. 5(c)) is given by

$$F_v = \sigma_2 bl \tag{101}$$

The inclination angles β_v and α_v of the mechanical and magnetic loads respectively for the vertical member as presented in Fig. 5(c) are given by

$$\beta_v = \pi \tag{102a}$$

$$\alpha_v = 0 \tag{102b}$$

2.5.1.3. Shear stress in 1–2 plane and magnetic field along direction-2. Under the combined loading of in-plane shear stress τ and magnetic field B^a as shown in Fig. 5(d), the horizontal and vertical members OA and OB of the rectangular HMS unit cell undergo bending-dominated large deformation with fixed end O and the other ends A and B being rotationally restrained but free to translation. Within the present multi-physical mechanics-based framework, the large deformation kinematics and kinetics of the horizontal and vertical HMS full beam members OA and OB are analysed as presented in Fig. 5(e).

The tip-concentrated transverse force F_h developed in the horizontal HMS beam under the remote shear stress τ is expressed as

$$F_h = \tau bh \tag{103}$$

The inclination angles β_h and α_h of the mechanical and magnetic loads for the horizontal HMS beam as shown in Fig. 5(e) are given by

$$\beta_h = \frac{3\pi}{2} \tag{104a}$$

$$\alpha_h = \frac{\pi}{2} \tag{104b}$$

The concentrated force F_v developed in the vertical HMS beam member under the remote shear stress τ (refer to Fig. 5(e)) is expressed by

$$F_v = \tau bl \tag{105}$$

The inclination angles β_v and α_v of the mechanical force F_v and the magnetic field B^a for the vertical HMS beam as shown in Fig. 5(e) are summarized as

$$\beta_v = \frac{\pi}{2} \tag{106a}$$

$$\alpha_v = 0 \tag{106b}$$

2.5.2. Effective elastic moduli

To estimate the non-linear effective elastic moduli E_1, ν_{12}, E_2, and ν_{21} of the rectangular HMS beam network under the normal modes of mechanical stress σ_1 or σ_2 in combination with the magnetic field B^a, geometrically non-linear axial tip-deflections δ_{x_h} and δ_{x_v} of the horizontal and vertical HMS half beams under the concentrated force F_h and F_v combined with the magnetic field B^a as described through Fig. 5(c) in the previous subsection are computed through the generalized HMS beam model. Whereas, for the estimation of the non-linear effective shear modulus G_{12} under in-plane shear stress τ and the magnetic

field B^a, geometrically non-linear transverse deflections δ_{y_h} and δ_{y_v} of the horizontal and vertical HMS full beams as shown in Fig. 5(e) are computed.

In the framework of the generalized HMS beam model, the geometries of the horizontal and vertical HMS half beams considered for combined loading case under normal stress σ_1 or σ_2 and magnetic field B^a as shown in Fig. 5(c) are normalized as

$$\Pi_{0_h} = \frac{3}{\left(\frac{t}{l}\right)^2} \tag{107a}$$

$$\Pi_{0_v} = \frac{3\left(\frac{h}{l}\right)^2}{\left(\frac{t}{l}\right)^2} \tag{107b}$$

Whereas, the non-dimensional geometries of the HMS full beams considered for the combined loading case under shear stress τ and magnetic field B^a as shown in Fig. 5(e) are given by

$$\Pi_{0_h} = \frac{12}{\left(\frac{t}{l}\right)^2} \tag{108a}$$

$$\Pi_{0_v} = \frac{12\left(\frac{h}{l}\right)^2}{\left(\frac{t}{l}\right)^2} \tag{108b}$$

2.5.2.1. Computation of E_1 and ν_{12} under combined load σ_1 and B^a. The non-dimensional mechanical forces C_h and C_v for the horizontal and vertical HMS beams under the combined loading of normal stress σ_1 and magnetic field B^a as shown in Fig. 5(a) and (c) are obtained from Eqs. (95) and (97) as

$$C_h = \frac{3\left(\frac{h}{l}\right)}{E_s\left(\frac{t}{l}\right)^3}\sigma_1 \tag{109a}$$

$$C_v = 0 \tag{109b}$$

Magnitudes of the non-dimensional magnetic loads B_h and B_v for the horizontal and vertical HMS beam members of the rectangular HMS unit cell are defined in terms of the magnetic load ratio r_h and the non-dimensional mechanical force C_h as

$$B_h = r_h C_h \tag{110a}$$

$$B_v = \left(\frac{h}{l}\right)^2 r_h C_h \tag{110b}$$

Under the prescribed non-dimensional mechanical and magnetic loads with the inclination angles as presented in Eqs. (96) and (98), the non-linear axial deflections are computed in non-dimensional forms $\bar{\delta}_{x_h}$ and $\bar{\delta}_{x_v}$. In terms of the beam-level deflections, the normal strains in direction-1 (ϵ_1) and direction-2 (ϵ_2) are defined by

$$\epsilon_1 = \bar{\delta}_{x_h} \tag{111}$$

$$\epsilon_2 = \bar{\delta}_{x_v} \tag{112}$$

With the above-presented strains ϵ_1 and ϵ_2, the non-linear effective Young's modulus E_1 and Poisson's ratio ν_{12} of the rectangular HMS beam network are obtained readily as

$$E_1 = \frac{\sigma_1}{\bar{\delta}_{x_h}} \tag{113}$$

$$\nu_{12} = -\frac{\bar{\delta}_{x_v}}{\bar{\delta}_{x_h}} \tag{114}$$

2.5.2.2. Computation of E_2 and ν_{21} under combined load σ_2 and B^a. When the rectangular HMS beam network is subjected to combined loading under the normal stress σ_2 and the magnetic field B^a as shown in Fig. 5(b), the concentrated forces in the horizontal and vertical HMS beams are expressed in non-dimensional forms using Eqs. (99) and (101) as

$$C_h = 0 \tag{115a}$$

$$C_v = \frac{3\left(\frac{h}{l}\right)^2}{E_s\left(\frac{t}{l}\right)^3}\sigma_2 \tag{115b}$$

Magnitudes of the non-dimensional magnetic loads B_h and B_v are defined in terms of load ratio r_v and non-dimensional load C_v in a similar way as in the case of the other previously discussed combined loading mode as

$$B_h = \frac{r_v C_v}{\left(\frac{h}{l}\right)^2} \tag{116a}$$

$$B_v = r_v C_v \tag{116b}$$

Under the above-presented mechanical and magnetic loads with the inclination angles presented in Eqs. (100) and (102), the non-linear beam-level deflections $\bar{\delta}_{x_h}$ and $\bar{\delta}_{x_v}$ are computed which in turn give the normal strains ϵ_1 and ϵ_2 through Eqs. (111) and (112). Using the strain expressions, the non-linear effective elastic moduli E_2 and ν_{21} of the rectangular HMS beam network under the combined loading of σ_2 and B^a are obtained as

$$E_2 = \frac{\sigma_2}{\bar{\delta}_{x_v}} \tag{117}$$

$$\nu_{21} = -\frac{\bar{\delta}_{x_h}}{\bar{\delta}_{x_v}} \tag{118}$$

2.5.2.3. Computation of G_{12} under combined load τ and B^a. Under the combined loading of τ and B^a as shown in Fig. 5(d) and (e), the non-dimensional forces C_h and C_v for the horizontal and vertical beams are derived from Eqs. (103) and (105) as

$$C_h = \frac{12\left(\frac{h}{l}\right)}{E_s\left(\frac{t}{l}\right)^3}\tau \tag{119a}$$

$$C_v = \frac{12\left(\frac{h}{l}\right)^2}{E_s\left(\frac{t}{l}\right)^3}\tau \tag{119b}$$

The non-dimensional magnetic loads B_h and B_v for the horizontal and vertical HMS beam members are defined as

$$B_h = r_h C_h \tag{120a}$$

$$B_v = \left(\frac{h}{l}\right)^2 r_h C_h \tag{120b}$$

Under the above-presented non-dimensional mechanical and magnetic loads with the inclination angles presented in Eqs. (104) and (106), non-linear transverse defections of the beam tips are computed in non-dimensional forms as denoted by $\bar{\delta}_{y_h}$ and $\bar{\delta}_{y_v}$ in Fig. 5(e). In terms of the transverse tip-deflections, rotations of the horizontal and vertical HMS beams are obtained as

$$\Omega_h = -\bar{\delta}_{y_h} \tag{121a}$$

$$\Omega_v = \bar{\delta}_{y_v} \tag{121b}$$

Due to the above-presented rotations Ω_h and Ω_v of the horizontal and vertical HMS beam members respectively, the total shear strain γ_{12} developed in the rectangular unit cell is given by

$$\gamma_{12} = -\bar{\delta}_{y_h} + \bar{\delta}_{y_v} \tag{122}$$

The non-linear effective shear modulus G_{12} of the rectangular HMS beam network is obtained subsequently through the fundamental definition $G_{12} = \tau/\gamma_{12}$ using Eq. (122) as

$$G_{12} = \frac{\tau}{-\bar{\delta}_{y_h} + \bar{\delta}_{y_v}} \tag{123}$$

2.5.2.4. Non-dimensional elastic moduli. As Poisson's ratios ν_{12} and ν_{21} are already non-dimensional, they are presented in their original forms. Following a similar representation framework as the other periodic network configurations, the effective elastic moduli E_1, E_2, and G_{12} of the rectangular HMS beam network are normalized as

$$\bar{E}_1 = \frac{E_1}{E_s\rho^3},\ \bar{E}_2 = \frac{E_2}{E_s\rho^3},\ \bar{G}_{12} = \frac{G_{12}}{E_s\rho^3} \tag{124}$$

Here the relative density ρ of the rectangular HMS beam network is derived as

$$\rho = \frac{t}{l}\frac{\left(1+\frac{h}{l}\right)}{\frac{h}{l}} \tag{125}$$

Having established the semi-analytical large-deformation computational frameworks for different magneto-active periodic beam networks, we present numerical results in the following section to demonstrate active broadband elasticity programming as a function of the externally applied magnetic field and bi-level (unit cell geometry and beam-level spatially-varying residual magnetic flux direction) metamaterial architectures.

3. Results and discussion

The generalized HMS beam model is the backbone of the present semi-analytical framework to estimate the non-linear effective elastic moduli of hexagonal HMS beam networks under combined mechanical and magnetic loads. Hence, before going to investigate the effective elastic moduli of HMS beam networks, the HMS beam model is validated first, as presented in the first subsection here. Thereafter, critical numerical beam-level results are furnished with symmetric and asymmetric residual magnetic flux density under different combinations of mechanical and magnetic loads. Note that modulation capability of the shapes of such architected beams will constitute the foundation for bi-level design of lattices, as discussed later in this section. Applicability of the full-beam and half-beam model for symmetric and asymmetric residual magnetic flux density of HMS beam is also investigated along with the influence of centreline extensibility on the load–deformation characteristics of HMS beam.

Following the beam-level results, the geometrically non-linear semi-analytical framework estimating the effective elastic moduli of the HMS beam networks is validated, as presented in the third subsection. Validations of the present framework at the beam-level as well as at the beam network-level would provide adequate confidence in the proposed computational models. Subsequently, the effect of magnetic field in combination with the different modes of mechanical load on the non-linear effective elastic moduli of hexagonal HMS beam network with uniform residual magnetic flux density is investigated, as presented in the fourth subsection. Based on the kinematic and kinetic conditions of the beam elements of the hexagonal HMS beam network, two intuitive designs of residual magnetic flux density $S(\xi)$ (beam-level architecture) are proposed in the fifth subsection which would significantly influence the effective elastic moduli of the HMS beam network under combined mechanical and magnetic loads. In the following subsection, we demonstrate the applicability of the concept of active broad-band elasticity modulation for different other forms of lattice geometries, as presented in Fig. 1(g).

For all the computations at beam-level and beam network-level, the material constitutive parameters in the framework of the Yeoh hyperelastic model are considered as $C_{10} = 0.2712$, $C_{20} = 0.0305$, and $C_{30} = -0.004$ (Xu and Liu, 2018). The numerical value of the computational parameter λ and the limit of μ are considered as 0.9 and 0.05% respectively. The number of functions for the centreline rotation φ and centreline strain ε are selected as $nb = ns = 5$, based on a convergence study.

3.1. Beam-level validation

Though large deformation analysis of HMS beam structures has become a topic of interest for the last few years, the studies focus on structural characteristics separately under mechanical load only and magnetic actuation only. Hence, comparable results for our multi-physical mechanics-based beam model for coupled mechanical and magnetic loading conditions are not readily available in the literature. Thus, the current geometrically non-linear HMS beam model is first validated under mechanical load only by comparing it with the results presented by Chen and Wang (2021). Whereas, for the loading case of magnetic actuation only, we validate our model with the paper by Chen et al. (2020a). The validation studies for both the mechanical and magnetic loading cases are performed for the non-dimensional geometric specification of the HMS beam $\Pi_0 = 10000$.

The validation study of the generalized HMS beam model under mechanical load only is carried out for the cantilever boundary conditions subjected to tip-concentrated non-dimensional load C with inclination angle β as considered in the paper (Chen and Wang, 2021). The non-dimensional deformed configurations $(\xi,\ \eta)$ of the cantilever beam under different values of C for inclination angle β of $\pi/4$, $\pi/2$, $3\pi/4$, and $9\pi/10$ as obtained from the present model are shown through solid lines in Figure S1(a)–(d) respectively. Whereas, the corresponding deformation results reported in the literature (Chen and Wang, 2021) are also plotted through dotted points in Figure S1. As obvious from Figure S1, an excellent agreement between the present semi-analytical HMS beam model and the model presented in literature (Chen and Wang, 2021) is found for all the considered load magnitudes C and the orientation angles β. Hence, the comparison studies in Figure S1 clearly show the capability of the present HMS beam model in predicting highly non-linear deformation characteristics of the soft beam under mechanical load only.

The validation study of the present non-linear beam model under magnetic load only is carried out for four different deformed shapes obtained under different designs of residual magnetic flux density $S(\xi)$ of the HMS beam subjected to multiple boundary conditions as considered in literature (Chen et al., 2020a). The first considered case among them is the m-shape deformed configuration which is obtained for the design of $S(\xi)$ as given below with the free-free boundary conditions ($\theta'(0) = 0$ and $\theta'(1) = 0$) and inclination angle $\alpha = \pi/2$ (Chen et al., 2020a).

$$S = \begin{cases} 1, & 0 \le \xi \le 0.25 \text{ or } 0.5 \le \xi \le 0.75 \\ -1, & 0.25 < \xi < 0.5 \text{ or } 0.75 < \xi \le 1.0 \end{cases}$$

With the above-presented residual magnetic flux density $S(\xi)$, the prescribed boundary conditions and inclination angle, the m-shape deformed configurations of HMS beam under non-dimensional magnetic actuations $B = 30$, $B = 100$, and $B = 300$ are obtained from the present non-linear model as shown through solid lines in Figure S2(a)–(c) respectively. The corresponding deformed shapes as reported in literature (Chen et al., 2020a) are also shown in the plots through dotted points.

The second shape we concentrate on is the s-shape configuration which is obtained under the same boundary conditions and inclination angle α as in the case of m-shape configurations but with the following design of $S(\xi)$ (Chen et al., 2020a)

$$S = \begin{cases} 1, & 0 \le \xi < \frac{1}{3} \text{ or } \frac{2}{3} \le \xi \le 1 \\ -1, & \frac{1}{3} \le \xi < \frac{2}{3} \end{cases}$$

The comparison plots between the present model and the results reported in literature (Chen et al., 2020a) for the s-shape configurations under the non-dimensional magnetic actuation B of 30, 100, and 300 are presented in Figure S2(d)–(f) respectively.

The third type of deformed shape considered for the validation study of the HMS beam model under magnetic actuation only is the n-shape configuration. The n-shape configuration is achieved for the same boundary conditions and inclination angle α as those of the m-shape and s-shape configurations but with the coefficient of residual magnetic flux density (Chen et al., 2020a)

$$S = \begin{cases} 1, & 0 \le \xi < 0.5 \\ -1, & 0.5 \le \xi \le 1 \end{cases}$$

Comparisons of n-shape deformed configurations from the present semi-analytical model with the results reported in literature (Chen et al., 2020a) are shown in Figure S2(g)–(i) for the magnetic actuation $B = 30$, $B = 60$, and $B = 100$ respectively.

The fourth type of the deformed shape of the HMS beam under magnetic actuation we consider is the Ω-shape configuration. The configuration is achieved for the same design of $S(\xi)$ as that for the n-shape configurations but under the boundary conditions of $\theta(0) = 0$ and $\theta(1) = 0$ with the inclination angle of the magnetic field $\alpha = \pi$ (Chen et al., 2020a). The Ω-shape deformed configurations of HMS beam under magnetic actuation B of 60, 100, and 200 are compared with the present non-linear model and the reported results in literature (Chen et al., 2020a) as presented in Figure S2(j)–(l) respectively.

The excellent matching of the deformation results obtained from the present semi-analytical model and literature (Chen et al., 2020a), as shown in Figure S2, validates our non-linear model in predicting complex configurations of HMS beam with designed spatially-varying residual magnetic flux densities under different magnetic actuation.

3.2. Beam-level numerical results under coupled mechanical and magnetic loads

Once the developed geometrically non-linear HMS beam model is validated for separate loading conditions of mechanical load only and magnetic load only, as presented in the previous subsection, benchmark numerical results under coupled mechanical and magnetic loading conditions are presented here. Note that the such coupled effect of magneto-mechanical loading has not been investigated in the literature through the development of a comprehensive computational framework for HMS beams.

An HMS beam representing the generalized element (full or half length) of the HMS beam network having length L with non-dimensional geometric specification $\Pi_0 = 10000$ is considered here. Non-linear deformation characteristics of the HMS beam are simulated through the full-beam and half-beam models within the extensible and inextensible versions of the present semi-analytical framework. The typical boundary conditions (as considered here) of the HMS beam as a full-beam problem and as a half-beam problem have been already described in detail in Section 2.1.

The considered HMS full-beam is fixed at one end with the other end being rotationally restrained but free to translation and subjected to non-dimensional mechanical force $C = 10$ applied incrementally in 50 steps. At each incremental step of C, five non-dimensional magnetic loads $B = rC$ are applied by five magnetic load ratio r of 0.8, 1.6, 2.4, 3.2, and 4 for two different cases of uniform residual magnetic flux density with $S = 1$ and $S = -1$. For the considered HMS full-beam problem, four different inclination angles of the mechanical and magnetic loads are considered as $\alpha = \beta = \pi/2$, $\alpha = \beta = \pi/3$, $\alpha = \beta = \pi/4$, and $\alpha = \beta = \pi/6$. The non-dimensional deformed configurations (ξ, η) of the HMS beam with residual magnetic flux density $S = 1$ and $S = -1$ under the mechanical load $C = 10$ in combination with different magnetic load ratios r are presented in Fig. 6(a)–(d) for the considered four sets of inclination angles respectively. The solid lines in the plots represent the results obtained from the extensible model. Whereas, the results obtained from the inextensible version of the non-linear model are plotted through dotted points in the figure. To observe the effect of magnetic load in combination with the mechanical loading on the non-linear deformation characteristics of the HMS beam with $S = 1$ and $S = -1$, variations of the non-dimensional tip-deflection $\bar{\delta}_y$ with the non-dimensional mechanical load C for the considered different magnetic load ratio r are shown in Figure S3(a)–(d) corresponding to four sets of inclination angles.

Figs. 6 and S3 clearly show that for the residual magnetic flux density with the coefficient $S = 1$, deflection under combined mechanical load C and magnetic field B for all the considered inclination angles β and α increases with magnetic load ratio r compared to the deflection under mechanical load only ($r = 0$). Whereas, for the residual magnetic flux density having coefficient $S = -1$, the deflection decreases with r for the same combination of mechanical and magnetic loads. Hence, it is clear from the results that we can modulate stiffness characteristics of HMS beam as per our requirements by applying a magnetic field in combination with mechanical load through proper design of the residual magnetic flux density $S(\xi)$ of the HMS beam. Such effects are exploited in the current design of lattice metamaterials for broadband elasticity programming.

Now the HMS full-beam of length L is modelled as two HMS half-beams with length $L/2$ subjected to cantilever boundary conditions. To apply the same dimensional force F as that of the full-beam, the maximum value of the non-dimensional force C for the half-beam is taken as 2.5. At each incremental step of mechanical force C, the same five magnetic load ratios r as those for the full-beam problem are considered as 0.8, 1.6, 2.4, 3.2, and 4. The deformed configurations of the HMS half-beam in the non-dimensional plane (ξ, η) under the maximum step of the mechanical load $C = 2.5$ in combination with the considered different magnetic loads are shown in Figure S4(a)–(d). Whereas, the non-linear variations of the non-dimensional tip-deflection $\bar{\delta}_y$ with the non-dimensional mechanical load C for the considered different magnetic load ratio r are presented in Figure S5(a)–(d).

It is evident from Figs. 6–S5 that the effects of the magnetic field in combination with the mechanical load on the deformation characteristics of the HMS half-beam are the same as the HMS full-beam. The overall deflections of the HMS half-beam are exactly half of the deflections for the HMS full-beam under the same condition of combined mechanical and magnetic loads. Hence, it is proved that an HMS full-beam with one fixed end and the other end being rotationally restrained but free to translation can be modelled as an HMS half-beam with cantilever boundary conditions when the HMS beam has symmetric residual magnetic flux density about the mid-point. However, for asymmetric residual magnetic flux density, the applicability of such a modelling concept is investigated in the following paragraphs.

Two different asymmetric distributions of residual magnetic flux density about the mid-point are considered for HMS full-beam by the following $S(\xi)$.

$$S = \begin{cases} 1, & 0 \le \xi < 0.5 \\ -1, & 0.5 \le \xi \le 1 \end{cases}$$

$$S = \begin{cases} -1, & 0 \le \xi < 0.5 \\ 1, & 0.5 \le \xi \le 1 \end{cases}$$

With the above-presented designs of $S(\xi)$ for the same geometric and loading parameters as those for the HMS full-beam with symmetric uniform residual magnetic flux density, load–deformation characteristics of HMS full-beam are computed. Deformed configurations of the HMS full-beam having asymmetric magnetic flux density are presented in Fig. 7. The figure depicts some non-conventional typical complex shapes of HMS beam achieved for the considered designs of $S(\xi)$. Though the curvatures of the deformed configurations are different for the two considered distributions of residual magnetic flux density, the endpoints undergo the same deflections. Variations of such common tip-deflection $\bar{\delta}_y$ with the mechanical load C for the considered different magnetic load ratios r are shown in Figure S6. The figure clearly shows

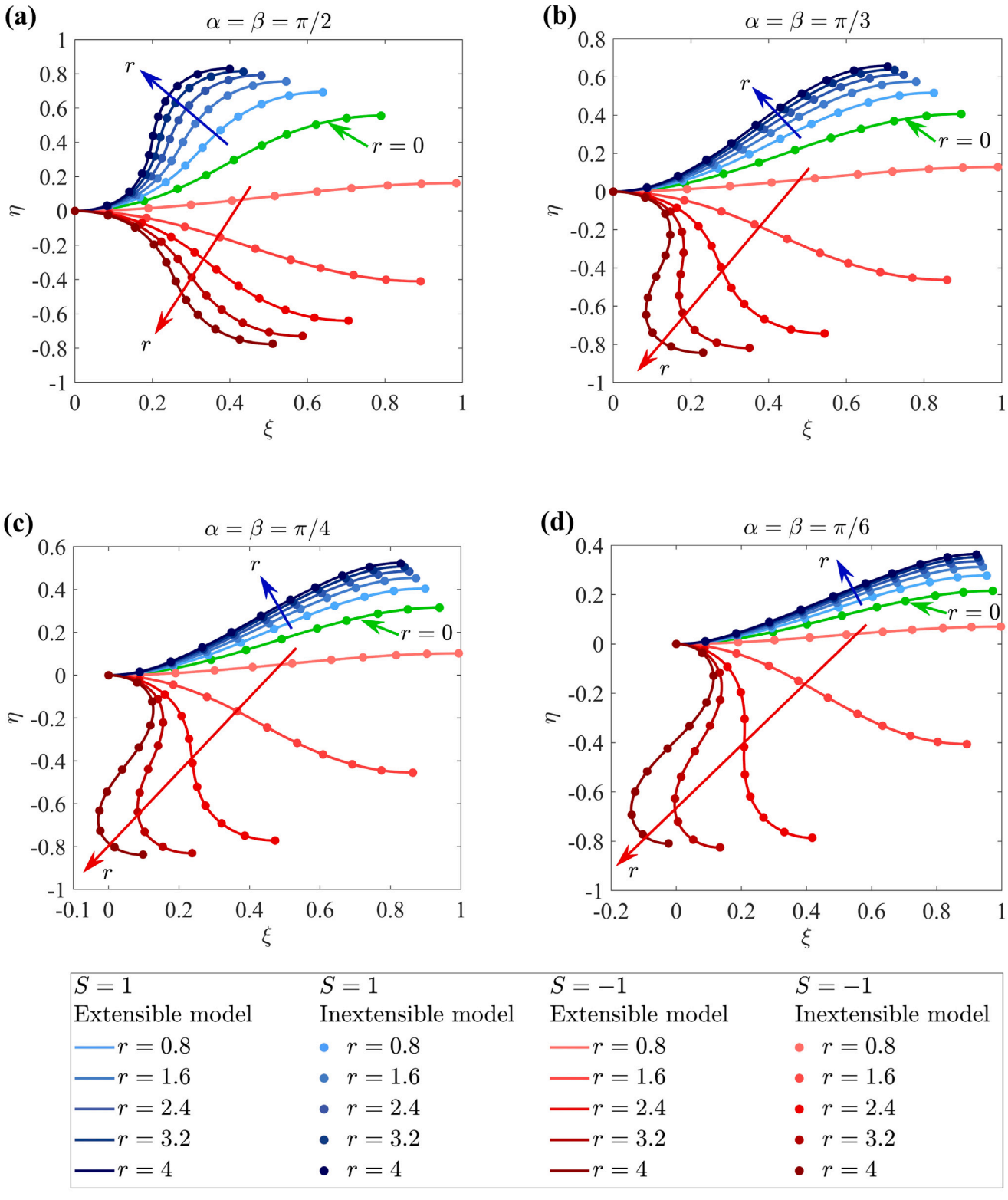

Fig. 6. Deformed shapes of HMS full-beam configurations with symmetric uniform residual magnetic flux density about the mid-point under combined mechanical and magnetic load. Non-dimensional deformed configurations (ξ, η) of HMS full beams with the coefficient of residual magnetic flux density $S = 1$ and $S = -1$ under non-dimensional mechanical force $C = 10$ in combination with different magnitudes of non-dimensional magnetic load $B = rC$ in terms of the magnetic load ratio r with the inclination angles of the mechanical and magnetic loads of **(a)** $\alpha = \beta = \pi/2$, **(b)** $\alpha = \beta = \pi/3$, **(c)** $\alpha = \beta = \pi/4$, and **(d)** $\alpha = \beta = \pi/6$.

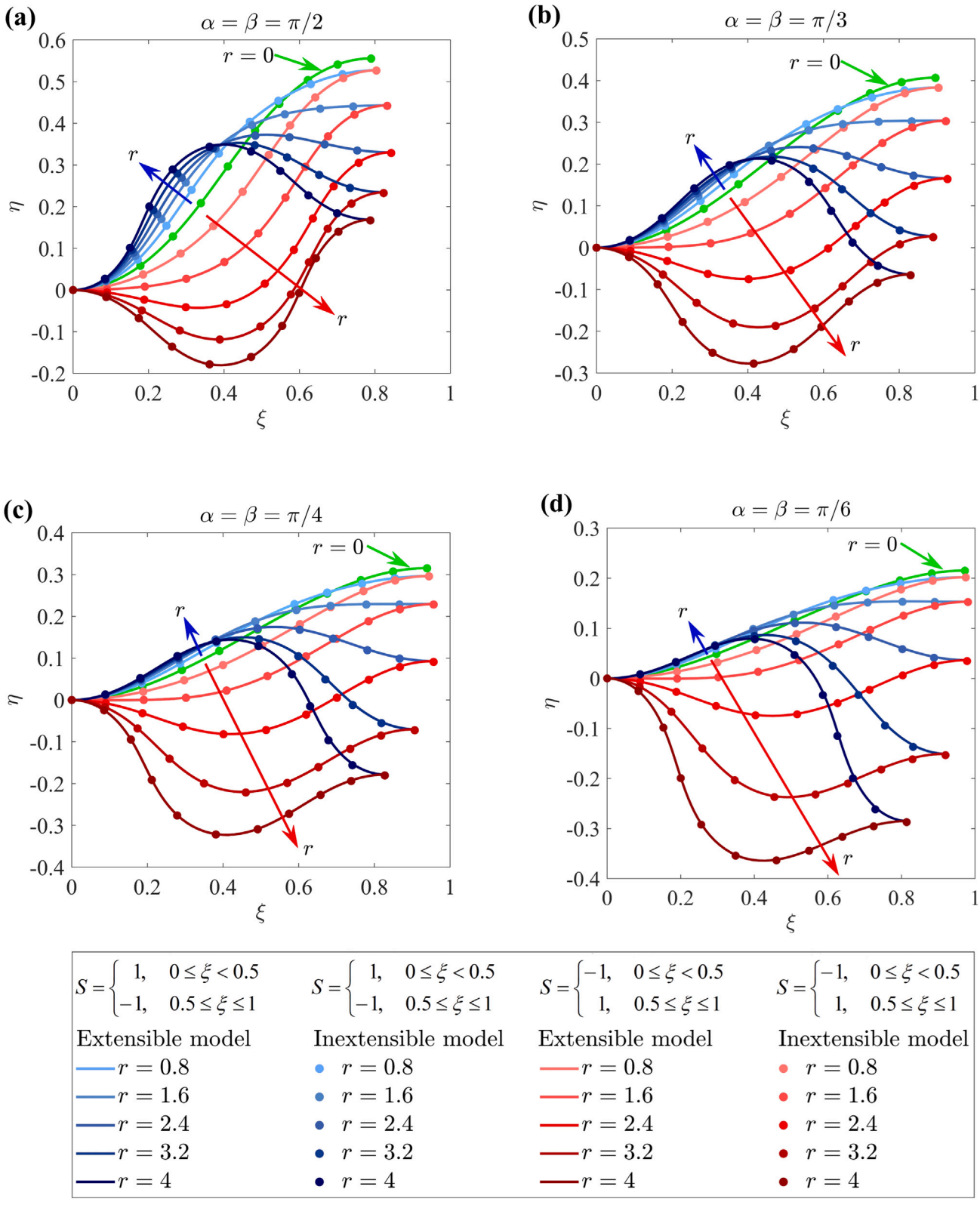

Fig. 7. Deformed shapes of HMS full-beam configurations with asymmetric residual magnetic flux density about the mid-point under combined mechanical and magnetic load. Non-dimensional deformed configurations (ξ, η) of HMS full-beam with asymmetric residual magnetic flux density under non-dimensional mechanical force $C = 10$ in combination with different magnitudes of non-dimensional magnetic load $B = rC$ in terms of the magnetic load ratio r with the inclination angles of the mechanical and magnetic loads as **(a)** $\alpha = \beta = \pi/2$, **(b)** $\alpha = \beta = \pi/3$, **(c)** $\alpha = \beta = \pi/4$, and **(d)** $\alpha = \beta = \pi/6$.

that for the considered two designs of $S(\xi)$, the deflections got reduced compared to the loading condition of mechanical load only ($r = 0$).

The HMS full-beam with the considered two asymmetric distributions of residual magnetic flux density is tried to be modelled now as two HMS half-length beams either with $S = 1$ or with $S = -1$. Load–deformation characteristics of such HMS half-length beams are already presented in Figures S4 and S5. Comparisons of the deflection results for the HMS full-beam with asymmetric residual magnetic flux density as presented in Figs. 7 and S6 with those for the HMS half-beam as presented in Figures S4 and S5 depicts that the deflections through the half-beam model are not half of the deflections obtained through the full-beam model. However, for symmetric residual magnetic flux density, we got exactly the half deflections from the half-beam model compared to the full-beam model under the same condition of combined mechanical and magnetic loading as described through comparisons between Figs. 6–S5. Hence, it is concluded from the comparison studies that modelling of HMS full-beam with one fixed end and the other end being rotationally restrained but free to translation as two half-length cantilever beams is only possible when the residual magnetic flux density is symmetric about the mid-point of the HMS full-beam. As we focus on both symmetric and asymmetric designs of $S(\xi)$ for modulation of effective elastic moduli of HMS beam networks, the two beam models are applied carefully for analysing nonlinear hexagonal lattices in the following subsections.

Comparisons of the deflection results between the extensible and inextensible versions of the present semi-analytical HMS beam model as presented in Figs. 6–S6 clearly show that the effect of centreline extension is not significant for the considered HMS beam under combined mechanical and magnetic loads. For achieving higher level of accuracy, we will consider the generalized extensible model in the further computations of effective elastic moduli of the HMS beam networks.

3.3. Periodic beam network-level validation

As the hexagonal lattice consisting of HMS beam members subjected to combined mechanical and magnetic loads is not investigated in the literature, directly comparable results for the presently developed semi-analytical framework are not readily available for reference and validation. Hence, the current semi-analytical framework estimating non-linear effective elastic moduli of hexagonal HMS beam network under combined mechanical and magnetic loads is validated for the special case of zero magnetic field ($r_i = 0$) subjected to different modes of mechanical stress only (σ_1 or σ_2 or τ). Validations for the non-linear effective elastic moduli E_1 and ν_{12} under normal mechanical stress σ_1 and for the elastic moduli E_2 and ν_{21} under normal mechanical stress σ_2 are carried out by comparing with the results presented by Ghuku and Mukhopadhyay (2022a). Whereas, for the non-linear effective shear modulus G_{12} under the shear mode of mechanical stress τ, the semi-analytical framework is validated by comparing with the paper by Fu et al. (2016).

The validation study for non-linear elastic moduli (E_1, ν_{12}, E_2, and ν_{21}) of the hexagonal HMS beam network under the normal modes of mechanical stress only (σ_1 and σ_2) (Ghuku and Mukhopadhyay, 2022a) is carried out for the lattice configuration with the geometric specifications $h/l = 2$, $t/l = 0.01$, and $\theta = \pi/6$. Young's modulus of the intrinsic material is taken as $E_s = 200$ GPa in the reference literature (Ghuku and Mukhopadhyay, 2022a). Whereas, for the present semi-analytical model, the material constitutive parameters are considered as $C_{10} = 0.2712$, $C_{20} = 0.0305$, and $C_{30} = -0.004$ within the framework of the Yeoh hyperelastic model (Xu and Liu, 2018). In the reference literature (Ghuku and Mukhopadhyay, 2022a), the non-linear results are presented as the variations of the non-dimensional elastic moduli $\bar{E}_1$, ν_{12}, $\bar{E}_2$, and ν_{21} with the dimensional input normal stress σ_1 and σ_2. As the elastic moduli are presented in non-dimensional forms, they are independent of the intrinsic material property E_s. However, the dimensional form of the input normal stress σ_1 and σ_2 makes the results dependent on the intrinsic material property E_s. Hence, to make the input normal stress independent of the material property E_s, the stresses σ_1 and σ_2 are also expressed in non-dimensional forms following Eq. (58) as $\bar{\sigma}_1 = \sigma_1/E_s\rho^3$ and $\bar{\sigma}_2 = \sigma_2/E_s\rho^3$. Variations of the non-dimensional effective Young's modulus $\bar{E}_1$ and the Poisson's ratio ν_{12} of the considered hexagonal lattice configuration with the non-dimensional compressive and tensile modes of normal stress $\bar{\sigma}_1$ are compared considering the present model, the results reported in the paper (Ghuku and Mukhopadhyay, 2022a), and the linear small-deformation analytical model (Gibson and Ashby, 1999) as presented in Figure S7(a) and (b). The similar comparison plots for the non-dimensional effective Young's modulus $\bar{E}_2$ and the Poisson's ratio ν_{21} under the non-dimensional compressive and tensile modes of normal stress $\bar{\sigma}_2$ are presented in Figure S7(c) and (d).

The comparison plots in Figure S7 depict that the non-dimensional effective elastic moduli $\bar{E}_1$, ν_{12}, $\bar{E}_2$, and ν_{21} of the hexagonal HMS beam network under normal modes of mechanical stress $\bar{\sigma}_1$ and $\bar{\sigma}_2$ as estimated by the present model match exactly with the non-linear model in literature (Ghuku and Mukhopadhyay, 2022a) at lower input stress level. However, the differences between them increase with the input stress level. The geometric exactness in non-linear kinematics and the hyperelastic material model of the present framework is the possible cause of this difference with the model reported in Ghuku and Mukhopadhyay (2022a). However, the differences in the elastic moduli at the higher stress levels are not very significant. Moreover, the increasing or decreasing trends of the elastic moduli with the input stress magnitudes agree well between the present model and the non-linear model reported in literature (Ghuku and Mukhopadhyay, 2022a). As also observed from Figure S7 that within the small deformation regime, the non-linear elastic moduli match exactly with the conventional analytical solutions (Gibson and Ashby, 1999). Differences between the elastic moduli estimated by the present framework and the linear solutions (Gibson and Ashby, 1999) increase with input stress magnitude due to the non-linearity in the system which is not considered in the conventional linear analytical solutions (Gibson and Ashby, 1999).

The validation study of the present non-linear framework for the effective shear modulus G_{12} of hexagonal HMS beam network under shear mode of mechanical stress τ is carried out for the auxetic configuration with $\theta = -\pi/6$ in terms of shear strain γ_{12} versus non-dimensional shear stress τ/E_s curve and shear strain γ_{12} versus non-dimensional shear modulus G_{12}/E_s curve following similar representation scheme of the reference literature (Fu et al., 2016). The shear strain γ_{12} versus shear stress τ/E_s curves for the auxetic lattice configuration with $h/l = 2$ and $t/l = 0.1$ as obtained from the present model, the model reported by Fu et al. (2016), and the analytical model (Gibson and Ashby, 1999) are compared in Figure S8(a). Whereas, the similar comparison of stress–strain curves under the shear mode of mechanical stress for the auxetic lattice configuration with $h/l = 2$ and $t/l = 0.12$ is shown in Figure S8(b). On the other hand, variations of the non-dimensional effective shear modulus G_{12}/E_s with the shear strain γ_{12} are compared considering the present model, the model reported by Fu et al. (2016), and the analytical model (Gibson and Ashby, 1999) in Figure S8(c) and (d) for two lattice configurations with $h/l = 1.5$, $t/l = 0.1$ and $h/l = 2$, $t/l = 0.1$ respectively.

The comparison plots in Figure S8(a) and (b) show that the stress–strain curves (γ_{12} versus τ/E_s) of the HMS beam network under the shear mode of mechanical stress τ as estimated by the present semi-analytical framework match exactly with the analytical solutions (Gibson and Ashby, 1999) within the small deformation regime. The non-linear stress–strain curves estimated by the present framework also match with the non-linear model (Fu et al., 2016) at the lower shear strain levels within the non-linear zone. However, with the increase in the shear strain γ_{12}, the differences between the non-linear stress–strain curves increase. Similar observations are found from the comparison

plots of variations of the non-dimensional effective shear modulus G_{12}/E_s of the HMS beam network with the shear strain γ_{12} in Figure S8(c) and (d). The differences between the present framework and the non-linear model reported in Fu et al. (2016) arise due to the fundamental differences in their respective formulations. The present framework is developed in the geometrically exact non-linear kinematic setting considering combined bending and axial deformations with the hyperelastic constitutive material model. Whereas, the model reported in the reference literature (Fu et al., 2016) is developed within the geometric non-linear kinematic setting excluding the axial deformation considering linear elastic constitutive material characteristics. Though the non-linear shear stiffness of the HMS beam network as predicted by the present framework has some difference at the higher strain levels, the trends are the same with the non-linear model reported in literature (Fu et al., 2016). Within the framework of the existing fundamental differences in the formulations (where the present model is more accurate), the validation study of the present model with the non-linear model from literature (Fu et al., 2016) for the effective shear stiffness of the HMS beam networks can be considered quite satisfactory.

In this subsection, we have primarily concentrated on the hexagonal lattices with non-auxetic and auxetic geometries for lattice-level validation, depending on the availability of reference literature. While rectangular brick, re-entrant auxetic and rhombic geometries are direct derivatives of hexagonal lattices (thus no need for additional validation), the triangular and rectangular lattice configurations are further validated later in their respective subsections.

3.4. Hexagonal periodic HMS beam networks under uniform residual magnetic flux density

Effect of the magnetic field B^a along direction-2 in combination with a particular mode of mechanical stress (σ_1 or σ_2 or τ) on the non-linear effective elastic moduli of the hexagonal HMS beam network having uniform residual magnetic flux density $S = 1$ and $S = -1$ is investigated in this subsection. As mentioned earlier, under the combined loading of normal stress σ_1 and magnetic field B^a, we will focus on the longitudinal non-dimensional Young's modulus $\bar{E}_1$ and Poisson's ratio ν_{12}. Under the combined loading of σ_2 and B^a, we will focus on the transverse non-dimensional Young's modulus $\bar{E}_2$ and Poisson's ratio ν_{21}. Whereas, under the combined loading of shear stress τ and magnetic field B^a, we will investigate the effective non-dimensional shear modulus $\bar{G}_{12}$. For a particular mechanical loading mode in combination with the magnetic field, the hexagonal HMS beam network is subjected to mechanical stress incrementally in 50 steps. At each step of mechanical loading, the incremental magnetic load is applied to the hexagonal HMS beam network in terms of the magnetic load ratio r_i through 100 steps.

Variations of the non-dimensional effective Young's modulus $\bar{E}_1$ of the hexagonal HMS beam network having the uniform residual magnetic flux density $S = 1$ as a function of the magnetic load ratio r_i at different stress levels under the compressive mechanical stress σ_1 in combination with the magnetic field B^a are shown in Fig. 8(a). Under the same combined loading conditions for the hexagonal HMS beam network having the negative uniform residual magnetic flux density $S = -1$, variations of the Young's modulus $\bar{E}_1$ with the magnetic load ratio r_i are shown in Fig. 8(b). Whereas, under the tensile mode of the mechanical normal stress σ_1 in combination with the magnetic field B^a, the similar plots of the non-dimensional Young's modulus of the hexagonal HMS beam network with $S = 1$ and $S = -1$ are shown in Fig. 8(c) and (d) respectively. Variations of the effective Poisson's ratio ν_{12} of the hexagonal HMS beam network having the uniform residual magnetic flux density $S = 1$ and $S = -1$ as a function of the magnetic load ratio r_i for the same combined loading conditions as of Fig. 8(a)–(d) are presented in Fig. 9(a)–(d).

Effects of the magnetic field along with the residual magnetization pattern in combination with different modes of far-field mechanical loading on the non-linear variations of the elastic moduli as function of the input stress magnitude are investigated here. As observed in Figs. 8(a), (c), (d), and 9(a), (c), (d), singularity points for the effective Young's modulus $\bar{E}_1$ and Poisson's ratio ν_{12} arise at some magnetic load ratios r_i for the hexagonal HMS beam network with $S = 1$ under both tension and compression and for the hexagonal HMS beam network with $S = -1$ under tensile mode only. The beam-level deflections under the magnetic load B^a corresponding to singular magnetic load ratios r_i balance the deflections under the corresponding far-field mechanical stress levels σ_1. Hence, at those magnetic load ratios r_i, the effective Young's modulus $\bar{E}_1$ and Poisson's ratio ν_{12} of the hexagonal HMS beam network become undefined due to no effective lattice-level strain. However, such singularity points for the effective Young's modulus $\bar{E}_1$ and Poisson's ratio ν_{12} do not arise for the hexagonal HMS beam network with $S = -1$ under the compressive mode of the mechanical stress σ_1 in combination with the magnetic field B^a as observed in Figs. 8(b) and 9(b). As also observed from Fig. 8 that under certain combinations of the mechanical and magnetic loading, negative stiffness of the hexagonal HMS beam network can be achieved. To observe the effect of the magnetic load in terms of the magnetic load ratio r_i on the effective stiffness of the hexagonal HMS beam network, variations of the non-dimensional Young's modulus $\bar{E}_1$ with the input stress σ_1 for equally spaced magnetic load ratios r_i are further presented in Figure S9(a)–(d). For the same magnetic load ratios r_i, variations of the Poisson's ratio ν_{12} with the input stress σ_1 are presented in Figure S10(a)–(d). The variations of the elastic moduli with the input stress magnitude is coming from the geometric non-linearity due to large deformation and material non-linearity under magneto-mechanical coupling.

As observed from Figure S9(a), the effective non-dimensional Young's modulus $\bar{E}_1$ of the hexagonal HMS beam network with $S = 1$ decreases with the input stress magnitude under the compressive mechanical stress σ_1 in combination with the magnetic load having the magnetic load ratio $0 \leq r_i \leq 0.4$. Under the same loading condition for the magnetic load ratio $0.6 \leq r_i \leq 0.7$, negative stiffness of the HMS beam network is observed. The negative stiffness initially increases with the stress magnitude σ_1 and then starts decreasing at the higher stress levels. However, both the positive and negative non-dimensional Young's modulus increases with the magnetic load ratio r_i. Maximum 225.5% enhancement in the positive Young's modulus $\bar{E}_1$ is observed from Figure S9(a) compared to the only mechanical loading condition ($r_i = 0$). Whereas, the maximum enhancement in the negative Young's modulus $\bar{E}_1$ is achieved as 74.2% for $r_i = 0.7$ compared to $r_i = 0.6$. Under the compressive stress σ_1 in combination with the magnetic load having $0 \leq r_i \leq 3$ for the hexagonal HMS beam network with $S = -1$ as observed from Figure S9(b), $\bar{E}_1$ decreases with the input stress magnitude σ_1 for lower r_i. However, for higher r_i, $\bar{E}_1$ initially decreases and then increases with σ_1. The overall non-dimensional Young's modulus $\bar{E}_1$ decreases with the magnetic load ratio r_i. A maximum 84% reduction in $\bar{E}_1$ is observed in Figure S9(b) for $r_i = 3$ compared to $r_i = 0$.

As evident from Figure S9(c), for the hexagonal HMS beam network with $S = 1$ under the tensile mode of mechanical normal stress σ_1 in combination with the magnetic load having $0 \leq r_i \leq 1.5$, the non-dimensional Young's modulus $\bar{E}_1$ increases with the stress amplitude. The overall $\bar{E}_1$ decreases with the magnetic load ratio r_i at the lower stress zone, however, at the higher input stress level σ_1, it has some mixed trend with r_i. Maximum enhancement and reduction in the non-dimensional Young's modulus $\bar{E}_1$ compared to the only mechanical loading condition ($r_i = 0$) are obtained as 44.1% and 72.1% respectively. Under the combined tensile stress σ_1 and magnetic field with $0 \leq r_i \leq 0.4$ for the HMS beam network with the negative residual magnetic flux density $S = -1$, the positive non-dimensional Young's modulus $\bar{E}_1$ increases with the stress amplitude as observed from Figure S9(d). For the magnetic load ratio $1 \leq r_i \leq 2$, the non-dimensional

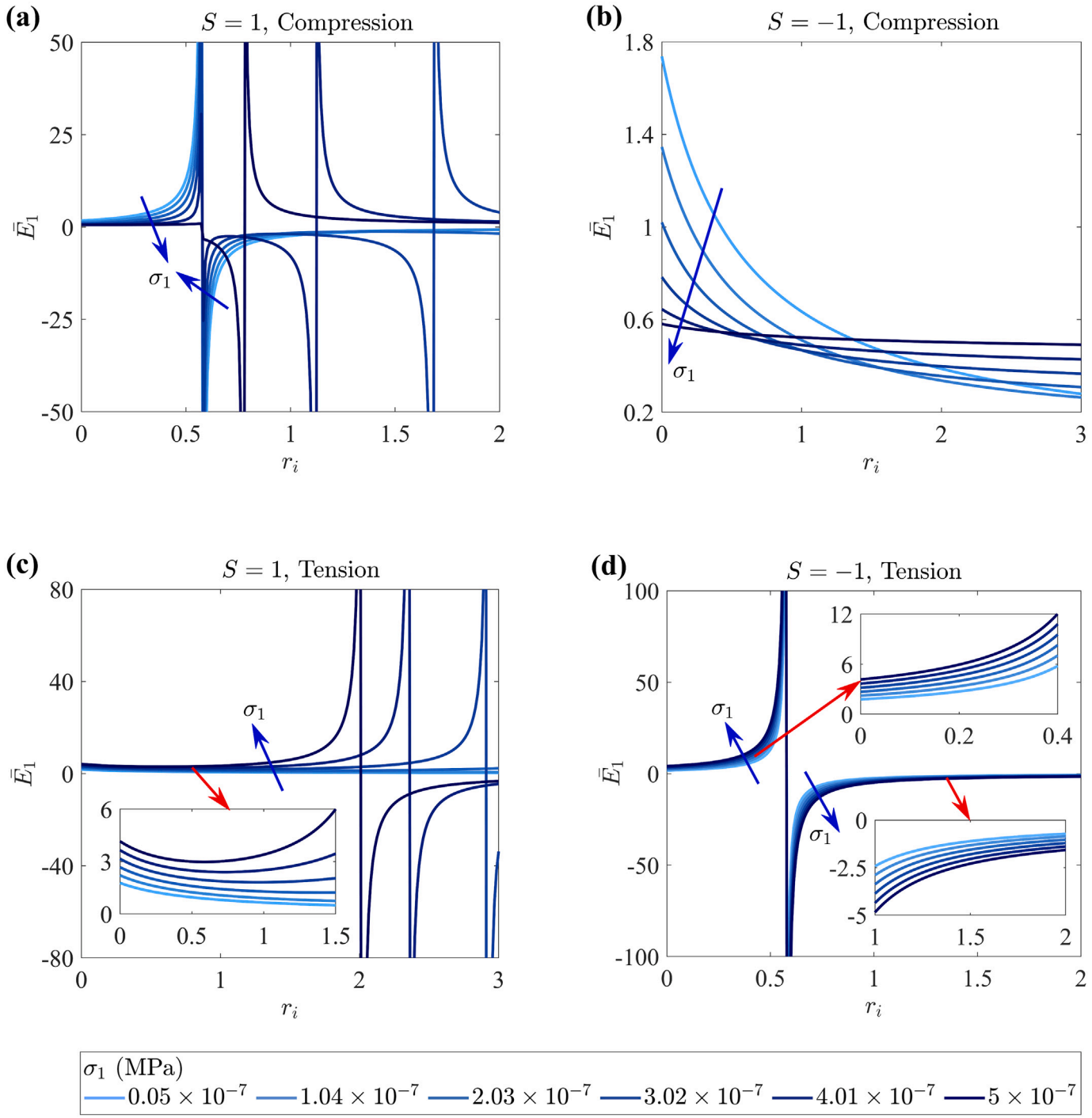

Fig. 8. Effective Young's modulus of hexagonal HMS beam networks having uniform residual magnetic flux density under combined mechanical normal stress along direction-1 and magnetic field along direction-2. Variations of the non-dimensional effective Young's modulus $\bar{E}_1$ of the hexagonal HMS beam network having uniform residual magnetic flux density **(a, c)** $S = 1$ and **(b, d)** $S = -1$ as function of the magnetic load ratio r_i at different mechanical stress levels σ_1 under the **(a, b)** compressive and **(c, d)** tensile modes of the mechanical stress σ_1 in combination with the magnetic field B^a along direction-2.

Young's modulus $\bar{E}_1$ is negative which decreases with σ_1. However, both the positive and negative Young's modulus $\bar{E}_1$ increases with r_i. As obtained from Figure S9(d), the maximum enhancements in the positive and negative $\bar{E}_1$ are found to be 189.1% and 67.6% respectively.

As observed from Figure S10(a), for the hexagonal HMS beam network with $S = 1$ under the combined compressive stress σ_1 and magnetic load, the effective Poisson's ratio ν_{12} decreases with σ_1 for $0 \leq r_i \leq 0.4$ and increases with σ_1 for $0.6 \leq r_i \leq 0.7$. However, for both the ranges of r_i, the overall Poisson's ratio ν_{12} has an increasing trend with the magnetic load ratio r_i. The maximum enhancements in ν_{12} for the two ranges of r_i are found to be 29.8% and 232.8% respectively. Under the same combined loading conditions for the HMS beam network with $S = -1$ as presented in Figure S10(b), the effective Poisson's ratio ν_{12} has decreasing trends with both σ_1 and r_i. A maximum 29.8% reduction in ν_{12} is observed compared to the only mechanical loading condition $r_i = 0$. As evident from Figure S10(c), the effective Poisson's ratio ν_{12} of the HMS beam network with $S = 1$ increases with both input tensile stress magnitude σ_1 and the magnetic load ratio r_i. The maximum enhancement in ν_{12} compared to the loading condition of $r_i = 0$ is found to be 449.2%. Under the combined loading of tensile σ_1 and

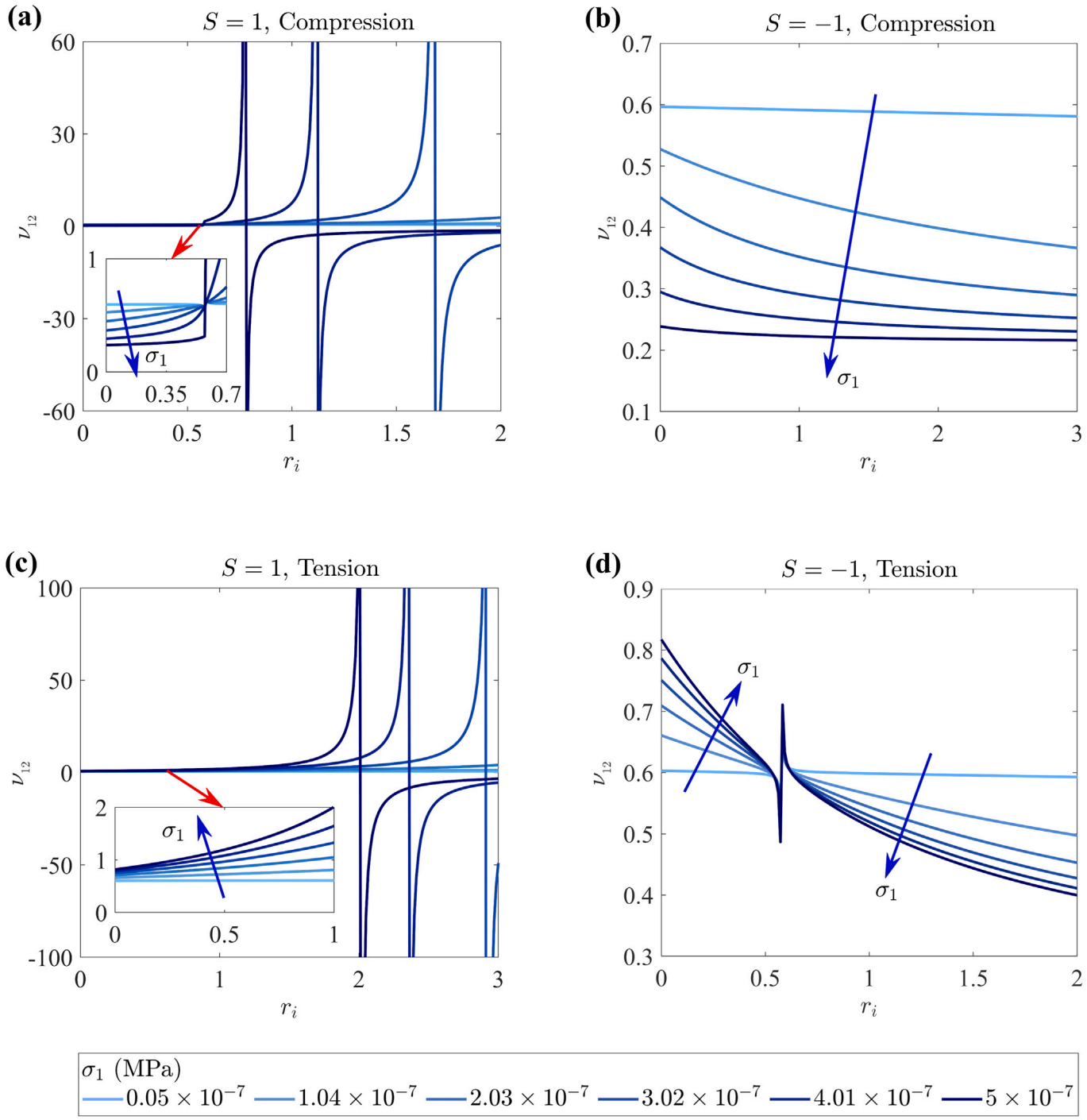

Fig. 9. Effective Poisson's ratio of hexagonal HMS beam networks having uniform residual magnetic flux density under combined mechanical normal stress along direction-1 and magnetic field along direction-2. Variations of the effective Poisson's ratio ν_{12} of the hexagonal HMS beam network having uniform residual magnetic flux density **(a, c)** $S = 1$ and **(b, d)** $S = -1$ as function of the magnetic load ratio r_i at different mechanical stress levels σ_1 under the **(a, b)** compressive and **(c, d)** tensile modes of the mechanical stress σ_1 in combination with the magnetic field B^a along direction-2.

r_i within the range $0 \leq r_i \leq 0.4$, ν_{12} of the HMS beam network with $S = -1$ increases with σ_1 as observed from Figure S10(d). For the range $1 \leq r_i \leq 2$, ν_{12} decreases with σ_1. For both the ranges of r_i, the overall effective Poisson's ratio ν_{12} has decreasing trends with r_i. The maximum reductions in ν_{12} for the considered two ranges of r_i are obtained from Figure S10(d) as 20.6% and 21.9% respectively.

Under the compressive and tensile normal stress along direction-2 (σ_2) in combination with the magnetic field along direction-2 (B^a), effects of the magnetic load ratio r_i and input stress magnitude σ_2 on the non-dimensional elastic moduli $\bar{E}_2$ and ν_{21} of the hexagonal HMS beam network with uniform residual magnetic flux density $S = 1$ and $S = -1$ are shown in Figs. 10–S12 following the representation scheme for the combined loading σ_1 and B^a (refer to Figs. 8–S10). Figs. 10(b), (c), and 11(b), (c) depict that for the hexagonal HMS beam network with $S = -1$ under compression and the hexagonal HMS beam network with $S = 1$ under tension, singularity points on the effective $\bar{E}_2$ and ν_{21} arise at some magnetic load ratios r_i. However, for the other two configurations as presented in Figs. 10(a), (d), and 11(a), (d), such phenomena are not observed.

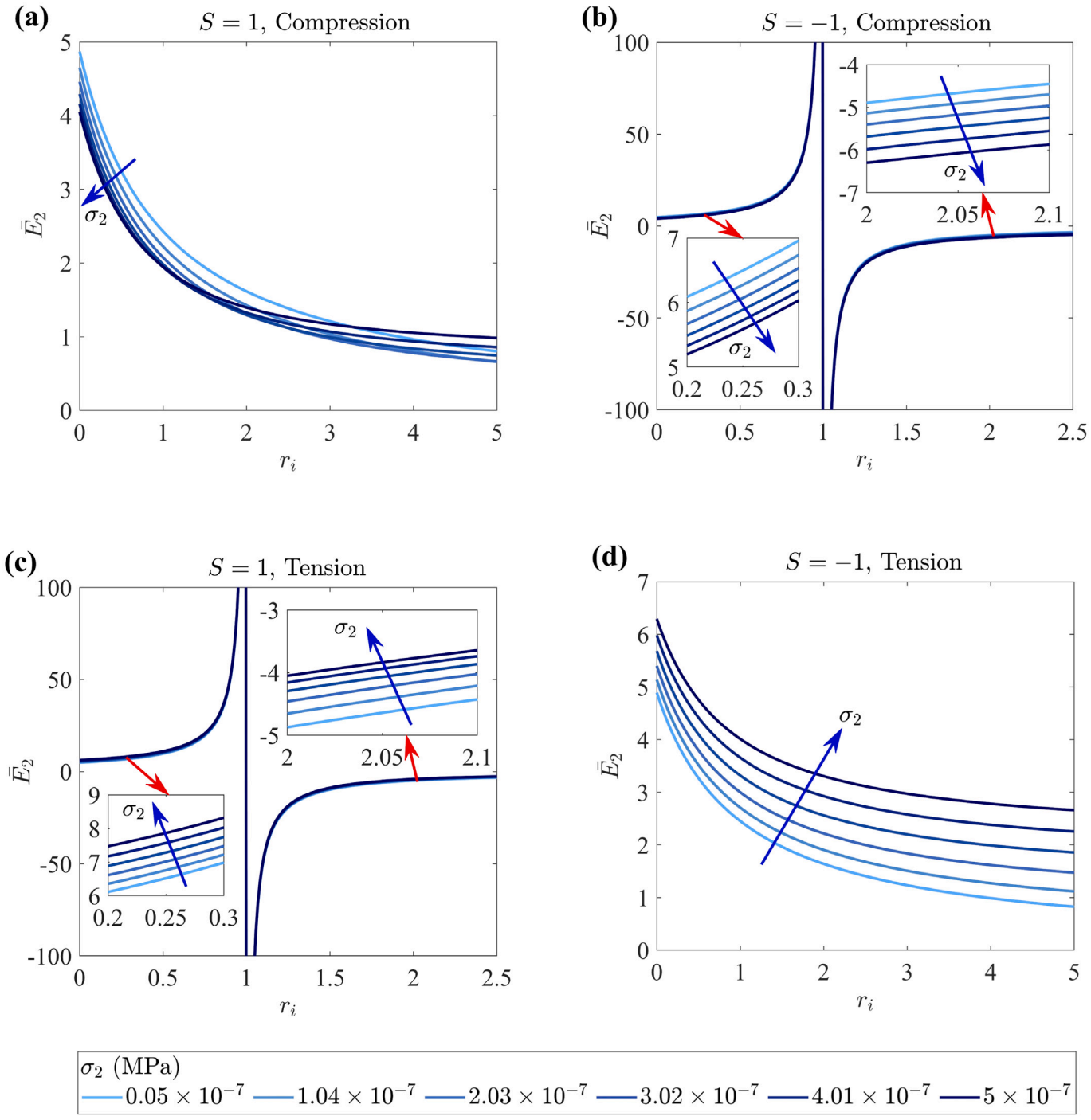

Fig. 10. Effective Young's modulus of hexagonal HMS beam networks having uniform residual magnetic flux density under combined mechanical normal stress along direction-2 and magnetic field along direction-2. Variations of the non-dimensional effective Young's modulus $\bar{E}_2$ of the hexagonal HMS beam network having the uniform residual magnetic flux density **(a, c)** $S = 1$ and **(b, d)** $S = -1$ as function of the magnetic load ratio r_i at different mechanical stress levels σ_2 under the **(a, b)** compressive and **(c, d)** tensile modes of the mechanical stress σ_2 in combination with the magnetic field B^a along direction-2.

As observed from Figure S11(a), the non-dimensional effective Young's modulus $\bar{E}_2$ of the hexagonal HMS beam network with $S = 1$ decrease with compressive stress magnitude σ_2 for lower values of r_i. However, for higher values of r_i, $\bar{E}_2$ initially decreases and then increases with σ_2. The overall stiffness decreases with r_i and maximum 83.9% reduction in $\bar{E}_2$ is observed. Under the same compressive mode of mechanical loading, the positive and negative $\bar{E}_2$ of the hexagonal HMS beam network with $S = -1$ for the ranges of the magnetic load ratio $0 \leq r_i \leq 0.7$ and $1.5 \leq r_i \leq 2.5$ respectively decreases with stress magnitude σ_2 and increases with r_i as observed in Figure S11(b). The maximum enhancements in the positive and negative $\bar{E}_2$ due to the magnetic field are achieved as 233.7% and 66.6% respectively. As observed from Figure S11(c) and (d), under the tensile mode of the normal stress σ_2, the effective Young's modulus $\bar{E}_2$ increase with σ_2 for both the hexagonal HMS beam networks with $S = 1$ and $S = -1$. However, for the HMS beam network with $S = 1$, the positive and negative non-dimensional $\bar{E}_2$ increases with r_i in the considered ranges $0 \leq r_i \leq 0.7$ and $1.5 \leq r_i \leq 2.5$ respectively. Maximum 232.6% and 66.8% enhancements in the positive and negative $\bar{E}_2$ are achieved as obtained from Figure S11(c). Whereas, for the HMS beam network with

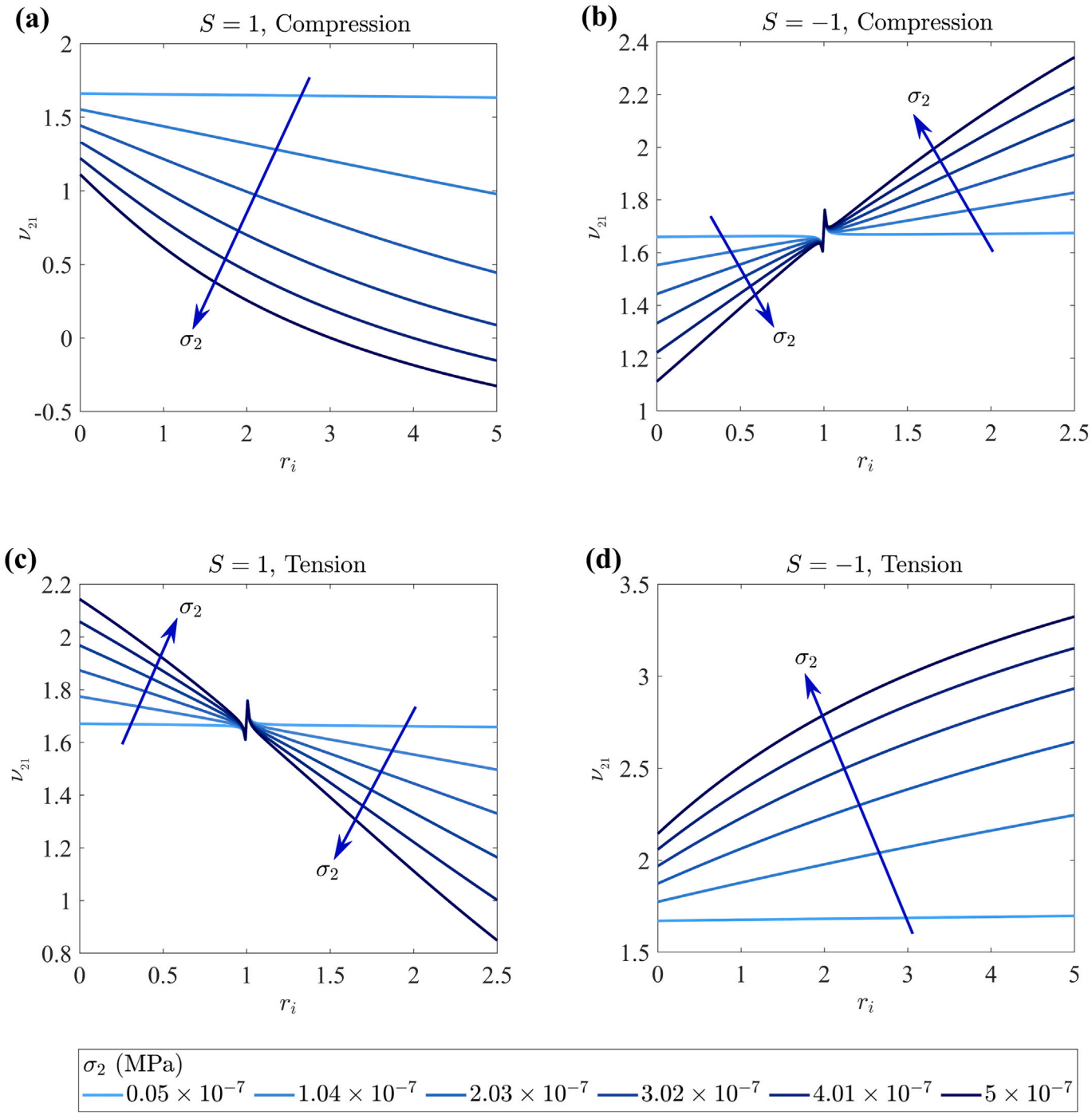

Fig. 11. Effective Poisson's ratio of hexagonal HMS beam networks having uniform residual magnetic flux density under combined mechanical normal stress along direction-2 and magnetic field along direction-2. Variations of the effective Poisson's ratio ν_{21} of the hexagonal HMS beam network having the uniform residual magnetic flux density **(a, c)** $S = 1$ and **(b, d)** $S = -1$ as function of the magnetic load ratio r_i at different mechanical stress levels σ_2 under the **(a, b)** compressive and **(c, d)** tensile modes of the mechanical stress σ_2 in combination with the magnetic field B^a along direction-2.

the negative residual magnetic flux density $S = -1$, opposite effect of r_i is observed in Figure S11(d) with the 83.1% maximum reduction with respect to the only mechanical loading condition, $r_i = 0$.

As evident from Figure S12(a), the effective Poisson's ratio ν_{21} of the hexagonal HMS beam network with $S = 1$ decreases with both the compressive stress σ_2 and magnetic load ratio r_i. A maximum 129.4% reduction in ν_{21} is observed for $r_i = 5$ compared to $r_i = 0$. For the HMS beam network with $S = -1$ under tensile mode of normal stress as presented in Figure S12(d), completely opposite effects of σ_2 and r_i are observed with the maximum 55% enhancement. As obvious from Figure S12(b), for the HMS beam network with $S = -1$ under compressive stress σ_2 in combination with the magnetic load $0 \leq r_i \leq 0.7$, the effective Poisson's ratio ν_{21} decreases with stress magnitude. For the magnetic load range $1.5 \leq r_i \leq 2.5$, an opposite effect of the non-linearity is observed. However, for both the considered magnetic load ranges, ν_{21} increases with r_i having the maximum 35.1% and 21.9% enhancements respectively. Completely opposite effects of σ_2 and r_i are observed in Figure S12(c) for the HMS beam network with $S = 1$ under tensile stress σ_2. The corresponding reductions in the effective ν_{21} due

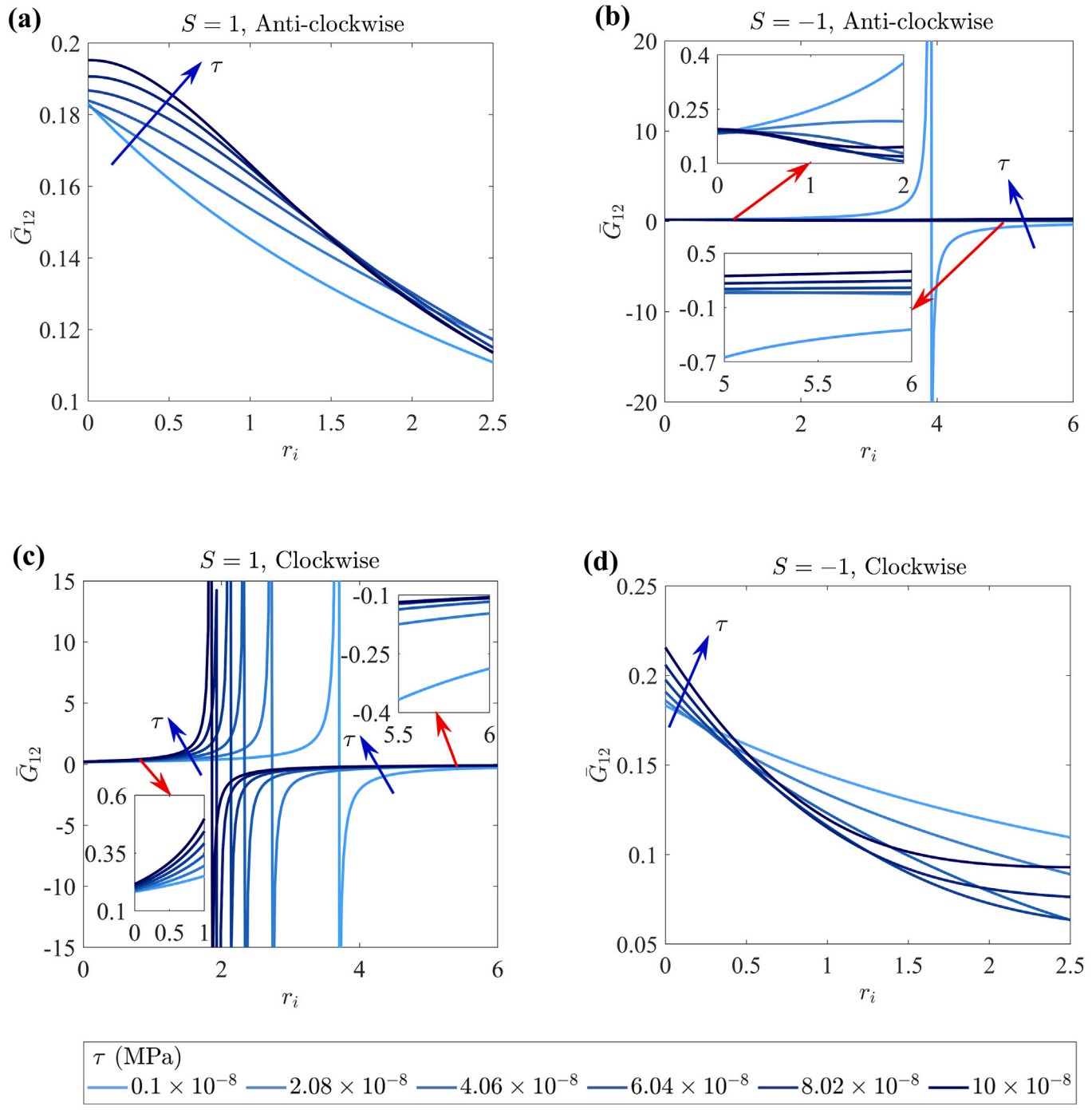

Fig. 12. Effective shear modulus of hexagonal HMS beam networks having uniform residual magnetic flux density under combined mechanical shear stress in plane 1–2 and magnetic field along direction-2. Variations of the non-dimensional effective shear modulus $\bar{G}_{12}$ of the hexagonal HMS beam network having the uniform residual magnetic flux density **(a, c)** $S = 1$ and **(b, d)** $S = -1$ as function of the magnetic load ratio r_i at different mechanical stress levels τ under the **(a, b)** anti-clockwise and **(c, d)** clockwise modes of the mechanical stress τ in combination with the magnetic field B^a along direction-2.

to the application of magnetic field are found to be 15.1% and 39% respectively.

Under the anti-clockwise and clockwise modes of the shear stress τ in combination with the magnetic field B^a along direction-2, combined effects of the magnetic load ratio r_i and the input stress magnitude τ on the non-dimensional shear modulus $\bar{G}_{12}$ of the hexagonal HMS beam network with uniform residual magnetic flux density $S = 1$ and $S = -1$ are shown in Figs. 12 and S13 following similar representation scheme for the combined loading condition of normal stress and magnetic field. As obvious from Fig. 12(b) and (c), for the HMS beam network with $S = -1$ under anti-clockwise shear stress and the HMS beam network with $S = 1$ under clockwise shear stress, singularity points arise at some r_i values. For these combined loading cases, negative shear modulus is observed under certain combinations of τ and r_i. Whereas, for the other two combined loading conditions as presented in Fig. 12(a) and (d), such singularity points of the shear modulus do not arise.

As obvious from Figure S13(a) and (d), for the hexagonal HMS beam network with $S = 1$ under anti-clockwise shear stress and the hexagonal HMS beam network with $S = -1$ under clockwise shear stress, the effective non-dimensional shear modulus $\bar{G}_{12}$ increases with

stress magnitude τ for the lower values of r_i. Whereas, for the higher magnetic loading r_i, mixed increasing–decreasing effects of the stress magnitude are observed. However, for both the configurations, r_i has the same decreasing effects with the corresponding 41.8% and 68.4% maximum reductions in $\bar{G}_{12}$. For the HMS beam network with the negative magnetization $S = -1$ under the anti-clockwise mode of shear stress τ as presented in Figure S13(b), some irregular effects of the stress magnitude τ and the magnetic load ratio r_i are observed on the non-dimensional positive $\bar{G}_{12}$ for $0 \leq r_i \leq 3$ and the mixed negative–positive $\bar{G}_{12}$ for $5 \leq r_i \leq 6$. The maximum enhancement and reduction in the positive $\bar{G}_{12}$ are found to be 339.6% and 56.8% respectively. Whereas, the maximum enhancement in the negative $\bar{G}_{12}$ is observed as 47.3%. For the HMS beam network with $S = 1$ under the clockwise shear stress τ as presented in Figure S13(c), the positive non-dimensional shear modulus $\bar{G}_{12}$ for $0 \leq r_i \leq 1.5$ increases with the input stress amplitude. However, for the magnetic load range $5 \leq r_i \leq 6$, the negative $\bar{G}_{12}$ initially increases with τ but at the higher stress level becomes almost independent of τ. Both the positive and negative $\bar{G}_{12}$ of the HMS beam network increase with r_i resulting in maximum 463.4% and 43.2% enhancements respectively. It is interesting no note from the trends presented for the elastic moduli, the value of applied magnetic field can be actively modulated (and optimized) based on the applied external mechanical stresses to achieve a target level of certain elastic modulus and stiffness.

3.5. Periodic HMS beam network with optimally-architected residual magnetic flux density

As described in the mathematical formulation in Section 2.3.1, the beam elements of the hexagonal HMS beam network are subjected to finite moments at the ends with zero moment at the mid-point due to the typical rotationally boundary conditions. Based on the kinetic conditions, two sets of intuitive designs of the residual magnetic flux density ($S(\xi)$) are proposed having maximum hard particle density at the endpoints with zero at the mid-point of the HMS beam elements. In the first set of design, we consider either $S = 1$ or $S = -1$ at both the ends $\xi = 0, 1$ with $S = 0$ at the mid-point $\xi = 0.5$. The variation of $S(\xi)$ along the normalized coordinate ξ is defined by the following equation with the degree of non-linearity n.

$$S(\xi) = \begin{cases} \pm(1-2\xi)^n, & 0 \leq \xi < 0.5 \\ \pm(-1+2\xi)^n, & 0.5 \leq \xi \leq 1 \end{cases}$$

For the second set of design, $S(\xi)$ is varying either from $S = -1$ to $S = 1$ or from $S = 1$ to $S = -1$ between the ends $\xi = 0, 1$ with $S = 0$ at the mid-point $\xi = 0.5$. The variation of $S(\xi)$ along the normalized coordinate ξ for the second set of design of $S(\xi)$ is expressed mathematically below with the degree of non-linearity n.

$$S(\xi) = \begin{cases} \mp(1-2\xi)^n, & 0 \leq \xi < 0.5 \\ \pm(-1+2\xi)^n, & 0.5 \leq \xi \leq 1 \end{cases}$$

The positive and negative distributions of the first designed set of $S(\xi)$ along the normalized coordinate ξ with the degree of non-linearity $n = 0, 0.1, 0.25, 0.5, 1$, and 3 are shown in Fig. 13(a) and (b) respectively. Similarly, for the two cases of the second designed set of $S(\xi)$, the distribution of $S(\xi)$ along the normalized coordinate ξ are presented in Fig. 13(c) and (d) respectively. The effect of the degree of non-linearity n for the two sets of designed $S(\xi)$ on the non-linear variation of the elastic moduli of the hexagonal HMS beam network as functions of the input stress are investigated here as presented in the following paragraphs.

Variations of the non-dimensional effective Young's modulus $\bar{E}_1$ of the hexagonal HMS beam network with the input stress σ_1 for the considered six degrees of non-linearity n (0, 0.1, 0.25, 0.5, 1, and 3) of the positive and negative distribution of the first set of designed $S(\xi)$ (refer to Fig. 13(a) and (b)) under the combined compressive stress along direction-1 (σ_1) and the external magnetic field B_a along direction-2 are shown in Fig. 14(a). Whereas, the variations of $\bar{E}_1$ under the tensile mode of the normal stress σ_1 in combination with the magnetic field B_a are presented in Fig. 14(b). The similar plots showing the effects of the degree of non-linearity n on the effective Poisson's ratio ν_{12} of the hexagonal HMS beam network with the first set of designed $S(\xi)$ are shown in Fig. 14(c) and (d) respectively. The results are compared in Fig. 14 for the magnetic load ratio $r_i = 0.4$. Under the combined loading of normal stress along direction-2 (σ_2) and the magnetic field B_a along direction-2, effects of the degree of non-linearity n on the non-linear variations of the effective Young's modulus $\bar{E}_2$ and Poisson's ratio ν_{21} of the hexagonal HMS beam network with the first set of designed $S(\xi)$ are shown in Figure S14 for the magnetic load ratio $r_i = 0.5$. Whereas, similar variations of the non-linear shear modulus $\bar{G}_{12}$ of the HMS beam network with the degree of non-linearity n for the first set of designed $S(\xi)$ under the anti-clockwise and clockwise modes of shear stress (τ) in combination with the external magnetic field B_a are shown in Fig. 15 for the magnetic load ratio $r_i = 1.5$.

As observed from Fig. 14(a) and (c), the non-dimensional Young's modulus $\bar{E}_1$ and the Poisson's ratio ν_{12} non-linearly decreases with compressive stress σ_1 for both the positive and negative distribution of the first set of design of $S(\xi)$. Such non-linearity in the system stiffness is coming from the inherent geometric non-linearity due to large deformation and material non-linearity due to magneto-elastic coupling under the combined mechanical and magnetic loading. For the positive distribution of the first set of designed $S(\xi)$, the overall non-linear Young's modulus $\bar{E}_1$ and Poisson's ratio ν_{12} decrease with the degree of non-linearity n as observed in Fig. 14(a) and (c). Whereas, for the negative distribution of $S(\xi)$, the degree of non-linearity n shows the opposite increasing effect on the non-linear Young's modulus $\bar{E}_1$ and Poisson's ratio ν_{12}. Maximum 56% and 11% enhancements in the non-dimensional Young's modulus $\bar{E}_1$ and Poisson's ratio ν_{12} are achieved respectively for $n = 3$ of the negative distribution of $S(\xi)$ compared to the uniform distribution ($S = -1$) for $n = 0$ (refer to Fig. 14(a) and (c)). Whereas, maximum 66.4% and 21% reductions in $\bar{E}_1$ and ν_{12} are obtained for $n = 3$ of the positive $S(\xi)$ with respect to the uniform distribution ($S = 1$) for $n = 0$.

Under the tensile mode of the normal stress σ_1 in combination with the external magnetic field B^a as presented in Fig. 14(b) and (d), a completely opposite effect of the inherent system non-linearity is observed compared to the compressive mode of σ_1 as shown in Fig. 14(a) and (c). The non-dimensional Young's modulus $\bar{E}_1$ and the Poisson's ratio ν_{12} increase with increase in the tensile σ_1 for both the positive and negative distribution of the first set of design of $S(\xi)$. As shown in Fig. 14(b), the overall non-linear Young's modulus $\bar{E}_1$ increases with the degree of non-linearity n for the positive distribution of $S(\xi)$, whereas, it decreases with n for the negative distribution of $S(\xi)$. Whereas, as observed from Fig. 14(d), the degree of non-linearity n has the opposite effect on the non-linear Poisson's ratio ν_{12} compared to the Young's modulus $\bar{E}_1$. The maximum 31.1% and 22.7% enhancements in $\bar{E}_1$ and ν_{12} are achieved respectively for the non-linear $S(\xi)$ with $n = 3$ compared to the uniform S with $n = 0$ under the tensile mode of normal stress σ_1 in combination with the external magnetic field B^a as observed from Fig. 14(b) and (d). Whereas, the maximum reductions in the elastic moduli $\bar{E}_1$ and ν_{12} are observed as 62.6% and 23.3% respectively from Fig. 14(b) and (d) for the non-linear $S(\xi)$ with $n = 3$ compared to the uniform S with $n = 0$.

Under the normal stress along direction-2 (σ_2) in combination with the magnetic field B^a along direction-2, effects of non-linearity on the non-dimensional elastic moduli $\bar{E}_2$ and ν_{21} in terms of their variations with input stress magnitude σ_2 are observed from Figure S14 similar to the combined loading of σ_1 and B^a as presented in Fig. 14. However, the effects of the degree of non-linearity n of the first set of designed

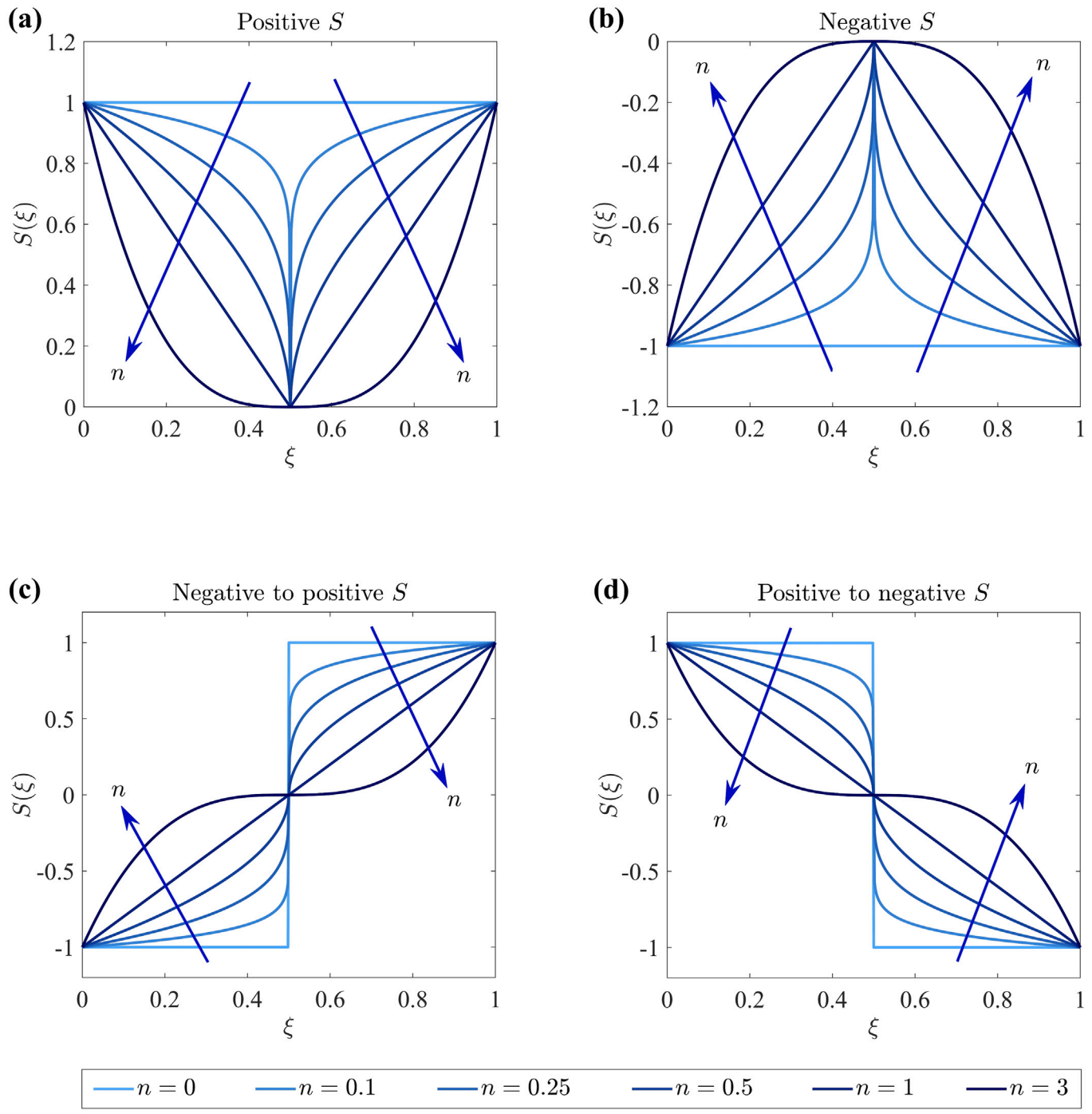

Fig. 13. Physics-informed intuitive designs of spatially-varying residual magnetic flux density in the HMS beam elements of the hexagonal HMS beam network. Distribution of the coefficient of residual magnetic flux density $S(\xi)$ along the normalized coordinate ξ with the degree of non-linearity $n = 0, 0.1, 0.25, 0.5, 1$, and 3 for: **(a, b)** the first set of design of $S(\xi)$ having (a) positive and (b) negative distribution, and **(c, d)** the second set of design of $S(\xi)$ varying (c) from $S = -1$ to $S = 1$ and (d) from $S = 1$ to $S = -1$.

$S(\xi)$ are found opposite for the combined loading of σ_2 and B^a compared to the combined loading of σ_1 and B^a. As evident from Figure S14(a) and (c), the maximum enhancements in the non-dimensional Young's modulus $\bar{E}_2$ and Poisson's ratio ν_{21} under the compressive mode of σ_2 are achieved as 42.4% and 27.5% respectively for the positive $S(\xi)$ with $n = 3$ compared to the uniform S for $n = 0$. Whereas, 47.2% and 18% reductions in $\bar{E}_2$ and ν_{21} are obtained for the negative distribution of $S(\xi)$ with $n = 3$ compared to $n = 0$. Under the tensile mode of σ_2 in combination with B^a, the maximum enhancement and reduction in $\bar{E}_2$ for $n = 3$ with respect to the uniform S ($n = 0$) are found to be 41% and 46.6% respectively from Figure S14(b). Whereas, as evident from Figure S14(d), the enhancement and reduction in ν_{21} for the non-linear $S(\xi)$ with $n = 3$ compared to $n = 0$ under the tensile mode of σ_2 in combination with B^a are obtained as 10.4% and 7.3% respectively.

As evident from Fig. 15(a) and (b), under both the anti-clockwise and clockwise modes of shear stress τ in combination with the magnetic field B^a, the non-dimensional shear modulus $\bar{G}_{12}$ increases with the input stress τ for the positive distribution of the first set of design of $S(\xi)$. Whereas, for the HMS beam network with the negative distribution of the first set of designed $S(\xi)$, the non-dimensional shear modulus $\bar{G}_{12}$ initially decreases and then increases with τ for the lower values of n.

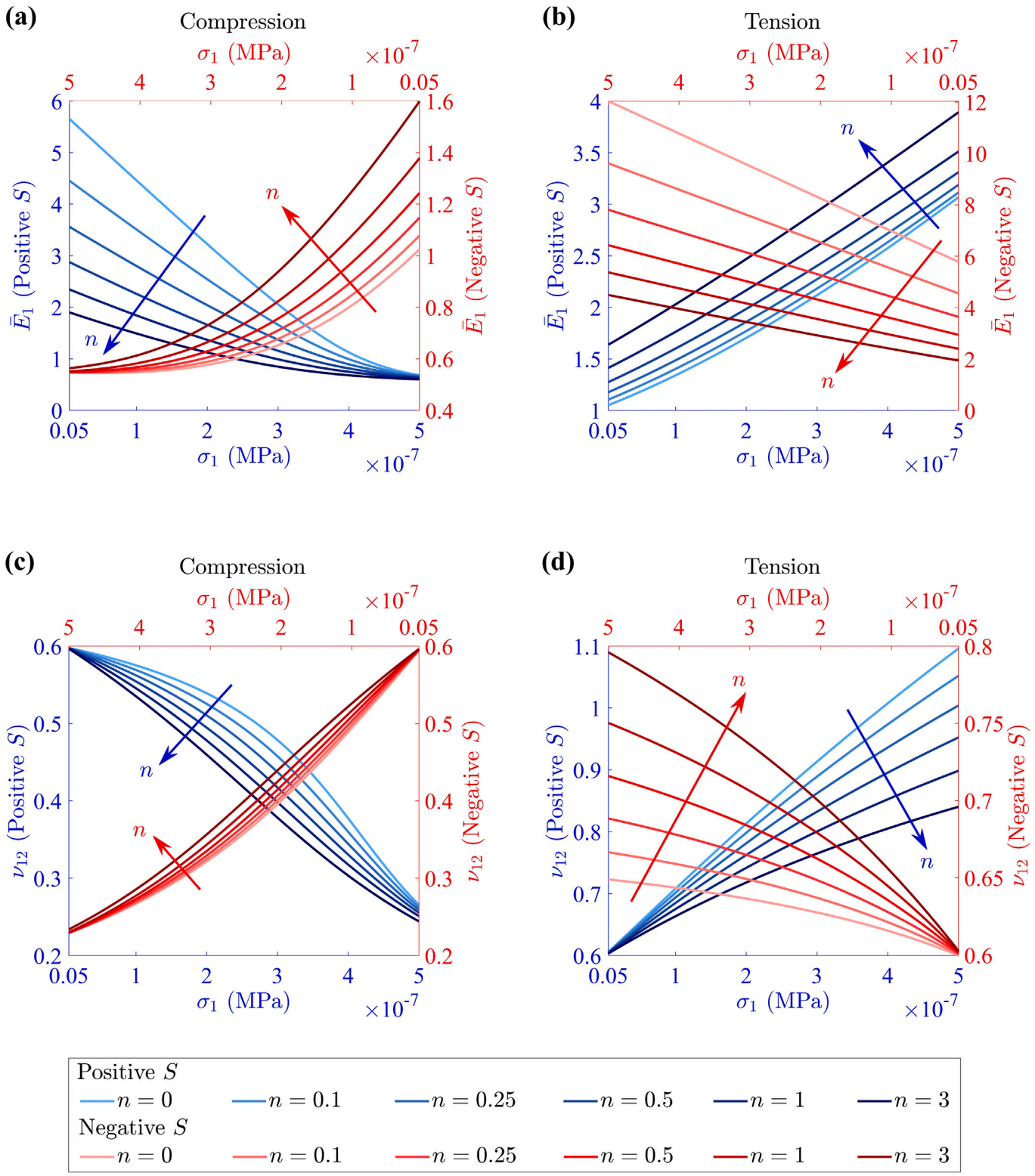

Fig. 14. Modulation of the effective elastic moduli of hexagonal HMS beam networks with the first set of designed $S(\xi)$ under the normal stress along direction-1 in combination with the magnetic field along direction-2. Variations of the **(a, b)** non-dimensional effective Young's modulus $\bar{E}_1$ and **(c, d)** effective Poisson's ratio ν_{12} of the hexagonal HMS beam network as function of the input stress σ_1 for the considered six degrees of non-linearity n $(0, 0.1, 0.25, 0.5, 1,$ and $3)$ of the positive and negative distributions of the first set of designed $S(\xi)$ under the **(a, c)** compressive and **(b, d)** tensile mode of normal stress σ_1 along direction-1 in combination with the magnetic field B^a along direction-2. The results are compared for the magnetic load ratio of the inclined member $r_i = 0.4$.

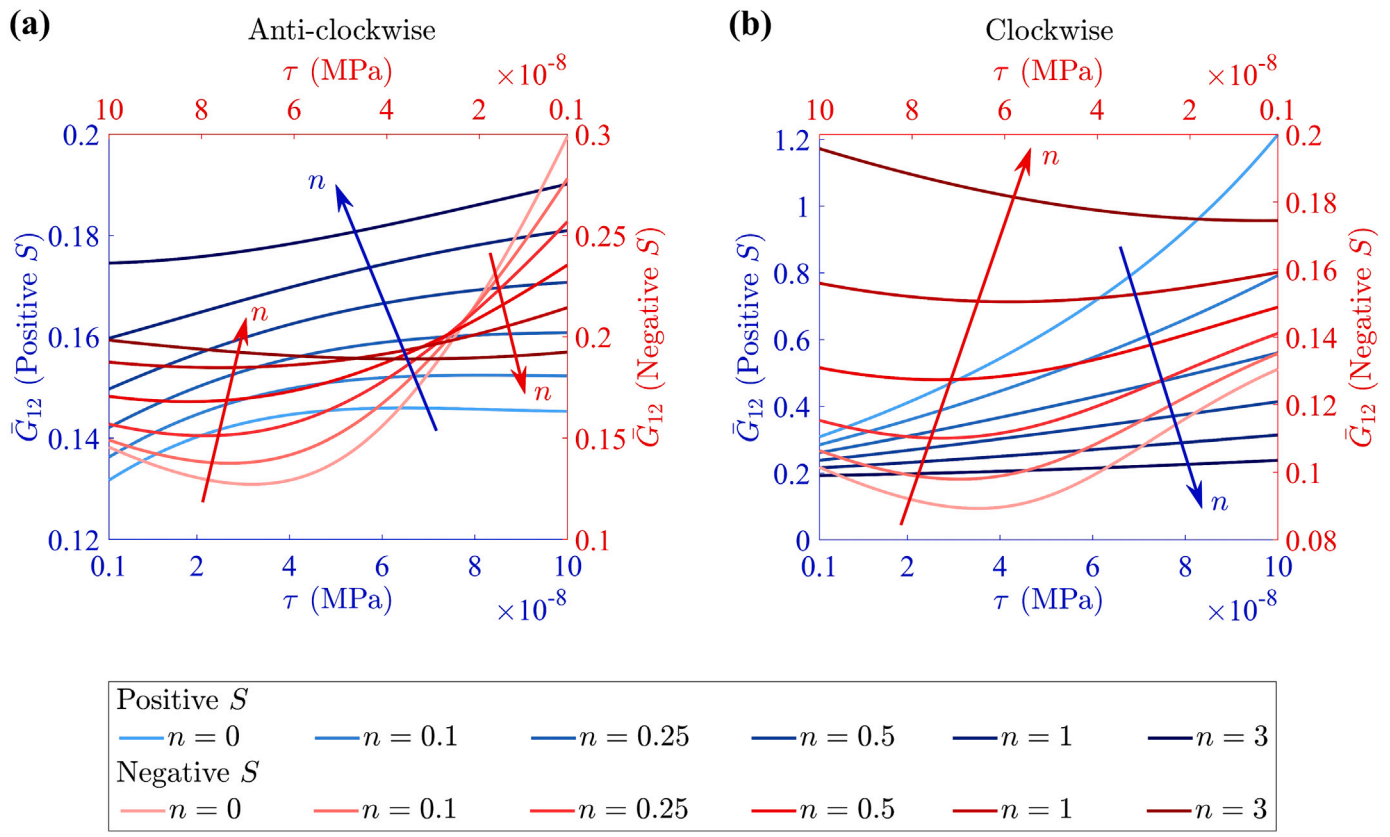

Fig. 15. Modulation of the effective shear modulus of hexagonal HMS beam networks with the first set of designed $S(\xi)$ under the shear stress in plane 1–2 in combination with the magnetic field along direction-2. Variations of the non-dimensional effective shear modulus $\bar{G}_{12}$ of the hexagonal HMS beam network as function of the input stress τ for the considered six degrees of non-linearity n $(0, 0.1, 0.25, 0.5, 1,$ and $3)$ of the positive and negative distributions of the first set of designed $S(\xi)$ under the **(a)** anti-clockwise and **(b)** clockwise mode of shear stress τ in plane 1–2 in combination with the magnetic field B^a along direction-2. The results are compared for the magnetic load ratio of the inclined member $r_i = 1.5$.

However, for the highest value of the degree of non-linearity $n = 3$, $\bar{G}_{12}$ has an increasing trend with the input stress τ amplitude. As observed from Fig. 15(a), under the anti-clockwise mode of τ in combination with the magnetic field B^a, the non-dimensional shear modulus $\bar{G}_{12}$ increases with the degree of non-linearity n for the positive distribution of the first designed set $S(\xi)$. However, for the negative distribution of $S(\xi)$, $\bar{G}_{12}$ decreases with n at the lower stress level, whereas, it increases with n at the higher stress zone. Maximum 30.9% enhancement in the non-dimensional shear modulus $\bar{G}_{12}$ is achieved for $n = 3$ of the positive distribution of the first set of designed $S(\xi)$ compared to the uniform S with $n = 0$. Whereas, the maximum reduction and enhancement in $\bar{G}_{12}$ for the negative $S(\xi)$ are observed as 35.6% and 50.9% respectively. On the other hand, under the clockwise mode of τ in combination with the magnetic field B^a as observed in Fig. 15(b), the non-dimensional shear modulus $\bar{G}_{12}$ decreases with the degree of non-linearity n for the positive distribution of $S(\xi)$. Whereas, for the hexagonal HMS beam network with negative designed $S(\xi)$, $\bar{G}_{12}$ increases with n. The maximum enhancement and reduction in $\bar{G}_{12}$ are observed from Fig. 15(b) as 104.3% and 80.4% respectively compared to the uniform S.

For the second set of design of the residual magnetic flux density (refer to Fig. 13(c) and (d)), the two opposite distributions of $S(\xi)$ varying from $S = -1$ to $S = 1$ and from $S = 1$ to $S = -1$ cause the same effects on the non-linear elastic moduli of the hexagonal HMS beam network under each mode of the mechanical stress in combination with the magnetic field. Despite of the opposite curvatures at the deformed state, the same tip-deflections of HMS beam for the two opposite distributions of $S(\xi)$ varying from $S = -1$ to $S = 1$ and from $S = 1$ to $S = -1$ is the cause behind such phenomenon. Such a phenomenon is already described in connection with Figs. 7 and S6 for a HMS beam with the opposite signs of $S(\xi)$ in the two halves. Hence, for the two opposite distributions (varying from $S = -1$ to $S = 1$ and from $S = 1$ to $S = -1$) of the second set of designed $S(\xi)$ as shown in Fig. 13(c) and (d), we get single set of results. Effects of the degree on non-linearity n for the second set of designed $S(\xi)$ on the non-linear elastic moduli of the hexagonal HMS beam network under the loading combinations of σ_1, σ_2, and τ with the magnetic field B^a are shown in Figures S15–S17 respectively for the magnetic load ratio $r_i = 2.5$, $r_i = 4$, and $r_i = 4$.

Under the compressive mode of normal stress along direction-1 (σ_1) in combination with the external magnetic field B^a for the second set of designed $S(\xi)$, the non-dimensional Young's modulus $\bar{E}_1$ initially decreases with the input stress magnitude σ_1 as observed from Figure S15(a). At the higher magnitude of the applied stress σ_1, $\bar{E}_1$ increases with σ_1 for the lower values of n and goes on decreasing for the higher values of n. Under the same combination of mechanical and magnetic loading, the Poisson's ratio ν_{12} decreases with the applied stress σ_1 as evident from Figure S15(c). Negative Poisson's ratio is obtained for $n = 0$, and 0.1 even for the non-auxetic configuration of the hexagonal HMS beam network under consideration. Under the tensile mode of the normal stress σ_1 in combination with B^a as observed from Figure S15(b) and (d), both Young's modulus $\bar{E}_1$ and Poisson's ratio ν_{12} increase with an increase in the magnitude of the applied stress σ_1. The overall non-linear Young's modulus $\bar{E}_1$ decreases with the degree of non-linearity n of the second set of designed $S(\xi)$ under both the compressive and tensile modes of σ_1 as observed from Figure S15(a) and (b). The maximum reductions in $\bar{E}_1$ for $n = 3$ compared to $n = 0$ are observed to be 86.9% and 63.9% under the compression and tension respectively. As observed in Figure S15(c), the Poisson's ratio ν_{12} has an increasing trend with n at the lower range of the compressive stress σ_1. However, at the higher range of σ_1, some mixed trend is observed. The maximum enhancement of 143.5% in ν_{12} for $n = 3$ compared to

$n = 0$ is achieved. Whereas, under the tensile mode of σ_1, Poisson's ratio ν_{12} decreases with n as shown in Figure S15(d), and the maximum reduction in ν_{12} is found to be 73.9%.

As shown in Figure S16(a) and (c), the non-dimensional Young's modulus $\bar{E}_2$ and Poisson's ratio ν_{21} of the hexagonal HMS beam network with the second set of designed $S(\xi)$ decrease with the applied stress input under the combined loading condition of compressive normal stress along direction-2 (σ_2) and magnetic field along direction-2 (B^a). The Overall non-linear elastic moduli $\bar{E}_2$ and ν_{21} increase with the degree of non-linearity n. The maximum enhancements in the elastic moduli $\bar{E}_2$ and ν_{21} for the non-linear $S(\xi)$ with $n = 3$ with respect to the linear $S(\xi)$ with $n = 0$ are found to be 23% and 68.5% respectively. Effects of the inherent system non-linearity and the degree of non-linearity n of the second set of designed $S(\xi)$ on the elastic moduli $\bar{E}_2$ and ν_{21} are found exactly the opposite under the tensile mode of normal stress σ_2 as observed from Figure S16(b) and (d) compared to the compressive mode (refer to Figure S16(a) and (c)). The maximum reductions of 63.3% and 35.8% are obtained in the elastic moduli $\bar{E}_2$ and ν_{21} for the non-linear $S(\xi)$ with $n = 3$ compared to the linear $S(\xi)$ with $n = 0$.

Under both the anti-clockwise and clockwise modes of shear stress τ in combination with the external magnetic field B^a, the non-dimensional effective shear modulus $\bar{G}_{12}$ of the hexagonal HMS beam network with the second set of designed $S(\xi)$ initially decreases and then increases with the input stress τ for the lower values of n as observed from Figure S17(a) and (b). Whereas, for the highest value of the degree of non-linearity $n = 3$, $\bar{G}_{12}$ has an increasing trend with the magnitude of the input stress τ. The plots in Figure S17(a) and (b) also depict that the non-linear shear modulus $\bar{G}_{12}$ increases with the degree of non-linearity n of the second set of deigned $S(\xi)$. The maximum enhancements in the non-dimensional shear modulus $\bar{G}_{12}$ are achieved to be 68.9% and 57.5% for the non-linear $S(\xi)$ with $n = 3$ compared to the linear $S(\xi)$ with $n = 0$ under the anti-clockwise and clockwise mode of shear stress respectively.

The numerical results presented in the preceding subsection (Section 3.4) demonstrate on-demand magneto-active modulations (enhancements and reductions) of the effective nonlinear elasticity of hexagonal HMS beam networks through uniform residual magnetic flux density design in the cell walls under far-field magnetic field in combination with externally applied mechanical stresses. Physics-informed (finite moments at the ends with zero moment at the mid-point due to the typical rotationally restrained beam boundary conditions for periodic lattices) architecturing of the residual magnetic flux density pattern in the cell walls as proposed in the present subsection results further augmentations in the deformation components due to far-field magnetic field compared to uniform residual magnetic flux density which are in-phase or out-of-phase with the deformations caused by mechanical stresses only. The in-phase and out-of-phase deformations coming from magnetic field and mechanical stresses respectively results augmented anti-curvature or pro-curvature effects (Ghuku and Mukhopadhyay, 2022a; Prajwal et al., 2022) to the cell wall deformations compared to the uniform residual magnetic flux density of the cell walls. Such active anti-curvature or pro-curvature effects cause further enhancements or reductions of the HMS beam network stiffness compared to the uniform residual magnetic flux density design as demonstrated through the numerical results in the present subsection (Section 3.5). In turn this will lead to improved energy efficiency in achieving a target on-demand stiffness, resulting in sustainable programmable metamaterials with minimum utilization of the intrinsic materials.

3.6. Applicability to other forms of periodic HMS beam networks

Within the developed multi-physical mechanics-based semi-analytical framework, modulations of the elastic moduli of hexagonal HMS beam networks with uniform and two intuitively designed residual magnetic flux densities are extensively investigated in the preceding two subsections. To demonstrate the generality of the proposed concept of modulating elastic properties through an external magnetic field within the developed physically insightful computational framework, non-linear effective elastic moduli of five other forms of HMS beam networks, namely, auxetic, rectangular brick, rhombic, triangular, and rectangular networks as shown in Fig. 1(g) are analysed in this subsection considering uniform residual magnetic flux density in combination with different modes of far-field mechanical stresses. Note that the concept of beam-level architecturing the residual magnetic flux density can also be implemented to different other unit cell architectures for more accentuated elasticity modulation as demonstrated in the case of hexagonal lattices (refer to Section 3.5). However, we limit the current demonstration to uniform residual magnetic flux density for other lattices in order to maintain the brevity of this paper.

3.6.1. Auxetic HMS beam networks

For the auxetic HMS beam network, as shown in Fig. 1(g)I, the geometric parameters are considered as $h/l = 2$ and $\theta = -\pi/6$. The unit cell configuration of the auxetic HMS beam network with residual magnetic flux density $S = 1$ subjected to normal (σ_1 or σ_2) and shear (τ) stresses in combination with the external magnetic field B^a is shown in Fig. 16(a). Variations of the non-dimensional elastic moduli $\bar{E}_1$, ν_{12}, $\bar{E}_2$, ν_{21}, and $\bar{G}_{12}$ with different modes of input stress magnitude under different magnetic load levels are presented in Fig. 16(b)–(f) respectively. It is evident from the figure that within a small deformation regime in absence of the external magnetic field, all the results obtained from the present framework agree well with the analytical solutions from literature (Gibson and Ashby, 1999). This provides a degree of confidence and validation to the present computational framework before exploiting it for further investigation.

As observed from Fig. 16(b), the effective non-dimensional Young's modulus $\bar{E}_1$ of the auxetic HMS beam network decreases with compressive stress σ_1 and magnetic load ratio r_i. Whereas, under the tensile mode of the normal stress σ_1, Young's modulus $\bar{E}_1$ increases with the stress magnitude and the magnetic load ratio r_i for $0 \leq r_i \leq 0.4$. Under the same loading condition for the magnetic load ratio $1 \leq r_i \leq 2$, negative stiffness is observed which decreases with stress magnitude but increases with r_i. Maximum 201.9% enhancement and 46.4% reduction in the positive Young's modulus $\bar{E}_1$ are achieved concerning the only mechanical loading condition ($r_i = 0$). Whereas, the maximum enhancement in the negative Young's modulus $\bar{E}_1$ is obtained as 68.8% for $r_i = 2$ compared to $r_i = 1$. Fig. 16(c) depicts that the effective Poisson's ratio ν_{12} increases with magnetic load ratio r_i with different degrees of auxecity under the compressive and tensile modes of normal stress σ_1. A maximum 19% enhancement in ν_{12} for the considered ranges of r_i can be obtained from Fig. 16(c).

For the combined loading under normal stress σ_2 and magnetic field B^a along direction-2 as presented in Fig. 16(d) and (e), effects of non-linearity in terms of variations of the elastic moduli $\bar{E}_2$ and ν_{21} with stress magnitude are found opposite compared to the loading combination under σ_1 and B^a. However, decreasing and increasing effects of the magnetic loading under the compressive and tensile loading modes are the same for $\bar{E}_2$ as that of $\bar{E}_1$, with maximum 400.4% and 66.49% enhancement and reduction respectively. However, for ν_{21}, the effect of magnetic load ratio is found opposite to that of ν_{12} with a maximum 40% reduction. Notably the degree of auxeticity for ν_{12} and ν_{21} can be actively controlled in a wide band as a function of the magnetic field.

As obvious from Fig. 16(f), under the anti-clockwise mode of shear loading, the non-dimensional shear modulus $\bar{G}_{12}$ increases with stress magnitude τ and decreases with magnetic load r_i. Under the clockwise mode of shear loading, $\bar{G}_{12}$ increases with stress magnitude τ for a lower range of r_i. However, for a higher range of r_i under the clockwise loading, negative $\bar{G}_{12}$ are observed having mixed increasing–decreasing

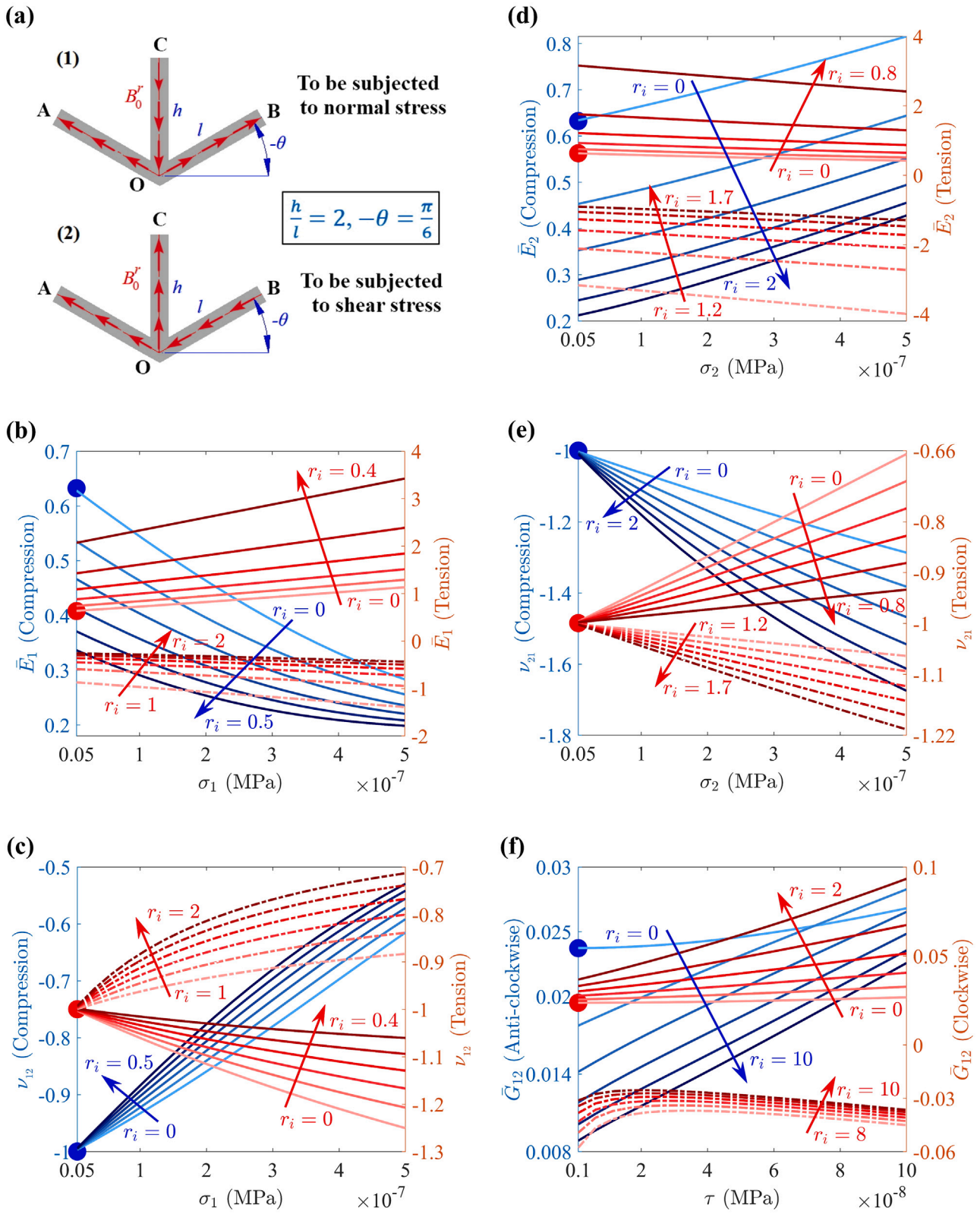

Fig. 16. Modulation of the effective elastic moduli of auxetic HMS beam networks having uniform residual magnetic flux density under different modes of mechanical stress in combination with magnetic field. (a) The unit cell of auxetic HMS beam network with $h/l = 2$ and $\theta = -\pi/6$ having residual magnetic flux density $S = 1$ subjected to (1) normal stress σ_1 or σ_2, and (2) shear stress τ in combination with magnetic field B^a along direction-2. **(b–f)** Variations of the non-dimensional effective elastic moduli of the auxetic HMS beam network as function of the different modes of the mechanical stress at equally spaced magnetic load levels r_i. The dotted points represent the analytical solutions (Gibson and Ashby, 1999) without magnetic field under small deformation regime.

trends with the stress magnitude. However, for both the ranges of r_i under the clockwise loading mode, r_i has increasing effects on $\bar{G}_{12}$. The maximum enhancement and reduction in the positive non-dimensional $\bar{G}_{12}$ concerning the only mechanical loading condition $r_i = 0$ are observed as 248.3% and 62.7% respectively. Whereas, in the negative shear modulus $\bar{G}_{12}$, a maximum 46% enhancement is achieved for $r_i = 10$ compared to $r_i = 8$.

3.6.2. Rectangular brick HMS beam networks

The rectangular brick HMS beam network as shown in Fig. 1(g)II is derived readily from the hexagonal HMS beam network by taking $\theta = 0$. The unit cell configuration of the rectangular brick HMS beam network with $h/l = 1$ having uniform residual magnetic flux density ($S = 1$) is shown schematically in Fig. 17(a). Variations of the non-dimensional effective elastic moduli $\bar{E}_1$, ν_{12}, $\bar{E}_2$, ν_{21}, and $\bar{G}_{12}$ of the rectangular brick HMS beam network as functions of the different modes of normal and shear stresses combined with external magnetic field are presented in Fig. 17(b)–(f). Comparisons of each set of results with the corresponding analytical solutions from literature (Gibson and Ashby, 1999), as presented through the large dotted points in the plots, validate our framework for the special case in absence of the magnetic field within a small deformation regime. This provides a degree of confidence to the present computational framework before exploiting it for further investigation.

As in cases of the other HMS beam networks, modulations of the non-linear elastic moduli of the rectangular brick HMS beam network in terms of the external magnetic field are evident from Fig. 17(b)–(f). Effects of geometric and material non-linearity on the elastic moduli in terms of their variations with stress magnitude σ_1, σ_2 or τ and magnetic load ratio r_i can be readily noticed Fig. 17(b)–(f). Interestingly, from Fig. 17(b)–(f) it becomes obvious that depending on the combination of the magnetic load with a particular mode of the mechanical stress, negative Young's modulus, negative Poisson's ratio and negative shear modulus can be achieved. Maximum enhancements in $\bar{E}_1$, $\bar{E}_2$, and $\bar{G}_{12}$ are noted to be 64.4%, 150%, and 162.1% respectively. Whereas, maximum 32%, 54.5%, 91.7%, and 48.5% reductions in $\bar{E}_1$, $\bar{E}_2$, ν_{21}, and $\bar{G}_{12}$ are obtained respectively under the considered ranges of the magnetic load ratio r_i.

Note in Fig. 17(c) that under the combined loading of normal stress σ_1 and magnetic field B^a, the magnitudes of the negative or positive Poisson's ratio ν_{12} of the rectangular brick HMS beam network are very large compared to the unity. As obvious from Fig. 17(a-1), under the combined loading of normal stress σ_1 and magnetic field B^a, the normal strain in direction-2 (ϵ_2) is governed by the bending-dominated deformation of the horizontal cell walls. Whereas, the normal strain along direction-1 (ϵ_1) is governed by the stretching-dominated deformation of the horizontal cell walls. Due to the difference in the order of magnitudes of the bending and stretching dominated axial strains along direction-1 (ϵ_1) and direction-2 (ϵ_2), such large magnitudes of Poisson's ratio ν_{12} is achieved for the rectangular brick HMS beam network under the present loading combination. As ν_{12} is zero under the only mechanical load in absence of the magnetic field, the enhancement and reduction in it are noted in terms of their absolute values instead of percentage and they are 240.4 and 109.3 respectively.

3.6.3. Rhombic HMS beam networks

The rhombic HMS beam network as shown in Fig. 1(g)III is obtained from generic hexagonal HMS beam lattices by putting $h/l = 0$ and $\theta = \pi/4$. The unit cell configuration of the rhombic HMS beam network with uniform residual magnetic flux density ($S = 1$) is shown in Fig. 18(a). Variations of the non-dimensional effective elastic moduli $\bar{E}_1$, ν_{12}, $\bar{E}_2$, ν_{21}, and $\bar{G}_{12}$ of the rhombic HMS beam network with combined stress and external magnetic field along with the comparisons with the respective analytical results from literature (Gibson and Ashby, 1999) are shown in Fig. 18(b)–(f). The good agreement with literature provides a degree of confidence and validation to the present computational framework before exploiting it for further investigation.

The self-explanatory plots in Fig. 18(b)–(f) establish the idea of modulating the non-linear elastic moduli $\bar{E}_1$, ν_{12}, $\bar{E}_2$, ν_{21}, and $\bar{G}_{12}$ of the rhombic HMS beam network by external magnetic field in combination with the different modes of the mechanical stress. The figure also depicts that under certain combinations of mechanical and magnetic loads, negative stiffness of the rhombic network can be achieved. Maximum 233%, 36.8%, 232.7%, and 77.6% enhancements in the non-dimensional elastic moduli $\bar{E}_1$, ν_{12}, $\bar{E}_2$, and $\bar{G}_{12}$ of the rhombic HMS beam network are obtained respectively under the considered ranges of the magnetic loads. Whereas, the maximum reductions in the non-dimensional elastic moduli $\bar{E}_1$, $\bar{E}_2$, ν_{21}, and $\bar{G}_{12}$ are achieved to be 58%, 60.2%, 37%, and 36.6% respectively.

3.6.4. Triangular HMS beam networks

The non-linear elastic moduli of the triangular HMS beam network (refer to Fig. 1(g)IV) is not readily derivable from the multi-physical mechanics-based semi-analytical framework for the hexagonal HMS beam lattices. However, by selecting the proper unit cell as shown in Fig. 19(a), the effective elastic moduli of the triangular HMS beam network are derived following a similar computational framework. A detailed derivation of non-linear elastic moduli E_1, ν_{12}, E_2, ν_{21}, and G_{12} of the triangular HMS beam network under the combined mechanical stress and magnetic field is presented in Section 2.4.

Variations of the non-dimensional elastic moduli $\bar{E}_1$, ν_{12}, $\bar{E}_2$, ν_{21}, and $\bar{G}_{12}$ of the triangular HMS beam network with different modes of mechanical stress in combination with the magnetic field are shown in Fig. 19(b)–(f). The corresponding analytical results from literature (Gibson and Ashby, 1999; Wang and McDowell, 2004) in absence of the magnetic field within a small deformation regime are also plotted in the figure through the large dotted points. The comparison studies successfully validate our proposed semi-analytical framework for the special case of small deformation in absence of the magnetic field.

Fig. 19(b)–(f) depicts that the non-linear non-dimensional elastic moduli $\bar{E}_1$, ν_{12}, $\bar{E}_2$, ν_{21}, and $\bar{G}_{12}$ of the triangular HMS beam network can be modulated as per requirement through the magnetic load in terms of ratio r_h or r_i. Under certain combinations of mechanical stress with the magnetic field, even a negative Poisson's ratio is achievable with different degrees. The maximum enhancements in the non-dimensional elastic moduli $\bar{E}_1$, ν_{12}, $\bar{E}_2$, ν_{21}, and $\bar{G}_{12}$ of the triangular HMS beam network are attainable as 14.1%, 27.5%, 44.5%, 865.5%, and 154% respectively. Whereas, maximum 11.6%, 27.6%, 32%, 1523.5%, and 65.8% reductions in the non-dimensional elastic moduli are obtained respectively.

Note the exceptional enhancement (865.5%) and reduction (1523.5%) in the Poisson's ratio ν_{21} as observed from Fig. 19(e). As obvious from Fig. 19(a-1), under the combined loading of normal stress σ_2 and magnetic field B^a, the influence of bending due to the magnetic field is more on the horizontal member OA compared to the inclined member OB. Such a deformation pattern of the triangular HMS unit cell creates a difference in the order of magnitudes of the normal strains along direction-1 (ϵ_1) and direction-2 (ϵ_2) which in turn results in an exceptionally large enhancement and reduction in the Poisson's ratio ν_{21} as noted in the numerical results.

3.6.5. Rectangular HMS beam networks

As in the case of the triangular HMS beam network, derivation of the non-linear elastic moduli of the rectangular HMS beam network (refer to Fig. 1(g)V) by considering appropriate unit cell (refer to Fig. 20(a)) within the current semi-analytical framework is presented in Section 2.5. Variations of the non-dimensional elastic moduli $\bar{E}_1$, ν_{12}, $\bar{E}_2$, ν_{21}, and $\bar{G}_{12}$ of the rectangular HMS beam network with different modes of mechanical stress in combination with the magnetic field along with the comparisons with the respective analytical results (concerning only small deformation mechanical stresses) from literature (Gibson and Ashby, 1999; Wang and McDowell, 2004) are presented in Fig. 20(b)–(f). As in the case of the other configurations,

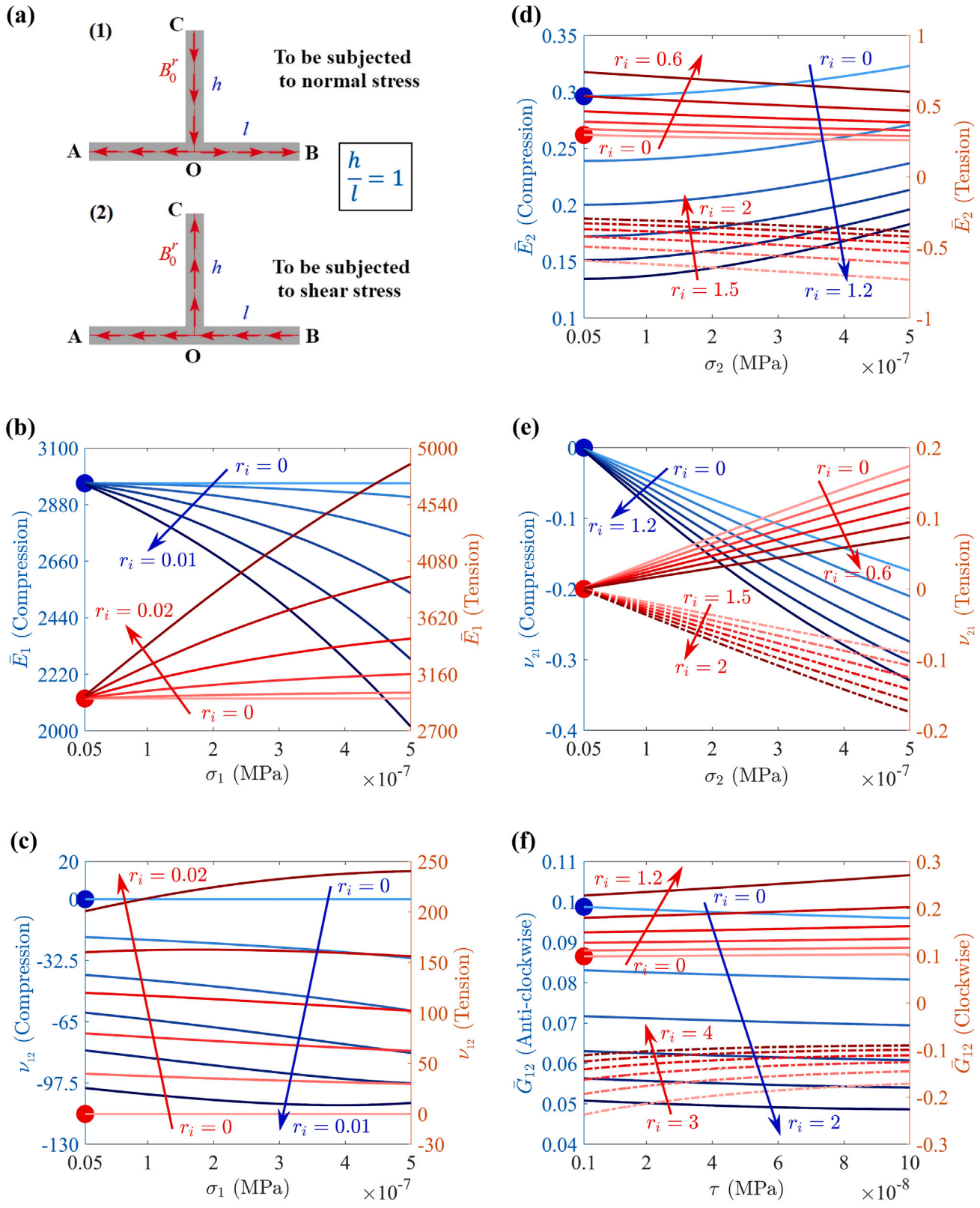

Fig. 17. Modulation of the effective elastic moduli of rectangular brick HMS beam networks having uniform residual magnetic flux density under different modes of mechanical stress in combination with magnetic field. (a) The unit cell of rectangular brick HMS beam network with $h/l = 1$ having residual magnetic flux density $S = 1$ subjected to (1) normal stress σ_1 or σ_2, and (2) shear stress τ in combination with magnetic field B^a along direction-2. **(b–f)** Variations of the non-dimensional effective elastic moduli of the rectangular brick HMS beam network as function of different modes of the mechanical stress at equally spaced magnetic load levels r_i. The dotted points represent the analytical solutions (Gibson and Ashby, 1999) without magnetic field under small deformation regime.

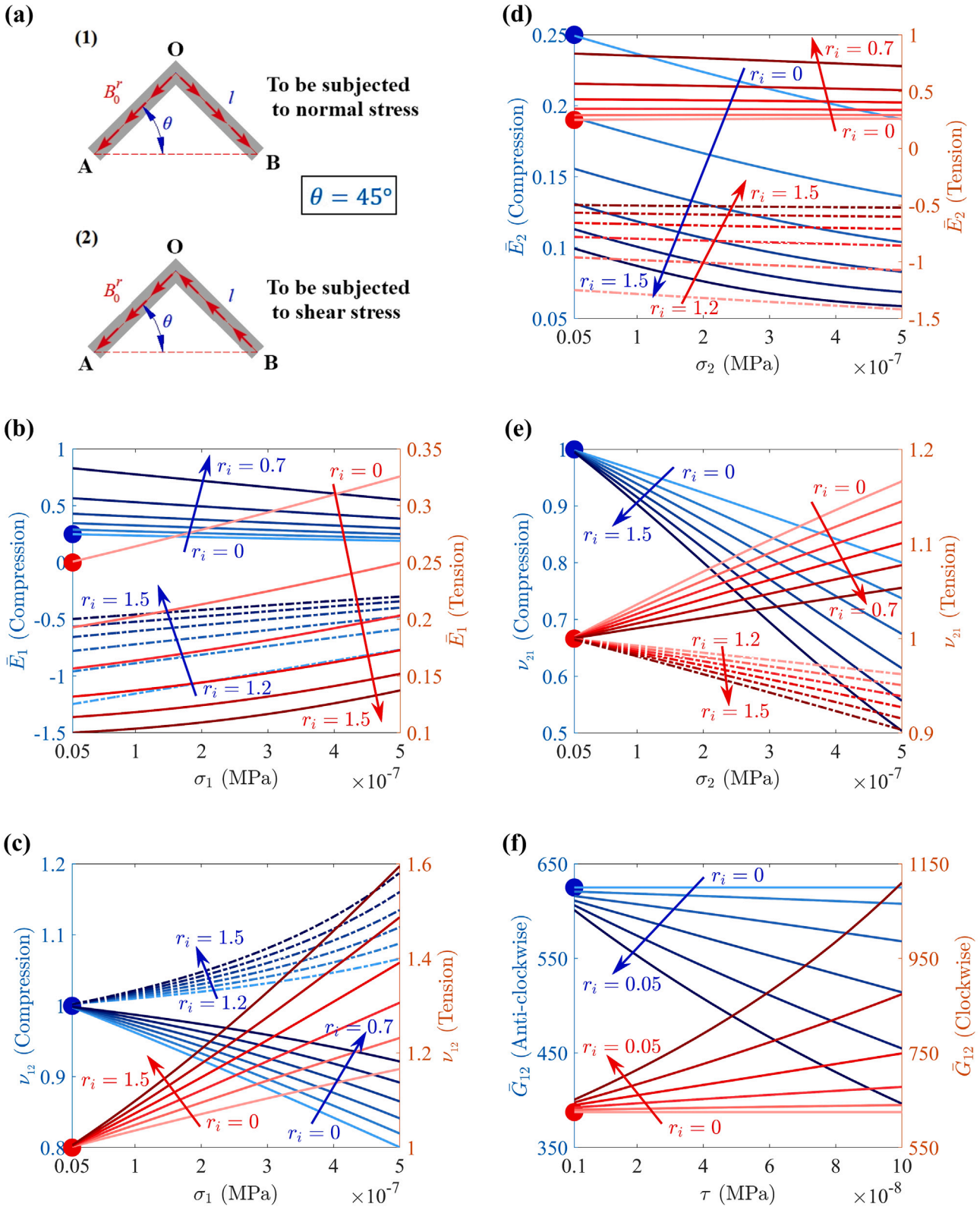

Fig. 18. Modulation of the effective elastic moduli of rhombic HMS beam networks having uniform residual magnetic flux density under different modes of mechanical stress in combination with magnetic field. (a) The unit cell of rhombic HMS beam network with $\theta = \pi/4$ having residual magnetic flux density $S = 1$ subjected to (1) normal stress σ_1 or σ_2, and (2) shear stress τ in combination with magnetic field B^a along direction-2. **(b–f)** Variations of the non-dimensional effective elastic moduli of the rhombic HMS beam network as function of the different modes of the mechanical stress at equally spaced magnetic load levels r_i. The dotted points represent the analytical solutions (Gibson and Ashby, 1999) without magnetic field under small deformation regime.

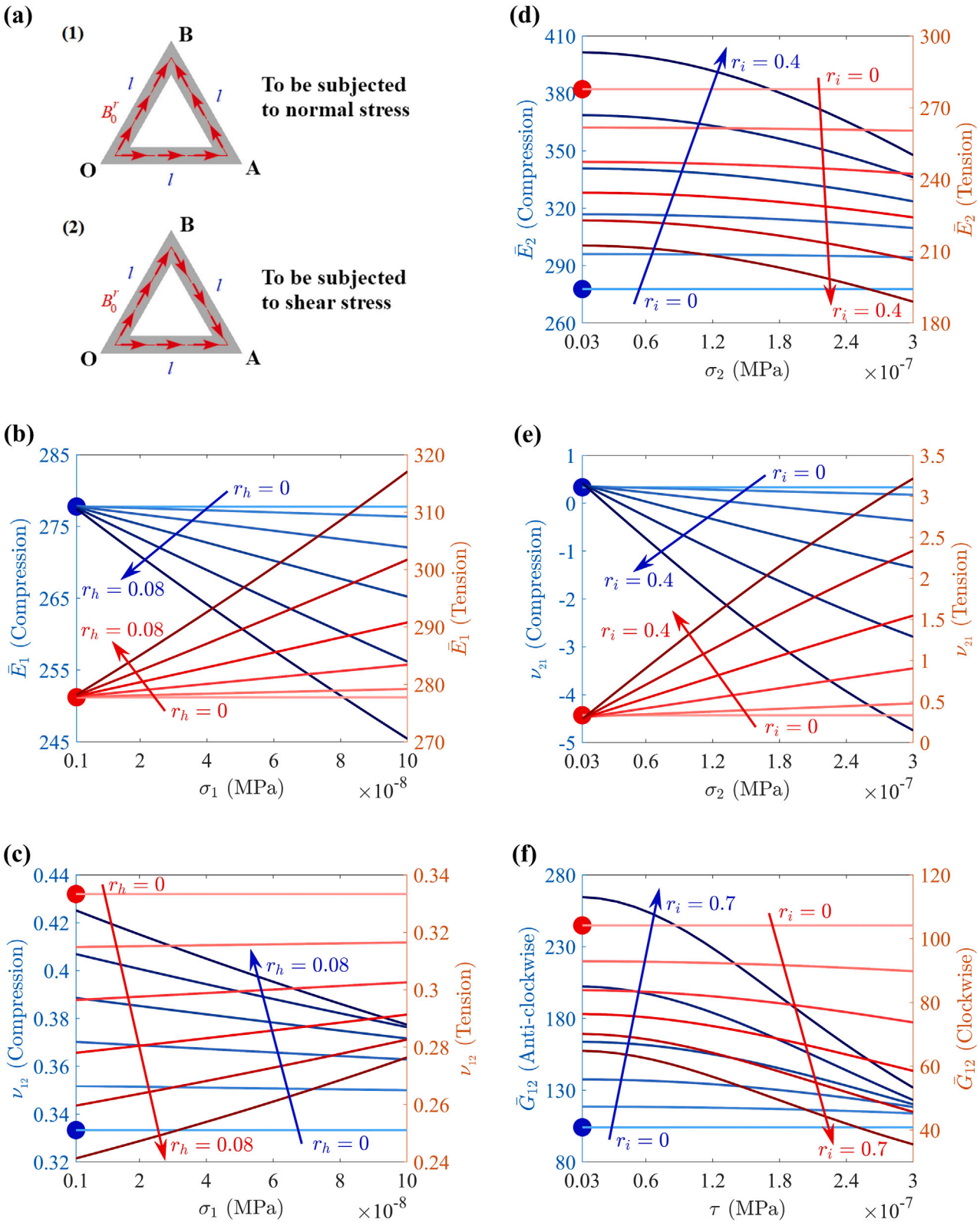

Fig. 19. Modulation of the effective elastic moduli of triangular HMS beam networks having uniform residual magnetic flux density under different modes of mechanical stress in combination with magnetic field. (a) The unit cell of triangular HMS beam network having residual magnetic flux density $S = 1$ subjected to (1) normal stress σ_1 or σ_2, and (2) shear stress τ in combination with magnetic field B^a along direction-2. **(b–f)** Variations of non-dimensional effective elastic moduli of the triangular HMS beam network as function of the different modes of the mechanical stress at equally spaced magnetic load levels r_h or r_i. The dotted points represent the analytical solutions (Gibson and Ashby, 1999; Wang and McDowell, 2004) without magnetic field under small deformation regime.

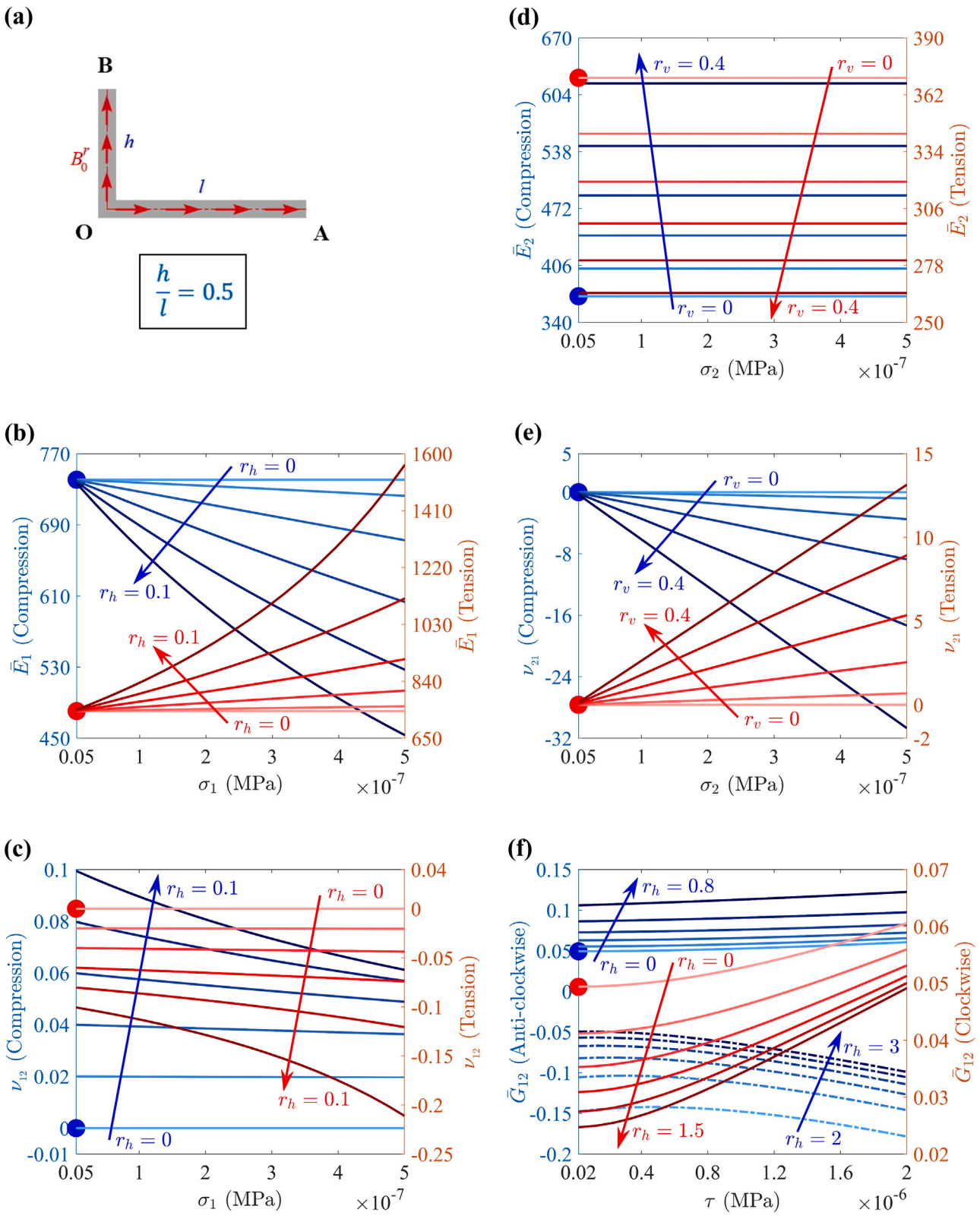

Fig. 20. Modulation of the effective elastic moduli of rectangular HMS beam networks having uniform residual magnetic flux density under different modes of mechanical stress in combination with magnetic field. (a) The unit cell of rectangular HMS beam network with $h/l = 0.5$ having residual magnetic flux density $S = 1$ subjected to normal stress σ_1 or σ_2 and shear stress τ in combination with magnetic field B^a along direction-2. **(b–f)** Variations of non-dimensional effective elastic moduli of the rectangular HMS beam network as function of different modes of the mechanical stress at equally spaced magnetic load levels r_h or r_v. The dotted points represent the analytical solutions (Gibson and Ashby, 1999; Wang and McDowell, 2004) without magnetic field under small deformation regime.

the comparison studies between the present semi-analytical framework and the analytical models (Gibson and Ashby, 1999; Wang and McDowell, 2004) are found quite satisfactory in absence of the magnetic field within the small deformation regime.

The concept of modulating non-linear elastic moduli $\bar{E}_1$, ν_{12}, $\bar{E}_2$, ν_{21}, and $\bar{G}_{12}$ through applying an external magnetic field is demonstrated in Fig. 20(b)–(f) for the rectangular HMS beam network. The figure also depicts that by controlling the external magnetic field in combination with the mechanical load, mode-dependent negative Poisson's ratio and negative shear modulus can be achieved. Maximum 111.1%, 66.7%, and 102.1% enhancements in the non-dimensional elastic moduli $\bar{E}_1$, $\bar{E}_2$, and $\bar{G}_{12}$ are obtained respectively. Whereas, the maximum reductions in the elastic moduli are found to be 38.8%, 28.6%, and 50% respectively. As the Poisson's ratios ν_{12} and ν_{21} are zero under only mechanical load, their enhancements and reductions under magnetic field are expressed by absolute values instead of percentage values, and they are 0.1 and 13.1 in enhancement and 0.2 and 30.7 in reduction respectively. The large magnitudes of the positive and negative Poisson's ratio ν_{21} of the rectangular HMS beam network are caused by the difference in the order of magnitudes in the normal strains ϵ_1 and ϵ_2 under the combined loading of normal stress σ_2 and magnetic field B^a due to different respective modes of predominant beam deformations.

In general, the numerical results demonstrate the on-demand active modulation of effective elastic moduli in a wide band (i.e. broadband stiffness and flexibility programming) as a function of the unit cell geometry, beam-level architecture of residual magnetic flux density and nonlinear intrinsic material properties along with the applied far-field mechanical stresses and magnetic field. The effectiveness of applied magnetic field can be further optimized (including target attainment) corresponding to a particular mode and level of applied far-field stress depending on the unit cell geometry (such as different bending and stretching dominated unit cells and dimensions of the beam-like members) and beam-level residual magnetic flux density.

4. Summary and perspective

In the paper, we have proposed a novel class of lattice metamaterials as periodic networks of beams made of soft material with embedded hard magnetic particles (HMS beam networks) subjected to large deformation under combined remote mechanical stress and magnetic field. The architected networks of HMS beams are very light in weight and provide excellent modulation capability of the nonlinear effective elastic properties depending on the hard magnetic particle distribution in the HMS beam elements, unit cell geometry and the combination of applied mechanical stress with the external magnetic field. To actively modulate the metamaterial properties post-manufacturing enabling applications for a range of advanced intelligent structural systems, we propose here to adopt an innovative bi-level modulation concept involving the coupled design space of unit cell geometries, architected HMS beam-like members and their stimuli–responsive deformation physics. We have exploited the geometric non-linearity due to large deformation and material non-linearity under magneto-mechanical coupling to modulate the effective elastic properties of the novel class of architected HMS beam networks ranging from very high stiffness like stiff metal to very low stiffness, even lower compared to the soft polymers.

By externally applying different values of the magnetic field intensity, different elastic properties and stiffness can be achieved, and that too from a distance (i.e. on-demand contactless elasticity control). Essentially, this will help in minimizing the material utilization to an extreme extent by controlling the stiffness of a structure based on active operational demands. For example, the stiffness corresponding to target modes and direction of a structure can be actively increased during an operational condition when higher magnitudes of loads are experienced to keep the deformations under control or the natural frequencies need to be increased to avoid resonance under dynamic loading. The stiffness can also be actively reduced to allow large deformation and shape control for (soft-)robotic motions or increased energy absorption and avert sudden failure.

To estimate the non-linear effective elastic moduli under the normal or shear mode of mechanical stress in combination with the external magnetic field, a physically insightful semi-analytical framework is developed for periodic HMS beam networks. Within the unit cell-based framework, the non-linear multi-physical mechanics of rotationally restrained HMS beams subjected to combined mechanical and magnetic loads representing generalized elements of the architected beam network is defined. Governing equation of the non-linear HMS beams is derived using the variational principle-based energy method within the non-linear kinematic setting of the Euler–Bernoulli beam theory and the material constitutive law of the Yeoh hyperelastic model. To deal with the non-linearity involved in the governing equation of the multi-physical mechanics problem, a successive two-stage iterative computational scheme is developed as an integral part of the semi-analytical framework.

Considering the aim of this paper, we have limited the scope to 2D lattices with different bending and stretching-dominated periodic configurations (as shown in Fig. 1(b, g)) to demonstrate the concept of post-manufacturing contactless active mechanical property modulation. Extension of the 2D lattice framework into 3D lattices can be readily performed by considering the same HMS beam model and appropriate 3D unit cells with appropriate boundary conditions (for example, refer to Sinha et al. (2025)).

Within the developed semi-analytical framework, we first investigate the effect of external magnetic field in combination with different modes of remote mechanical stress on the non-linear effective elastic moduli of the architected hexagonal HMS beam network having uniform residual magnetic flux density. Based on the observations along with the kinematics and kinetics of the HMS beam elements, we have proposed two physics-informed beam-level designs of residual magnetic flux density for the hexagonal HMS beam network, leading to enhanced efficiency of the magnetic field. Further to demonstrate the generality of the proposed multi-physical mechanics-based framework, different other HMS beam based lattice geometries, namely, auxetic, rectangular brick, rhombic, triangular, and rectangular configurations are investigated considering uniform residual magnetic flux density. Before presenting the numerical results, the developed semi-analytical framework has been thoroughly validated to ascertain adequate confidence, considering (1) HMS beam-level deformation under mechanical and magnetic actuation (note that the lattice-level homogenized mechanical behaviour depends on beam-level deformation physics), (2) effective elastic moduli of different lattice geometries considering the conventional linear regime, and (3) effective nonlinear elastic moduli of hexagonal lattices under large deformation. Such multi-level validations at the beam and lattice level considering the linear and non-linear deformation regimes along with multi-physical loading conditions provide adequate confidence in the proposed computational framework. A full-scale finite element modelling can be carried out to compare the current results. But considering the complexity of modelling such HMS beam-based lattices in the finite element framework, it is beyond the scope of this manuscript. Further, a detailed finite element model of the lattice is also not strictly necessary considering the extensive multi-level validation approach adopted for the proposed computational framework.

For the hexagonal HMS beam network with the uniform residual magnetic flux density, the maximum enhancements in the non-dimensional elastic moduli $\bar{E}_1$, ν_{12}, $\bar{E}_2$, ν_{21}, and $\bar{G}_{12}$ under the compressive normal modes and anti-clockwise shear mode of the mechanical stress in combination with the magnetic field are achieved as 225.5%, 232.8%, 233.7%, 35.1%, and 339.6% respectively compared to the only mechanical loading condition without any magnetic field. Under the same combined loading conditions, the maximum reductions in the five elastic moduli are observed to be 84%, 29.8%, 83.9%, 129.4%,

and 56.8% respectively. Whereas, under the tensile modes of normal stress and the clockwise mode of shear stress in combination with the magnetic field, 189.1%, 449.2%, 232.6%, 55%, and 463.4% enhancements and 72.1%, 21.9%, 83.1%, 39%, and 68.4% reductions in the five elastic moduli $\bar{E}_1$, ν_{12}, $\bar{E}_2$, ν_{21}, and $\bar{G}_{12}$ are achieved respectively.

The effectiveness of on-demand elasticity modulation can further be enhanced through beam-level spatially-varying architectures of the residual magnetic flux density. For the hexagonal HMS beam network with the first set of designed residual magnetic flux density, 56%, 11%, 42.4%, 27.5%, and 50.9% enhancements in the non-dimensional elastic moduli $\bar{E}_1$, ν_{12}, $\bar{E}_2$, ν_{21}, and $\bar{G}_{12}$ are achieved respectively compared to the uniform magnetization under the compressive modes of normal stress and anti-clockwise mode of shear stress in combination with the external magnetic field. Whereas, the maximum reductions in the non-dimensional elastic moduli $\bar{E}_1$, ν_{12}, $\bar{E}_2$, ν_{21}, and $\bar{G}_{12}$ under the compressive normal modes and the anti-clockwise shear mode of the mechanical stress in combination with the magnetic field are found to be 66.4%, 21%, 47.2%, 18%, and 35.6% respectively. Under the tensile modes of the normal stress and the clockwise mode of shear stress in combination with the external magnetic field, 31.1%, 22.7%, 41%, 10.4%, and 104.3% enhancements and 62.6%, 23.3%, 46.6%, 7.3%, and 80.4% reductions in the five elastic moduli $\bar{E}_1$, ν_{12}, $\bar{E}_2$, ν_{21}, and $\bar{G}_{12}$ of the hexagonal HMS beam network with the first designed set of residual magnetic flux density are obtained respectively.

For the hexagonal HMS beam network with the second set of design (beam-level spatial variation) of the residual magnetic flux density under the compressive modes of normal stress and the anti-clockwise mode of shear stress in combination with the magnetic field, maximum 86.9% reduction in $\bar{E}_1$ and maximum 143.5%, 23%, 68.5%, and 68.9% enhancements in ν_{12}, $\bar{E}_2$, ν_{21}, and $\bar{G}_{12}$ are achieved respectively with respect to uniform designs. Whereas, under the tensile normal modes and the clockwise shear mode of the mechanical stress in combination with the magnetic field, maximum 63.9%, 73.9%, 63.3%, and 35.8% reductions in $\bar{E}_1$, ν_{12}, $\bar{E}_2$, and ν_{21} and maximum 57.5% enhancement in $\bar{G}_{12}$ are achieved respectively. It is worthy to mention that we have explored here two different classes of architectures for spatially varying residual flux density, while there exist a vast scope of further optimization following single and multi-objective optimization algorithms along with unit cell geometry for enhancing the effectiveness of broad-band elasticity modulation.

For the auxetic HMS beam network with the uniform residual magnetic flux density, the maximum enhancements in the non-dimensional elastic moduli $\bar{E}_1$, ν_{12}, $\bar{E}_2$, and $\bar{G}_{12}$ are achieved to be 201.9%, 19%, 400.4%, and 248.3% respectively compared to the only mechanical loading condition. Whereas, maximum 46.4%, 66.49%, 40%, and 62.7% reductions are obtained in the non-dimensional elastic moduli $\bar{E}_1$, $\bar{E}_2$, ν_{21}, and $\bar{G}_{12}$ respectively. For the rectangular brick HMS beam network with the uniform residual magnetic flux density, maximum 64.4%, 150%, and 162.1% enhancements are achieved in $\bar{E}_1$, $\bar{E}_2$, and $\bar{G}_{12}$ respectively compared to the only mechanical loading condition. Whereas, the maximum reductions in $\bar{E}_1$, $\bar{E}_2$, ν_{21}, and $\bar{G}_{12}$ are obtained to be 32%, 54.5%, 91.7%, and 48.5% respectively. As ν_{12} is zero for rectangular brick lattices under the only mechanical load in absence of the magnetic field, the enhancement and reduction in it are noted in terms of their absolute values instead of percentage and they are 240.4 and 109.3 respectively.

For the rhombic HMS beam network with the uniform residual magnetic flux density, maximum 233%, 36.8%, 232.7%, and 77.6% enhancements in the non-dimensional elastic moduli $\bar{E}_1$, ν_{12}, $\bar{E}_2$, and $\bar{G}_{12}$ are obtained respectively compared to the only mechanical loading condition. Whereas, the maximum reductions in the non-dimensional elastic moduli $\bar{E}_1$, $\bar{E}_2$, ν_{21}, and $\bar{G}_{12}$ are achieved to be 58%, 60.2%, 37%, and 36.6% respectively. For the triangular HMS beam network with the uniform residual magnetic flux density, the maximum enhancements in non-dimensional elastic moduli $\bar{E}_1$, ν_{12}, $\bar{E}_2$, ν_{21}, and $\bar{G}_{12}$ are achieved to be 14.1%, 27.5%, 44.5%, 865.5%, and 154% respectively compared to the only mechanical loading condition in absence of magnetic field. Whereas, maximum 11.6%, 27.6%, 32%, 1523.5%, and 65.8% reductions in the non-dimensional elastic moduli are obtained respectively. For rectangular HMS beam network with the uniform residual magnetic flux density, maximum 111.1%, 66.7%, and 102.1% enhancements in the non-dimensional elastic moduli $\bar{E}_1$, $\bar{E}_2$, and $\bar{G}_{12}$ are obtained respectively compared to the only mechanical condition. Whereas, the maximum reductions in the elastic moduli are found to be 38.8%, 28.6%, and 50% respectively. As the Poisson's ratios ν_{12} and ν_{21} are zero for rectangular lattices under only mechanical load, their enhancements and reductions under magnetic field are expressed by absolute values instead of percentage values, and they are 0.1 and 13.1 in enhancement and 0.2 and 30.7 in reduction respectively.

The numerical investigations on the effective elastic moduli of the HMS beam networks depict an excellent modulation capability of the elastic properties in an extremely wide band for the proposed novel class of lightweight lattice metamaterials through designing the beam-level distribution of residual magnetic flux density, unit cell geometry and nonlinear coupled material physics, along with controlling the external magnetic field in combination with the mechanical mode of loading. The numerical results exhibit non-invariant elastic properties (Sinha et al., 2023) of the periodic HMS beam networks under the anti-clockwise and clockwise modes of shear stress in addition to the tensile and compressive modes of normal stress. Moreover, under certain combinations of the externally applied mechanical stress and magnetic field depending on the residual magnetic flux density, it is possible to achieve negative stiffness and negative Poisson's ratio with different degrees of auxecity, even for the non-auxetic unit cell configurations. The reported numerical results would provide a foundation for more innovative designs of the residual magnetic flux density of the HMS beam elements along with the interactive influence of unit cell geometry to increase the spectrum of modulated effective elastic properties.

In this paper, we have considered different modes of far-field in-plane mechanical stresses (normal stress along the horizontal and vertical direction (direction-1 and 2) and shear stress in plane 1–2) in combination with remote magnetic field along direction-2. It can be noted that there are three aspects of magnetic stimuli in the context of the proposed active metamaterials (1) distribution of residual magnetic flux density along the length of the constituting beams that form a unit cell, leading to beam-level magnetic particle distribution architecture, (2) direction of the externally applied magnetic field, and (3) intensity of externally applied magnetic field. In the analysis of the multi-physical large deformation mechanics of HMS beam representing the generalized member of periodic HMS beam networks under the combined mechanical and magnetic loading as presented in Sections 2.1 and 2.2, generalized direction (inclination angle α) of the externally applied magnetic field B^a is considered in combination with the generalized mechanical force. Hence, the multi-scale framework estimating the non-linear elastic properties of the proposed HMS metamaterials under the far-field mechanical and magnetic fields is generalized for considering any arbitrary direction of the external magnetic field in combination with the different modes of the in-plane mechanical stresses. Though we have concentrated on the remote magnetic field along direction-2 considering different intensities in combination with normal and shear modes of the in-plane mechanical stresses, the framework can easily be extended to consider other directions of magnetic fields. In fact, this will give a scope of achieving tunable normal-shear lattice level coupling behaviour for a given bi-level designed lattice architecture just by changing the direction of external magnetic field (Mondal et al., 2025). The effect of intensity of externally applied magnetic field is investigated throughout the presented results for multi-physical property modulation of lattices, while the beam-level architecture based on the distribution of residual magnetic flux density is explored in Section 3.5.

We would conclude this section by highlighting, summarizing and justifying some of the keywords and concepts of the presented research, as reflected in the discussions throughout this paper. (1) *Metamaterials*: The work deals with the development of a new class of mechanical metamaterials conceptualized as a periodic network of hard magnetic soft beams that can change their properties in real-time based on external stimuli. (2) *Magneto-active*: The proposed novel class of metamaterials under consideration is magneto-active because their mechanical properties can be actively altered by applying an external magnetic field. The title includes this term to signify the magneto-mechanical interaction that underpins the unique homogenized behaviour and active effective elastic moduli of these metamaterials. (3) *Nonlinear*: The metamaterials' homogenized constitutive response under the combined mechanical and magnetic fields is non-linear due to geometric non-linearity coming from the large deformation of the beam-like soft cell walls and material nonlinearity of the considered materials. (4) *Bi-level architected*: The paper introduces the concept of bi-level modulation of the effective elastic properties of the novel class of metamaterials under the far-field combined mechanical stress and magnetic stimuli, where the design incorporates both the unit cell periodic geometries, and the deformation physics of the beam-like members based on the hard magnetic particle distribution patterns within the soft cell walls. This term in the title refers to this dual-level design approach, integrating geometric and multi-physical aspects (both at unit cell level and beam level) to control the effective lattice-level material behaviour. (5) *Multi-physically programmable*: The paper discusses the ability to actively modulate the physical properties of metamaterials, such as elastic moduli and Poisson's ratios, through contactless far-field stimuli (magnetic field). This shows that the metamaterials can be programmed post-manufacturing to exhibit different mechanical behaviours depending on external stimuli as per application-specific operational demands. The term multi-physical highlights the fact that active on-demand elastic moduli tailoring is achieved here through different physics involving mechanical and magnetic deformations. (6) *stimuli–responsive*: The work emphasizes the stimuli–responsive nature of the metamaterials, where the mechanical properties change in response to external magnetic fields and mechanical stresses. This term reflects the adaptability of the metamaterials to different external stimuli, which is a key focus of the paper. (7) *Multi-scale mechanics*: The research focuses on the development of a multi-physical mechanics-based framework for the estimations and modulations of the homogenized mechanical properties of the proposed metamaterials considering geometric and material non-linearities due to large deformation and magneto-mechanical coupling. The developed computational framework involves the deformation mechanics of hard magnetic soft beams and subsequent integration of that in the unit cell mechanics to obtain the homogenized mechanical behaviour of the lattices. In essence, it may be noted that the computational mechanics framework developed here entails components and understanding at different length scales (i.e. multi-scale) to obtain the effective elastic properties: hard magnetic particles and their distribution at the beam level (i.e. beam-level architecture), unit cell geometry, effective material properties (i.e. the effective elastic moduli) at continuum level and subsequently design of structures (such as an aircraft) based on such continuum level effective elastic properties.

5. Conclusions

The current work addresses a critical limitation in conventional mechanical metamaterials in terms of contactless broad-band programming of elastic moduli based on on-demand operational requirements. This is achieved through shifting the design paradigm towards more innovative bi-level modulation concepts involving the coupled design space of unit cell geometries, architected beam-like members and their stimuli–responsive deformation physics. We have introduced graded hard magnetic soft (HMS) material architectures in the periodic beam networks following physics-informed insights of the stress resultants depending on uni cell geometry. The compound effect of spatially-graded residual magnetic flux density and unit cell geometries lead to improved stimuli efficiency in achieving a target on-demand stiffness, resulting in programmable and sustainable metamaterials with minimal utilization of the intrinsic materials. Moreover, under certain combinations of the externally applied mechanical stress and magnetic field depending on the residual magnetic flux density, it is possible to achieve negative stiffness and negative Poisson's ratio with different degrees of auxecity, even for the non-auxetic unit cell configurations. A generic semi-analytical computational framework involving the large-deformation geometric non-linearity and material non-linearity under magneto-mechanical coupling is developed here for the effective elastic moduli of HMS material based bi-level architected lattices under normal or shear modes of mechanical far-field stresses. Effective elastic moduli being a critically fundamental property of materials, the capability of having extreme-broadband active control would essentially lead to on-demand programming of a range of static, stability and dynamic structural behaviour, including direction-dependent deformation, vibration and control, wave propagation, impact and penetration resistance, energy absorption, shape morphing, robotic motion and actuation at multiple length scales.

CRediT authorship contribution statement

S. Ghuku: Writing – original draft, Visualization, Validation, Methodology, Investigation, Formal analysis. **S. Naskar:** Writing – original draft, Visualization, Investigation, Formal analysis. **T. Mukhopadhyay:** Writing – review & editing, Supervision, Investigation, Formal analysis, Conceptualization.

Declaration of competing interest

The authors declare that they have no known competing financial interests or personal relationships that could have appeared to influence the work reported in this paper.

Acknowledgements

TM and SN would like to acknowledge the initiation grant received from the University of Southampton during the period of this research work. SG acknowledges the funding of Science and Engineering Research Board (SERB) through Empowerment and Equity Opportunities for Excellence in Science (EMEQ - File No. EEQ/2023/000548).

Appendix A. Supplementary data

Supplementary material related to this article can be found online at https://doi.org/10.1016/j.mechmat.2025.105333.

Data availability

Data will be made available on request.

References

Adhikari, S., Mukhopadhyay, T., Liu, X., 2021. Broadband dynamic elastic moduli of honeycomb lattice materials: A generalized analytical approach. Mech. Mater. 157, 103796.

Alkuino, G., Zhang, T., 2024. Physics-based discrete models for magneto-mechanical metamaterials. J. Mech. Phys. Solids 191, 105759.

Balawi, S., Abot, J., 2008. The effect of honeycomb relative density on its effective in-plane elastic moduli: An experimental study. Compos. Struct. 84 (4), 293–299.

Bandyopadhyay, A., Heer, B., 2018. Additive manufacturing of multi-material structures. Mater. Sci. Eng.: R: Rep. 129, 1–16.

Bartlett, N.W., Tolley, M.T., Overvelde, J.T., Weaver, J.C., Mosadegh, B., Bertoldi, K., Whitesides, G.M., Wood, R.J., 2015. A 3D-printed, functionally graded soft robot powered by combustion. Science 349 (6244), 161–165.

Bekele, A., Wadee, M.A., Phillips, A.T., 2023. Enhancing energy absorption through sequential instabilities in mechanical metamaterials. R. Soc. Open Sci. 10 (8), 230762.
Chen, W., Wang, L., 2020. Theoretical modeling and exact solution for extreme bending deformation of hard-magnetic soft beams. J. Appl. Mech. 87 (4), 041002.
Chen, W., Wang, L., 2021. Large bending deformation of a cantilevered soft beam under external load: The applicability of inextensibility assumption of the centerline. Curr. Mech. Adv. Mater. 1 (1), 24–38.
Chen, W., Yan, Z., Wang, L., 2020a. Complex transformations of hard-magnetic soft beams by designing residual magnetic flux density. Soft Matter 16 (27), 6379–6388.
Chen, W., Yan, Z., Wang, L., 2020b. On mechanics of functionally graded hard-magnetic soft beams. Internat. J. Engrg. Sci. 157, 103391.
Chen, D., Zheng, X., 2018. Multi-material additive manufacturing of metamaterials with giant, tailorable negative Poisson's ratios. Sci. Rep. 8 (1), 1–8.
Chu, H., Yang, W., Sun, L., Cai, S., Yang, R., Liang, W., Yu, H., Liu, L., 2020. 4D printing: a review on recent progresses. Micromachines 11 (9), 796.
Dalela, S., Balaji, P., Jena, D., 2021. A review on application of mechanical metamaterials for vibration control. Mech. Adv. Mater. Struct. 1–26.
Damanpack, A., Bodaghi, M., Liao, W., 2019. Experimentally validated multi-scale modeling of 3D printed hyper-elastic lattices. Int. J. Non-Linear Mech. 108, 87–110.
Dudek, K., Gatt, R., Dudek, M., Grima, J., 2018. Negative and positive stiffness in auxetic magneto-mechanical metamaterials. Proc. R. Soc. A: Math. Phys. Eng. Sci. 474 (2215), 20180003.
Dudek, K.K., Wolak, W., Gatt, R., Grima, J.N., 2019. Impact resistance of composite magnetic metamaterials. Sci. Rep. 9 (1), 3963.
Fleck, N.A., Deshpande, V.S., Ashby, M.F., 2010. Micro-architectured materials: past, present and future. Proc. R. Soc. A: Math. Phys. Eng. Sci. 466 (2121), 2495–2516.
Fu, M., Xu, O., Hu, L., Yu, T., 2016. Nonlinear shear modulus of re-entrant hexagonal honeycombs under large deformation. Int. J. Solids Struct. 80, 284–296.
Furusawa, M., Maeda, K., Azukizawa, S., Shinoda, H., Tsumori, F., 2019. Bio-mimic motion of elastic material dispersed with hard-magnetic particles. J. Photopolym. Sci. Technol. 32 (2), 309–313.
Galea, R., Dudek, K.K., Farrugia, P.-S., Mangion, L.Z., Grima, J.N., Gatt, R., 2022. Reconfigurable magneto-mechanical metamaterials guided by magnetic fields. Compos. Struct. 280, 114921.
Gao, J., Cao, X., Xiao, M., Yang, Z., Zhou, X., Li, Y., Gao, L., Yan, W., Rabczuk, T., Mai, Y.-W., 2023. Rational designs of mechanical metamaterials: Formulations, architectures, tessellations and prospects. Mater. Sci. Eng.: R: Rep. 156, 100755.
Ghuku, S., Mukhopadhyay, T., 2022a. Anti-curvature honeycomb lattices for mode-dependent enhancement of nonlinear elastic properties under large deformation. Int. J. Non-Linear Mech. 140, 103887.
Ghuku, S., Mukhopadhyay, T., 2022b. On enhancing mode-dependent failure strength under large deformation: The concept of anti-curvature in honeycomb lattices. Compos. Struct. 116318.
Ghuku, S., Saha, K.N., 2019. A parametric study on geometrically nonlinear behavior of curved beams with single and double link rods, and supported on moving boundary. Int. J. Mech. Sci. 161, 105065.
Gibson, L., Ashby, M.F., 1999. Cellular Solids Structure and Properties. Cambridge University Press, Cambridge, UK.
Gonella, S., Ruzzene, M., 2008. Homogenization and equivalent in-plane properties of two-dimensional periodic lattices. Int. J. Solids Struct. 45 (10), 2897–2915.
Halpern, D., Wilson, H.B., Turcotte, L.H., 2002. Advanced Mathematics and Mechanics Applications Using MATLAB. Chapman and Hall/CRC.
Hu, L., Yu, T., 2013. Mechanical behavior of hexagonal honeycombs under low-velocity impact–theory and simulations. Int. J. Solids Struct. 50 (20–21), 3152–3165.
Jackson, J.A., Messner, M.C., Dudukovic, N.A., Smith, W.L., Bekker, L., Moran, B., Golobic, A.M., Pascall, A.J., Duoss, E.B., Loh, K.J., et al., 2018. Field responsive mechanical metamaterials. Sci. Adv. 4 (12), eaau6419.
Jang, W.-Y., Kyriakides, S., 2015. On the buckling and crushing of expanded honeycomb. Int. J. Mech. Sci. 91, 81–90.
Jiménez, F.L., Triantafyllidis, N., 2013. Buckling of rectangular and hexagonal honeycomb under combined axial compression and transverse shear. Int. J. Solids Struct. 50 (24), 3934–3946.
Josselin, M., Di Cesare, N., Castro, M., Colinart, T., Scarpa, F., Le Duigou, A., 2024. Hygro-thermal coupling on 4D-printed biocomposites as key for meteosensitive shape-changing materials. Virtual Phys. Prototyp. 19 (1), e2335233.
Kang, D., Park, S., Son, Y., Yeon, S., Kim, S.H., Kim, I., 2019. Multi-lattice inner structures for high-strength and light-weight in metal selective laser melting process. Mater. Des. 175, 107786.
Katz, J.S., Burdick, J.A., 2010. Light-responsive biomaterials: development and applications. Macromol. Biosci. 10 (4), 339–348.
Kim, S., Laschi, C., Trimmer, B., 2013. Soft robotics: a bioinspired evolution in robotics. Trends Biotechnol. 31 (5), 287–294.
Kim, Y., Parada, G.A., Liu, S., Zhao, X., 2019. Ferromagnetic soft continuum robots. Sci. Robot. 4 (33), eaax7329.
Kim, Y., Yuk, H., Zhao, R., Chester, S.A., Zhao, X., 2018. Printing ferromagnetic domains for untethered fast-transforming soft materials. Nature 558 (7709), 274–279.
Kolken, H.M., Zadpoor, A., 2017. Auxetic mechanical metamaterials. RSC Adv. 7 (9), 5111–5129.
Li, Y., 2016. Reversible wrinkles of monolayer graphene on a polymer substrate: toward stretchable and flexible electronics. Soft Matter 12 (13), 3202–3213.
Liu, Q., Mo, Z., Wu, Y., Ma, J., Tsui, G.C.P., Hui, D., 2016. Crush response of CFRP square tube filled with aluminum honeycomb. Compos. Part B: Eng. 98, 406–414.
Lu, L., Sim, J., Zhao, R.R., 2024. Mechanics of hard-magnetic soft materials: A review. Mech. Mater. 189, 104874.
Lum, G.Z., Ye, Z., Dong, X., Marvi, H., Erin, O., Hu, W., Sitti, M., 2016. Shape-programmable magnetic soft matter. Proc. Natl. Acad. Sci. 113 (41), E6007–E6015.
Malek, S., Gibson, L., 2015. Effective elastic properties of periodic hexagonal honeycombs. Mech. Mater. 91, 226–240.
Mirzaali, M., Caracciolo, A., Pahlavani, H., Janbaz, S., Vergani, L., Zadpoor, A., 2018. Multi-material 3D printed mechanical metamaterials: Rational design of elastic properties through spatial distribution of hard and soft phases. Appl. Phys. Lett. 113 (24), 241903.
Miyajima, D., Tashiro, K., Araoka, F., Takezoe, H., Kim, J., Kato, K., Takata, M., Aida, T., 2009. Liquid crystalline corannulene responsive to electric field. J. Am. Chem. Soc. 131 (1), 44–45.
Mondal, S., Mukhopadhyay, T., Naskar, S., 2025. Active heterogeneous mode coupling in bi-level multi-physically architected metamaterials for temporal, on-demand and tunable programming. Commun. Eng..
Montgomery, S.M., Kuang, X., Armstrong, C.D., Qi, H.J., 2020. Recent advances in additive manufacturing of active mechanical metamaterials. Curr. Opin. Solid State Mater. Sci. 24 (5), 100869.
Montgomery, S.M., Wu, S., Kuang, X., Armstrong, C.D., Zemelka, C., Ze, Q., Zhang, R., Zhao, R., Qi, H.J., 2021. Magneto-mechanical metamaterials with widely tunable mechanical properties and acoustic bandgaps. Adv. Funct. Mater. 31 (3), 2005319.
Morishima, Y., 2007. Thermally responsive polymer vesicles. Angew. Chem. Int. Ed. 46 (9), 1370–1372.
Mukhopadhyay, T., Adhikari, S., 2017a. Effective in-plane elastic moduli of quasi-random spatially irregular hexagonal lattices. Internat. J. Engrg. Sci. 119, 142–179.
Mukhopadhyay, T., Adhikari, S., 2017b. Stochastic mechanics of metamaterials. Compos. Struct. 162, 85–97.
Mukhopadhyay, T., Kundu, D., 2021. Mixed-mode multidirectional Poisson's ratio modulation in auxetic 3D lattice metamaterials. Adv. Eng. Mater. 2101183.
Mukhopadhyay, T., Ma, J., Feng, H., Hou, D., Gattas, J.M., Chen, Y., You, Z., 2020a. Programmable stiffness and shape modulation in origami materials: Emergence of a distant actuation feature. Appl. Mater. Today 19, 100537.
Mukhopadhyay, T., Naskar, S., Adhikari, S., 2020b. Anisotropy tailoring in geometrically isotropic multi-material lattices. Extrem. Mech. Lett. 40, 100934.
Nampally, P., Karttunen, A.T., Reddy, J., 2020. Nonlinear finite element analysis of lattice core sandwich plates. Int. J. Non-Linear Mech. 121, 103423.
Pankhurst, Q.A., Connolly, J., Jones, S.K., Dobson, J., 2003. Applications of magnetic nanoparticles in biomedicine. J. Phys. D: Appl. Phys. 36 (13), R167.
Papka, S.D., Kyriakides, S., 1998. Experiments and full-scale numerical simulations of in-plane crushing of a honeycomb. Acta Mater. 46 (8), 2765–2776.
Prajwal, P., Ghuku, S., Mukhopadhyay, T., 2022. Large-deformation mechanics of anti-curvature lattice materials for mode-dependent enhancement of non-linear shear modulus. Mech. Mater. 104337.
Qi, J., Chen, Z., Jiang, P., Hu, W., Wang, Y., Zhao, Z., Cao, X., Zhang, S., Tao, R., Li, Y., et al., 2022. Recent progress in active mechanical metamaterials and construction principles. Adv. Sci. 9 (1), 2102662.
Rich, S.I., Wood, R.J., Majidi, C., 2018. Untethered soft robotics. Nat. Electron. 1 (2), 102–112.
Rogers, J.A., Someya, T., Huang, Y., 2010. Materials and mechanics for stretchable electronics. Science 327 (5973), 1603–1607.
Scarpa, F., Panayiotou, P., Tomlinson, G., 2000. Numerical and experimental uniaxial loading on in-plane auxetic honeycombs. J. Strain Anal. Eng. Des. 35 (5), 383–388.
Sim, J., Zhao, R.R., 2024. Magneto-mechanical metamaterials: A perspective. J. Appl. Mech. 91 (3).
Singh, A., Mukhopadhyay, T., Adhikari, S., Bhattacharya, B., 2021. Voltage-dependent modulation of elastic moduli in lattice metamaterials: Emergence of a programmable state-transition capability. Int. J. Solids Struct. 208–209, 31–48.
Singh, A., Mukhopadhyay, T., Adhikari, S., Bhattacharya, B., 2022a. Active multi-physical modulation of Poisson's ratios in composite piezoelectric lattices: On-demand sign reversal. Compos. Struct. 280, 114857.
Singh, A., Mukhopadhyay, T., Adhikari, S., Bhattacharya, B., 2022b. Extreme on-demand contactless modulation of elastic properties in magnetostrictive lattices. Smart Mater. Struct. 31 (12), 125005.
Sinha, P., Kundu, D., Naskar, S., Mukhopadhyay, T., 2025. Effective elastic properties of 3D lattice materials with intrinsic stresses: Bottom-up spectral characterization and constitutive programming. Appl. Math. Model. 140, 115786.
Sinha, P., Mukhopadhyay, T., 2022. Effective elastic properties of lattice materials with intrinsic stresses. Thin-Walled Struct. 173, 108950.
Sinha, P., Mukhopadhyay, T., 2023a. On-demand contactless programming of nonlinear elastic moduli in hard magnetic soft beam based broadband active lattice materials. Smart Mater. Struct. 32 (5), 055021.
Sinha, P., Mukhopadhyay, T., 2023b. Programmable multi-physical mechanics of mechanical metamaterials. Mater. Sci. Eng.: R: Rep. 155, 100745.

Sinha, P., Walker, M., Mukhopadhyay, T., 2023. Non-invariant elastic moduli of bi-level architected lattice materials through programmed domain discontinuity. Mech. Mater. 184, 104691.
Sorohan, S., Constantinescu, D.M., Sandu, M., Sandu, A.G., 2019. In-plane homogenization of commercial hexagonal honeycombs considering the cell wall curvature and adhesive layer influence. Int. J. Solids Struct. 156, 87–106.
Surjadi, J.U., Gao, L., Du, H., Li, X., Xiong, X., Fang, N.X., Lu, Y., 2019. Mechanical metamaterials and their engineering applications. Adv. Eng. Mater. 21 (3), 1800864.
Thomas, T., Tiwari, G., 2019. Energy absorption and in-plane crushing behavior of aluminium reinforced honeycomb. Vacuum 166, 364–369.
Tibbits, S., 2014. 4D printing: multi-material shape change. Archit. Des. 84 (1), 116–121.
Truby, R.L., Lewis, J.A., 2016. Printing soft matter in three dimensions. Nature 540 (7633), 371–378.
Vogiatzis, P., Chen, S., Wang, X., Li, T., Wang, L., 2017. Topology optimization of multi-material negative Poisson's ratio metamaterials using a reconciled level set method. Comput.- Aided Des. 83, 15–32.
Wadley, H.N., 2006. Multifunctional periodic cellular metals. Philos. Trans. R. Soc. A: Math. Phys. Eng. Sci. 364 (1838), 31–68.
Wang, L., Kim, Y., Guo, C.F., Zhao, X., 2020a. Hard-magnetic elastica. J. Mech. Phys. Solids 142, 104045.
Wang, A.-J., McDowell, D., 2004. In-plane stiffness and yield strength of periodic metal honeycombs. J. Eng. Mater. Technol. 126 (2), 137–156.
Wang, H., Zhao, D., Jin, Y., Wang, M., Mukhopadhyay, T., You, Z., 2020b. Modulation of multi-directional auxeticity in hybrid origami metamaterials. Appl. Mater. Today 20, 100715.
Wilbert, A., Jang, W.-Y., Kyriakides, S., Floccari, J., 2011. Buckling and progressive crushing of laterally loaded honeycomb. Int. J. Solids Struct. 48 (5), 803–816.
Wu, L., Wang, Y., Chuang, K., Wu, F., Wang, Q., Lin, W., Jiang, H., 2021a. A brief review of dynamic mechanical metamaterials for mechanical energy manipulation. Mater. Today 44, 168–193.
Wu, X., Wen, Z., Jin, Y., Rabczuk, T., Zhuang, X., Djafari-Rouhani, B., 2021b. Broadband Rayleigh wave attenuation by gradient metamaterials. Int. J. Mech. Sci. 205, 106592.
Xu, Q., Liu, J., 2018. An improved dynamic model for a silicone material beam with large deformation. Acta Mech. Sin. 34 (4), 744–753.
Yang, L., Harrysson, O., West, H., Cormier, D., 2015. Mechanical properties of 3D re-entrant honeycomb auxetic structures realized via additive manufacturing. Int. J. Solids Struct. 69, 475–490.
Zadpoor, A.A., 2016. Mechanical meta-materials. Mater. Horizons 3 (5), 371–381.
Zhang, Q., Cherkasov, A.V., Arora, N., Hu, G., Rudykh, S., 2023. Magnetic field-induced asymmetric mechanical metamaterials. Extrem. Mech. Lett. 59, 101957.
Zhao, Y., Ge, M., Ma, W., 2020. The effective in-plane elastic properties of hexagonal honeycombs with consideration for geometric nonlinearity. Compos. Struct. 234, 111749.
Zhao, X., Kim, J., Cezar, C.A., Huebsch, N., Lee, K., Bouhadir, K., Mooney, D.J., 2011. Active scaffolds for on-demand drug and cell delivery. Proc. Natl. Acad. Sci. 108 (1), 67–72.
Zhao, R., Kim, Y., Chester, S.A., Sharma, P., Zhao, X., 2019. Mechanics of hard-magnetic soft materials. J. Mech. Phys. Solids 124, 244–263.
Zschernack, C., Wadee, M.A., Völlmecke, C., 2016. Nonlinear buckling of fibre-reinforced unit cells of lattice materials. Compos. Struct. 136, 217–228.